LBL--27180

DE89 016310

TWO PHOTON PRODUCTION OF PION PAIRS IN e^+e^- COLLISIONS AT 29 GEV

John Henry Boyer

(Ph.D. Thesis)

Physics Division

Lawrence Berkeley Laboratory

1 Cyclotron Road

Berkeley, California 94720

May 1989

This work was supported by the Director, Office of Energy Research, Office of High Energy and Nuclear Physics, Division of High Energy Physics of the U.S. Department of Energy under Contract Number DE-AC03-76SF00098.

TWO PHOTON PRODUCTION OF PION PAIRS IN e^+e^- COLLISIONS AT 29 GEV

John Henry Boyer

Abstract

We present a new measurement of the cross section for the process $e^+e^- \rightarrow e^+e^-\pi^+\pi^-$ at center-of-mass energy 29 GeV for invariant pion pair masses $M_{\pi\pi}$ between 350 MeV/c^2 and 3.5 GeV/c^2. For $M_{\pi\pi}$ above 2.1 GeV/c^2, we find approximate agreement with the hard-scattering prediction of Brodsky and Lepage. In the low mass region, we observe the $f_2(1270)$, and measure its radiative width to be 3.15 $\pm$ .04 $\pm$ .39 keV. We also observe an enhancement in the $\pi^+\pi^-$ spectrum near 1 GeV. We hypothesize that it is the $f_0(975)$ and determine it's radiative width to be 0.29 $\pm$ .07 $\pm$ .12 keV.

To my grandfather, Henry Rau

Acknowledgements

I would like to thank the whole Mark II Collaboration for all the work which made this experiment run smoothly and well. It has been an honor and a pleasure to work with so many fine physicists. I have benefitted enormously from my fellow graduate students. Particular thanks go to Darien Wood, Drew Baden, Bill Schmidke, and Peter Rowson for their friendship, and for the many things they taught me.

I am very grateful to my advisor George Gidal, for his advice, insight, encouragement, and good humor. Without him, this work would not have been possible. I also thank Gerson Goldhaber for his very helpful advice.

Finally, I am most grateful to my parents for their love, their guidance, and their faith.

Table of Contents

Chapter 1. THE TWO PHOTON PRODUCTION MECHANISM

1.1 INTRODUCTION

According to the theory of Quantum Electrodynamics (QED), pairs of charged particles can be produced in collisions between two photons. In today's world, there is no facility where it is possible to collide beams of free real photons. However, it is possible to observe collisions between virtual photons at e^+e^- colliders through the second order QED process pictured in Fig. 1.1. In this thesis we will examine the process

$$e^+e^- \rightarrow e^+e^-\pi^+\pi^- \tag{1.1}$$

From a measurement of the cross section for reaction 1.1, we will extract the cross section for the two photon production of pion pairs

$$\gamma\gamma \rightarrow \pi^+\pi^- \tag{1.2}$$

over the range of $\gamma\gamma$ invariant masses between 350 MeV/c^2 and 3.5 GeV/c^2.

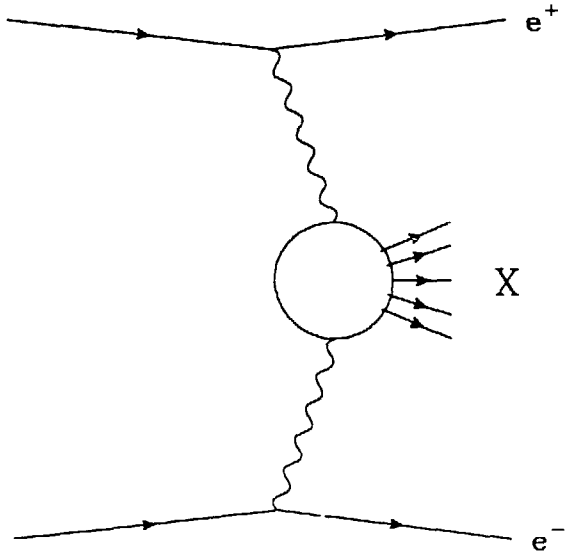

Figure 1.1 *Feynman diagram for two photon production of final state X*

Reaction 1.1 and the closely related reaction for neutral pion pair production ($e^+e^- \to e^+e^-\pi^0\pi^0$) have been observed in many other experiments[1-15]. We will present the highest statistics measurement to date. Based on previous observations, we expect to observe a large continuum production of pion pairs, as well as resonance production of the $f_2(1270)$. From our measurement of its two photon production, we will determine the partial decay rate for $f_2(1270) \to \gamma\gamma$, or equivalently, its radiative width: $\Gamma(f_2(1270) \to \gamma\gamma)$. We will also search the data for other resonances. We will present evidence for a candidate resonance near 1 GeV/c^2.

The Standard Model predicts that we can describe the two photon production of hadrons by calculating the QED cross section for quark pair production ($\gamma\gamma \to q\bar{q}$), and then determining the hadronization of the quarks using the theory of Quantum Chromodynamics (QCD). In practice, the composite nature of hadrons can only be probed using photons of wavelength of a size such that the constituent quarks can be resolved. The cross section for reaction 1.1 has been calculated[16] in the high mass limit from QED and a leading order QCD model which uses the experimentally determined pion form factor. We will compare the observed continuum with this calculation to determine the invariant pion pair mass ($M_{\pi\pi}$) above which it becomes valid. For longer wavelength photons, or lower $M_{\pi\pi}$, the QED and QCD parts of the process cannot be separated. Therefore we must resort to understanding the observed cross section in terms of a phenomenological model which treats pions as elementary particles. We will compare our data to the predictions of several such models. [17-19]

1.1.1 Kinematics and Definition of Variables

In Fig. 1.2 we show a schematic representation of the two photon production of a final state pair of particles x. Some symbols frequently used in this analysis are shown in Fig. 1.2, and defined in Table 1.1. In a typical two photon event, an electron from each beam emits a photon, and continues approximately along the beam axis, scattering through a very small angle. The emitted photons carry a correspondingly small fraction of the beam energy. An event where one or both of the scattered electrons is observed at a small but measureable angle (the minimum scattering angle

at which the electron can be detected is usually about 1°), is called a tagged two photon event. As indicated by the nomenclature, such events are very well identified as coming from the interaction of two photons (as opposed to annihilation). In most experiments only about 10% of all two photon events are tagged. In this thesis, we are concerned only with untagged or anti-tagged† events. However, even untagged events are relatively easy to distinguish from annihilation events by requiring that the visible energy be less than 20% of the available center-of-mass energy.

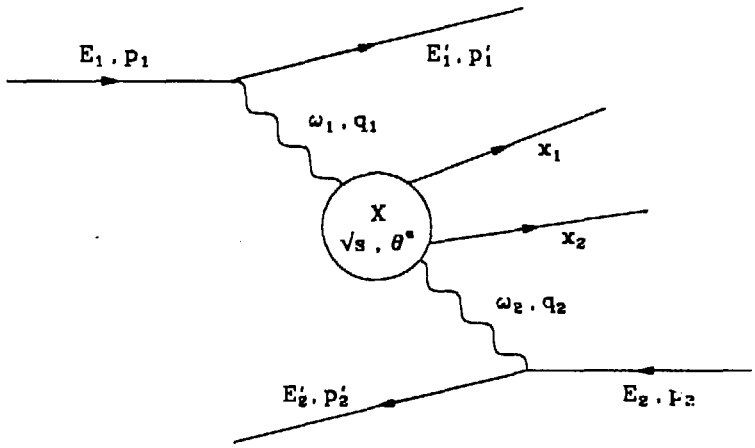

Figure 1.2 *Kinematics of the two photon production of a pair of final state particles x in the reaction $e^+e^- \rightarrow e^+e^-x^+x^-$*

Untagged events have several properties that are important in this analysis. The invariant mass squared (Q^2) of the photons in such events is small compared to s. Neglecting the electron mass, we may write

$$Q^2 = (p - p')^2 \simeq 2EE'(1 - cos\theta') \tag{1.3}$$

† We require that neither scattered electron is detected.

Table 1.1 *Definition of variables used in this analysis*

Variable	Description
E, p	Energy-momentum 4–vector of electron beam
E', p'	Energy-momentum 4–vector of scattered electron
ω, q	Energy-momentum 4–vector of virtual photon
Q^2	Negative invariant mass squared of virtual photon
X	produced final state
x_i	outgoing final state particles
$\sqrt{s}$	$\gamma\gamma$ center-of-mass energy
θ^*	Center-of-mass $\gamma\gamma \rightarrow x_i x_j$ scattering angle
M_{xx}	Invariant mass of produced xx pair

where θ' is the angle with respect to the beam of the scattered electron. For the maximum θ' and minimum s, Q^2/s is about 1/2. However, since the photon propogator is inversely proportional to Q^2, the cross section will be peaked for Q^2 much less than s. This is important, because virtual photons may have a longitudinally polarized component only at the level of Q^2/s. Knowing that photons are transversely polarized facilitates our ability to understand the photon beams, and constrains the allowed quantum numbers of any produced final state.

The analysis of two photon processes is somewhat complicated by the kinematics. In particular, the $\gamma\gamma$ center-of-mass reference frame is usually boosted along the beam axis with respect to the lab. At a typical detector such as the Mark II, less than 10% of all two photon events are observable. The rest contain only tracks produced at small angles with respect to the beam. Therefore, one of the important aspects of any two photon analysis must be to understand in detail the nature of the effective beams of photons.

1.2 Equivalent Photon Approximation

One may understand the interaction of photons at an e^+e^- colider, as being due

to a cloud of virtual photons associated with the electrons and positrons that make up the beams.

In the equivalent photon aproximation, we divide the process into two steps: the emission of photons by the beams, and their subsequent interaction. This is equivalent to saying that the cross section factorizes:

$$\frac{d\sigma(e^+e^- \to e^+e^-\pi^+\pi^-)}{dM_{\pi\pi}} = \frac{d\mathcal{L}_{\gamma\gamma}}{dW_{\gamma\gamma}} \cdot \sigma(\gamma\gamma \to \pi^+\pi^-) \tag{1.4}$$

where $d\mathcal{L}_{\gamma\gamma}/dW_{\gamma\gamma}$ is called the luminosity function, which relates the two processes. We can calculate $d\mathcal{L}_{\gamma\gamma}/dW_{\gamma\gamma}$ by using the Weizsäcker-Williams approximation[20,21]. This says that the energy spectrum $N(\omega)$ of virtual photons associated with an electron of energy E is given by

$$\frac{dN_\gamma}{d\omega} = \frac{2\alpha}{\pi\omega} \ln \frac{E}{m_e} \tag{1.5}$$

One then assumes that the luminosity function can be derived from two such photon flux factors, one from each electron-photon vertex (see Fig. 1.1), By integration, one derives the Low formula:[22,23]

$$\frac{d\mathcal{L}}{dz} = 4\left(\frac{\alpha}{\pi}\right)^2 \frac{1}{z}\left(\ln\frac{E}{m_e}\right)^2 \left[2(1+\frac{1}{2}z^2)^2 \ln\frac{1}{z^2} - (1-z^2)(3+z^2)\right] \tag{1.6}$$

where z is the scaled two photon energy: $z = \sqrt{s}/2E$. A more exact calculation has been performed by Bonneau, Gourdin, and Martin[24]. They derive the luminosity function by integrating over the complete phase space of the scattered electron and positron, assuming that the contribution due to longitudinally polarized photons (which is allowed for virtual photons, but not for real ones) is negligible. Their calculation also assumes that the two photon cross section for the process being considered does not depend on Q^2. These are reasonable approximations to make for the case of untagged electrons, where the photon flux is dominated by nearly real photons. Real (Q^2=0) photons must be transversely polarized. The longitudinal component of the polarization of a virtual photon is suppressed by the factor Q^2/s, so for untagged events where Q^2 is small, transversely polarized photons dominate.

In Ref. 25 Field compares the prediction of the Low formula to the more exact calculation of Reference 24. He finds that the Low formula overestimates the luminosity function by $\sim 15\%$.[†] In this work, we will frequently refer to the equivalent photon approximation, or to the luminosity function. By this we mean the more exact formula of Reference 24.

[†] Field finds that the leading log approximation to the Bonneau, Gourdin and Martin formula overestimates the luminosity function at PEP energies by $\sim 30\%$ for $\gamma\gamma$ energies of interest in this experiment. The leading log approximation differs from the Low formula by $\ln(2E_{beam}/m_e)/\ln(E_{beam}/m_e)$, or 14%. Thus the factor of 15%.

Chapter 2. THE APPARATUS

The Mark II is a magnetic spectrometer designed to measure charged and neutral particles produced in high energy e^+e^- collisions. It was installed at the PEP (Positron Electron Project) storage ring at the Stanford Linear Accelerator Center (SLAC) in 1979, and stayed there through the Spring of 1984.

2.1 PEP

PEP is a 2.2 km circumference ring through which three bunches each of 14.5 GeV positrons and electrons circulate. There are six different interaction regions (IR's). The Mark II was at one such region. At each IR, bunches cross every 2.4 μsec. Interactions occur in a region with an rms width of $\sigma_{x,y,z} = (60\mu\text{m}, 480\mu\text{m}, 1.5\text{cm})$, where the z-axis is along the beam direction, and the x and y axes are horizontal and vertical respectively. The peak luminosity was $3 \times 10^{31}\text{cm}^{-2}\text{sec}^{-1}$.

2.2 The Detector

During it's tenure at PEP, the Mark II had several different configurations. In this thesis we will use only data collected beginning in the Spring of 1982, after the addition of the Vertex Chamber (VC) and the reduction of the magnetic field from 4.7 kG to 2.3 kG. The net effect of these two changes was to somewhat improve the momentum resolution and to allow us to trigger on lower momentum tracks, substantially enlarging the range of Two-Photon invariant masses accessable to us. Of the 220 pb^{-1} of data collected at PEP, approximately 209 pb^{-1} were collected after 1981.

The Mark II has a cylindrical geometry, with the axis in the z-direction. The detector, as it was configured at that time, is pictured in Figure 2.1 and in Figure 2.2. Details of the detector components have been described elsewhere.[26] We reiterate here those features of the Mark II which are important to this analysis.

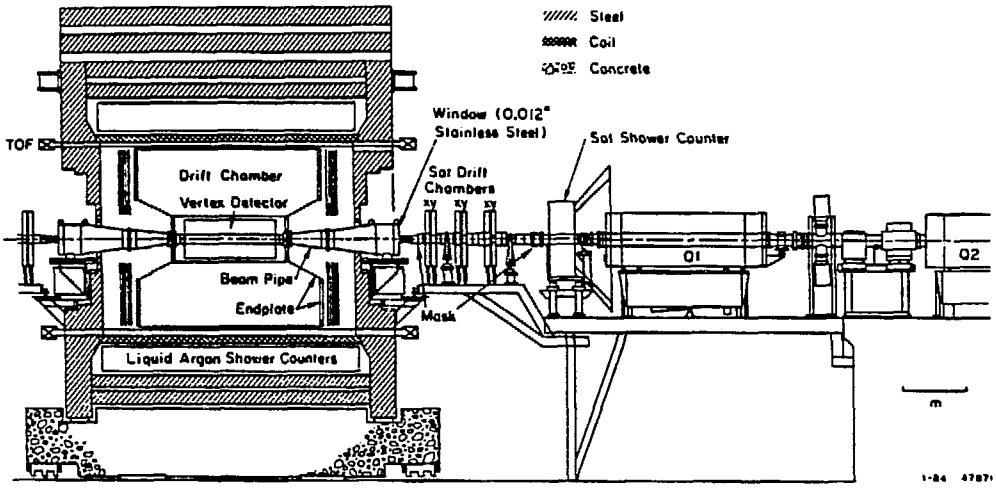

Figure 2.1 *The Mark II detector, side view*

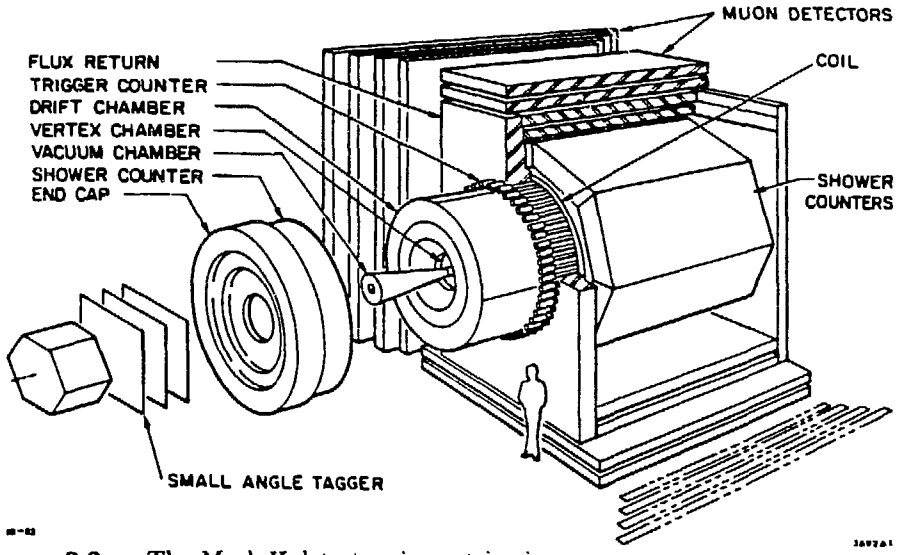

Figure 2.2 *The Mark II detector, isometric view*

2.2.1 Tracking

Tracking information was provided by the Main Drift Chamber (DC), in conjunction with the VC. The DC consisted of sixteen concentric layers of sense wires, covering radii between 41 cm and 145 cm from the beam axis. The position resolution was approximately 200 μm in the xy-plane at each layer. Ten of the layers were tilted

at an angle of $\pm 3°$ with respect to the z-axis. The resulting stereo information was used to measure the z position. The VC was a high resolution drift chamber. It consisted of an inner band of four layers of sense wires at a radius of ~10 cm, and an outer band of three layers at a radius of ~30 cm. The drift chamber was immersed in a conventional solenoidal magnet, with the field along the z-axis. The magnet had two layers, producing a nominal field of 4.7 kG. The coil consisted of 1.4 radiation lengths and 0.3 interaction lengths of aluminum at a radius of 1.6 m. However, a short developed between the two layers in early 1982. The solution was to disconnect the inner layer, causing us to run at half-field, or 2.3 kG, from that time on. The combined information from the DC and the VC with a field strength of 2.3 kG provided a momentum resolution in the xy-plane of $(\sigma_{p_{xy}}/p_{xy})^2 = (0.025)^2 + (0.011 p_{xy})^2$ (p_{xy} in GeV/c), where the first term is due to the contribution from multiple scattering.

2.2.2 *Time of Flight*

The Time of Flight (TOF) system consisted of 48 scintillation counters at a radius of 1.51 m, or just inside the magnet coil. Each counter was read out at both ends by phototubes. The rms resolution, averaged over the duration of the run, was 375 psec. This timing, combined with the tracking information, allowed $\pi - \mu$ separation up to momenta of $\sim$ 150 MeV/c, $\pi - e$ separation up to $\sim$ 200 MeV/c, $K - \pi$ separation up to $\sim$ 830 MeV/c, and proton identification up to $\sim$ 1.4 GeV/c. It also allowed unambiguous identification of cosmic ray events.

2.2.3 *Calorimetry*

Electromagnetic calorimetry was provided by the Liquid Argon Calorimeter (LA). Eight modules circled the magnet coil at a minimum radius of 1.8 m, covering a solid angle of about 64% of 4π. Each module consisted of 37 planes of 2 mm thick lead/antimony separated by 3 mm and immersed in liquid argon. Signal planes and ground planes were alternated. The signal planes were divided into strips running in one of three different directions: 3.8 mm strips parallel and perpindicular to the beam to measure azimuth and polar angle respectively, and 5.4 mm strips at

a 45° angle to resolve ambiguities. The front of each module also contained a trigger gap – three 1.6 mm thick aluminum planes separated by 8 mm of liquid argon. The central plane was the signal plane and was segmented into strips perpindicular to the beam axis. The trigger gap was used to identify and correct the energy of showers that began in the magnet coil. The total calorimeter thickness was 14.5 radiation lengths, and the energy resolution for electro-magnetic showers was $\frac{\sigma_E}{E} = \frac{14\%}{\sqrt{E}}$. Use of the LA was crucial in identifying pions, and will be explained in Chapter 3.

The Mark II also had End Cap Calorimeters, but they were not used in this analysis because we did not trigger on charged tracks pointing toward the End Caps.

2.2.4 *Muon Chambers*

Outside the LA Calorimeter were four Muon Chambers, providing muon identification over a solid angle of 45% of 4π. Each chamber consisted of four layers of aluminum proportional tubes separated by iron. The iron served as both flux return and hadron absorber. At normal incidence, a particle needed to traverse 1.4 interaction lengths of material to reach the first layer of tubes, and 7.4 interaction lengths to reach the fourth layer. This translates to a threshold of ~800 MeV/c for muon identification using only the first layer, or 2 GeV/c using all four layers. The first layer of tubes measures polar angle, while the other three measure azimuth.

2.2.5 *Small Angle Tagging*

The Small Angle Tagging (SAT) system was designed to tag electrons from small angle Bhabha events and two-photon interactions that scattered between 21 and 82 milliradians from the beam axis. At each end of the detector are three layers of drift chambers with a spatial resolution of $\sim 300\mu$m in the xy-plane. These are followed by three layers of acceptance defining scintillator, and 18 layers of $\frac{1}{4}$ inch lead alternating with $\frac{1}{2}$ inch scintillator. The energy resolution achieved for electrons is $\frac{\sigma_E}{E} = \frac{15\%}{\sqrt{E}}$. Using the SAT system to count Bhabha events, luminosity was measured with an uncertainty of $\sim 5\%$. In this thesis, in which we analyze only untagged two-photon events, the SAT system is used as a veto for tagged events.

2.3 The Trigger

The Mark II used a two-tiered trigger. The primary trigger took only 1 μsec to make a decision. There were several different primary triggers. Events of interest in this thesis typically satisfied the Charged Trigger. This required a coincidence of a beam crossing, a TOF hit, 2 of 4 inner VC layers hit, and 4 of 8 selected DC layers hit, at least 2 of which were in the outermost 6 layers. Neutral and SAT Bhabha triggers also contributed to the primary trigger rate of about 1 kHz. When a primary trigger occurs, data taking is halted for 34 μsec while the secondary trigger decides whether to read out the event to the Mark II Vax 11/780 and subsequently to log it to tape. Dead time was dominated by the primary trigger rate and was about 3%.

The secondary trigger employed more sophisticated pattern-recognition electronics to search for charged tracks. The charged trigger required at least two A-tracks. The criteria for an A-track were 2 of 4 inner VC layers hit, 4 of 8 selected DC layers hit at least 2 of which were in the outer 6 DC layers, and a TOF hit. These hits all had to be along the expected path for some charged track. This latter criterion was implemented using the Curvature Modules. The twenty-four modules were programmed to look for tracks of different curvature, twelve each for positively and negatively charged tracks. The smallest radius of curvature searched for was 85 cm, corresponding to tracks with a transverse momentum of about 60 MeV/c in a magnetic field of 2.3 kG. Information from the twelve tracking chamber layers used in the trigger was fed continuously to the curvature modules, with 10 MHz clock pulses defining the azimuthal angle of the hits. Each module then used a different set of programmable delays d_i and widths w_i to search for a coincidence of hits from different layers in a given curvature road. This is shown shematically in Fig. 2.3. The time of the coincidence also gave a preliminary estimate of the azimuthal angle of the track. The Curvature Modules are > 98% efficient at finding A-tracks that are within the fiducial volume of interest in this analysis, that have momentum greater than 400 MeV/c, and that originate at the Interaction Point (IP). A detailed measurement of the charged trigger efficiency is described in Chapter 4.

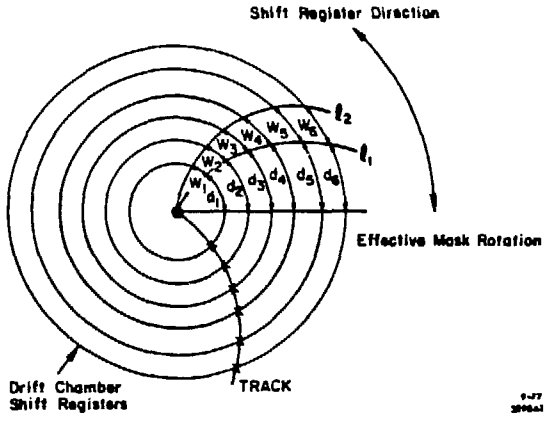

Figure 2.3 *Definition of a curvature module road*

2.4 Event Reconstruction

The event reconstruction program is called PASS2. Tapes containing data processed by PASS2 are called the PASS2 tapes. Raw data tapes were first searched for charged tracks in the DC and VC. At least seven total hits (or DAZM's) were required, with at least four hits in stereo layers. A helix was fit to the DAZM's. Each track was then traced outward through the other components of the detector. The position at which each track hit a TOF scintillator was used in conjunction with timing information from the TOF phototubes to determine the time-of-flight. Energy deposited in the LA ($E_{\rm LA}$) was associated with the track if it was in a strip that could have been hit by an electromagnetic shower. Muon hits were also associated with the charged track.

The LA was then searched for neutral clusters. When a LA strip was found to be used in two different charged or neutral clusters, a sharing algorithm was used to divide the energy from that strip between the two clusters, and the $E_{\rm LA}$'s were adjusted accordingly.

For most of the data processing, PASS2 contained a filter (CHUKIT) whose goal was to keep low invariant mass 2-prong events from swamping the PASS2 tapes. Unfortunately, it is just these events which are of interest in this analysis. Thus it was necessary to reprocess the raw data tapes to recover the events thrown out by

CHUKIT. These events were saved on the KEEPASS2 tapes. The possibility that some events were lost in this process is considered in a later chapter.

Chapter 3. PARTICLE IDENTIFICATION

The principal backgrounds to the reaction $\gamma\gamma \rightarrow \pi^+\pi^-$ are the $\gamma\gamma$ production of lepton pairs: *i.e.* $\gamma\gamma \rightarrow e^+e^-$, and $\gamma\gamma \rightarrow \mu^+\mu^-$. In Fig. 3.1 we show predicted cross sections for the two photon production of pion pairs and lepton pairs. One sees that except near the $f_2(1270)$ resonance, the backgrounds are much larger than the signal. Therefore, we must optimize the rejection of electrons and muons. We use several different methods of particle identification, depending on the momentum of the track. For $M_{\pi\pi}$ between 350 and 400 MeV/c^2, we identify pion pairs using the TOF system. For $M_{\pi\pi}$ between 540 MeV/c^2 and 1.6 GeV/c^2, we use the LA Calorimeter. For $M_{\pi\pi}$ between 1.7 and 3.5 GeV/c^2, we use the LA to reject electrons, and the Muon Chamber to reject muons, but do not distinguish between pions and kaons. In this chapter we describe each of these methods.

3.1 Low Momentum Pion Identification

The TOF counters were capable of measuring time of flight with a time averaged resolution of $\sim$ 375 psec. Since the cross section for $\gamma\gamma \rightarrow \mu^+\mu^-$ is greater than that for $\gamma\gamma \rightarrow \pi^+\pi^-$ by a factor of 10 to 20 for very low momentum tracks, we expect to be able to reliably measure the pion pair cross section only at momenta where the expected TOF for a pion is 3σ greater than that for a muon. The situation is somewhat improved for pair events, because each event must have two tracks of the same species. If we look at the sum of the TOF's of the two tracks ($t_{1+2} = t_1 + t_2$), the difference between $t_{\pi\pi}$ and $t_{\mu\mu}$ (the expected values of t_{1+2} for pion pairs and muon pairs respectively) is greater by a factor of 2 than the difference in expected TOF for an individual track, while the resolution in t_{1+2} is only a factor of $\sqrt{2}$ poorer[†] than the single track resolution.

[†] The measurements of the TOF of the two tracks are independent, so the uncertainties are added in quadrature.

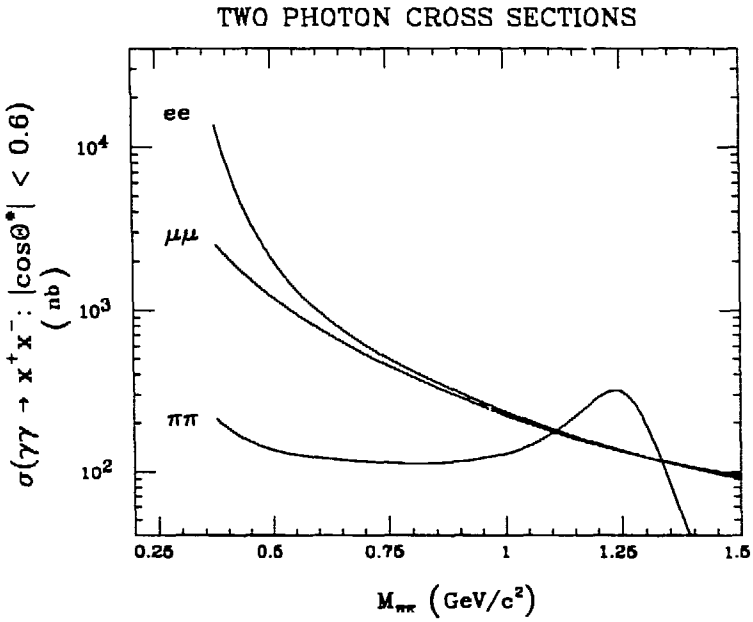

Figure 3.1 *Predicted two photon cross sections for pion pairs and lepton pairs. The predictions for lepton pairs are from a Monte Carlo calculation. The prediction for pion pairs is that of Morgan and Pennington,[17] where the pion pair cross section consists of a non-resonant continuum and the large $f_2(1270)$ resonance. The observed peak of the $f_2(1270)$ is shifted due to interference with the continuum.*

For convenience, when we measure the number of pion pair events, we plot $t_{1+2} - t_{\pi\pi}$ for all events in the appropriate kinematic region such that $t_{\pi\pi} - t_{\mu\mu}$ is greater than some minimum value to be selected such that the pion peak is well-separated from the muon peak. We observe that the resolution for low momentum tracks is substantially worse than that measured for Bhabha eevents. This poorer resolution in $t_{\pi\pi}$ is due to the uncertainty in the track's measured momentum and it's path length to the TOF counters. Both of these factors contribute to a lesser extent to the TOF resolution measured with Bhabha electrons. Another possible source of poorer resolution is a pulse height dependent correction to the measured TOF. Low momentum tracks might have larger fluctuations in pulse height than Bhabha electrons. An attempt was made to determine the pulse height dependence of the

measured TOF offline, but this correction could only be determined using Bhabhas, rather than low momentum pions.

The net result is that the measured resolution in $t_{1+2} - t_{\pi\pi}$ is not 530 psec, as expected, but is closer to 700 psec. Therefore we require that $t_{\pi\pi} - t_{\mu\mu}$ is at least 2 nsec in order to measure the pion pair cross section using TOF identification. Similarly, we will apply the same criterion in order to identify muon pair events, or the criterion that $t_{\mu\mu} - t_{ee}$ is at least 2 nsec in order to identify electron pair events.

3.2 High Momentum Pion Identification

Muons can be identified for momenta greater than 800 MeV/c. At this momentum, electrons can be easily distinguished from pions by using the standard Mark II algorithm for $\pi - e$ separation,[27] but, it is not possible to separate pions from kaons at these high momenta. Therefore, we will measure the combined pion pair and kaon pair cross sections for $W_{\gamma\gamma}$ greater than 1.7 GeV. Since the theory predicting these two cross sections is very similar (the two cross sections differ only by a form factor in the high mass continuum), this is an appropriate measurement to make. Details of this method will be described in a later chapter.

3.3 Intermediate Momentum Pion Identification

For pion momenta too large for TOF identification and too small for standard $\pi - e$ separation, we use the LA calorimeter to identify pions in a slightly different way. For momenta less than 800 GeV/c, we can still use the TOF system to eliminate kaons and protons, thus we must concentrate on eliminating leptons from the sample. In order to do this, we take advantage of a particular feature of the MARK II detector.

Before entering the LA calorimeter, a particle must traverse 12 cm of aluminum in the 0.3 interaction length magnet coil. In Fig. 3.2 we show the probability that a pion will have at least one nuclear interaction in the magnet coil. If an interaction causes a pion to scatter through a fairly large angle, the pion will either miss the LA module it was headed toward, or hit it at a point other than that extrapolated from the reconstructed Drift Chamber track. Leptons, on the other hand, do not typically

scatter through large angles in material. This difference provides the signature by which we can identify pions. The detailed identification criteria will be chosen so as to minimize contamination in the pion sample from misidentification of leptons.

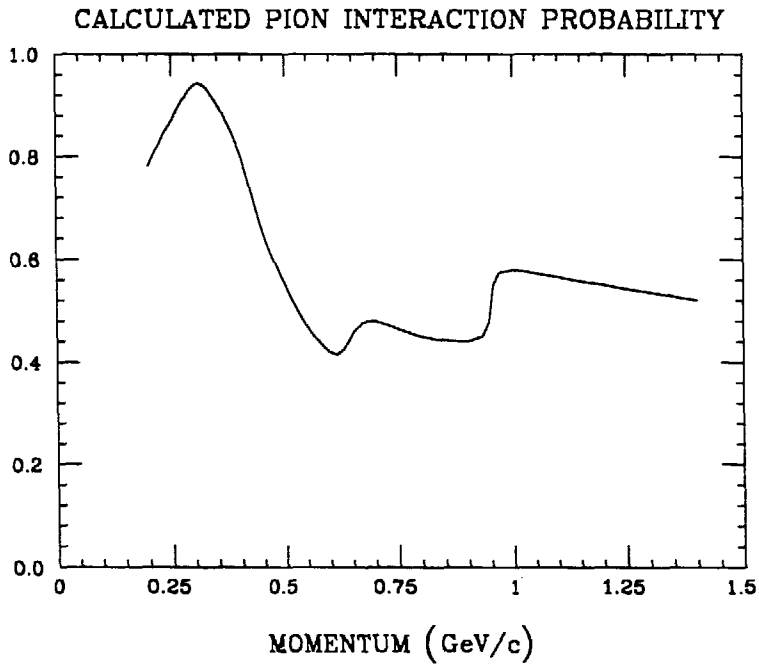

Figure 3.2 *Probability that a pion will interact in the magnet coil as calculated from the total cross sections σ_{π^+p} and σ_{π^-p}[28], and the interaction length of aluminum. We have assumed that the momentum dependence is given approximately by that of σ_{π^+p} and σ_{π^-p}, and normalized to the total cross section of aluminum for extremely relativistic incident beams near 100 GeV/c, where the interaction length is defined.*

For pion momenta near 300 MeV/c, the dominant contribution to the total pion nucleon cross section is from the (I,J) = $(\frac{3}{2}, \frac{3}{2})$ $\Delta(1232)$ resonance. From isospin rotation, one expects that the I=$\frac{3}{2}$ contribution to σ_{π^+p} will be three times greater than its contribution to σ_{π^-p}. One also expects that $\sigma_{\pi^+p} = \sigma_{\pi^-n}$ and $\sigma_{\pi^-p} = \sigma_{\pi^+n}$. Since there are more neutrons than protons in aluminum, (14 to 13), there are slight differences in the interaction probabilities for positively and negatively charged pions. However, a given event will contain exactly one pion of each charge. Thus the probability of correctly identifying either one or both of the two pions in an event may

be accurately estimated from a measurement of the average identification probability of the two pions. (We introduce here the following notation: $P_{ID}(i)$ is the probability that particle i will satisfy the criteria for identification as a pion using the LA Calorimeter as described below. Thus $P_{ID}(\pi)$ is the pion identification probability, while $P_{ID}(e,\mu)$ are the probabilities that a muon or electron will be misidentified as a pion. $P_1(\pi\pi)$ and $P_2(\pi\pi)$ are the probabilities that 1 or both (2) pions in a pion pair event will be correctly identified. Similarly, $P_1(ee,\mu\mu)$ and $P_2(ee,\mu\mu)$ are the probabilities that 1 or both leptons in a lepton pair event will be misidentified as pions.)

3.3.1 Identification Criteria

Every charged track has associated with it the quantity $E_{\rm LA}$, or energy deposited in the LA. $E_{\rm LA}$ is determined as follows:

- A reconstructed DC track is projected into an LA module. At each layer we determine which strip the track should have crossed. Nearby strips are checked for a signal greater than a noise threshold. If a signal is found within the search distance (1 to 1.7 strip widths depending on the layer) then adjacent strips are also checked and included if they are above threshold. As many as four adjacent strips in any layer may contribute to $E_{\rm LA}$.
- The energy in each layer is then corrected and summed. The first layer, which is called the trigger gap, is scaled up to account for loss in the magnet coil. The last layer, if it is above threshold, is corrected for leakage. Finally, corrections are applied that are determined by requiring that on average, Bhabha electrons have the beam energy of 14.5 GeV, less radiative corrections.

As a consequence of this method, it is possible for a scattered pion to deposit energy in some layers far enough away from the projected path so that the energy is not included in $E_{\rm LA}$. In general, all of the energy deposited by leptons is included in $E_{\rm LA}$. Minimum ionizing muons deposit energy centered at about 250 MeV, and electrons deposit all their energy. Therefore, by requiring that a charged track of momentum > 200 MeV/c has $E_{\rm LA} < 130$ MeV, we select a sample that is enriched

in pions. The actual cut used was tuned as a funtion of momentum to optimize the signal-to-noise ratio.

Keeping in mind the goal that $P_{ID}(e,\mu)$ be minimized, we require a track to pass certain cuts before we consider it as a candidate for pion identification. These cuts are designed to ensure that the track is well measured, minimizing the possibility that the wrong LA strips will be searched. We also require that the projected location at which a track will intersect a LA module is far enough from the edge of the module so that the resulting shower will be fully contained.

In this analysis, we first apply a set of event cuts to select a sample of clean $\gamma\gamma$ events with a "true" 2–prong topology, *i.e.* the only undetected tracks in the event were the scattered beam electrons, which continued unobserved along the beam axis. Some of the event cuts also help to insure that tracks are well measured. Other cuts are applied only to a particular track. A track must pass all the track cuts to be identified as a pion. A good pion pair event could however have one identified pion and one track which failed one of the track cuts.

Event Cuts

- We accept only events with exactly one positive and one negative charged track. No other charged tracks are allowed, including tracks in the SAT system (small angle tagger).
- A vertex must have been found. This vertex must be within 5 cm of the interaction point in r and in z.
- Both tracks must have $p_t > 100$ MeV/c.
- Both tracks must intersect the LA calorimeter at $z_{\rm LA} < 1.7$ m. Along with the previous cut, this cut insures that the trigger efficiency is reasonably good.
- Both tracks must have a distance of closest approach to the beam axis of less than 1.5 cm.
- If there is TOF information, then the TOF difference between the two tracks must not be consistent with that expected for a cosmic ray ($\sim$10%). If a measured TOF is greater than that expected for a pion, the calculated probability that the track is a pion must be at least 10%. This cut removes events with

higher mass particles.

- The cosine of the center of mass scattering angle ($\cos\theta^*$), calculated under the assumption that both tracks are pions, and that the two photons are along the beam axis, must have absolute value less than .6. Few events which pass the other cuts fail this cut.
- Finally, the net transverse momentum of the two tracks ($\sum p_t$) must be less than 150 MeV/c. The maximum allowable $\sum p_t$ for an untagged event is 600 MeV/c, when both electrons scatter through 20 mrad. However, the distribution is strongly peaked at lower $\sum p_t$: ~90% of all events analyzed have $\sum p_t < 150$ MeV/c. Events with undetected tracks or neutral energy will have much larger $\sum p_t$, so this cut substantially reduces backgrounds from events with more than two tracks (where only two charged tracks were found).

Track Cuts

- A track must have at least eight DC and VC hits, at least six of which are in the DC. Fewer than 0.5% of all tracks fail this cut.
- There is a dead space between LA modules. In order to avoid these inefficient regions, we require tracks to be at least 2° in azimuth from the edge of an LA module. Since the electron and positron beams are unpolarized, all cross sections must be azimuthally symmetric. Therefore, we expect this cut to remove 8.9% of all tracks. Observation is consistent with this expectation.
- We also require that the energy weighted mean position of the LA shower associated with the track be at least one LA strip width (3.8 cm) from the edge of the module. This is only about 1° from the edge, which makes the cut less stringent than the previous cut, but because of shower fluctuations, it removes an additional 2% of all tracks.
- A track must not point toward any of the support posts in the LA. These are areas of reduced efficiency covering approximately 1.2% of the active region of the LA calorimeter.
- No more than half of the deposited energy contributing to E_{LA} may be shared with another LA shower, neutral or charged. This cut reduces the possibility

that $E_{\rm LA}$ of a track is mismeasured due to the presence of a nearby neutral. It is important in the selection of a clean sample of tracks for the calibration of the pion identification process. For 2-prong events, it is relatively unlikely for a real photon to share LA energy with a pion. However, it is possible for a "fake" photon to cause a track to fail this cut. The fake photon could be due either to noise or to a scattered pion.

The efficiencies of the event cuts are included in the overall event efficiency measured using a Monte Carlo simulation described in Chapter 4. For events which pass the event cuts, we will attempt particle identification. To be identified as a pion, a track must pass the track cuts and have $E_{\rm LA}$ less than the threshold for pion identification. The particle identification probabilities ($P_{ID}(\pi, e, \mu)$) include the efficiency for a track to pass the event cuts, so if $N_{\pi\pi}$ pion pair events pass the event cuts, $N_{\pi\pi}\cdot P_{ID}(\pi)\cdot P_{ID}(\pi)$ events will have both pions identified, $N_{\pi\pi}\cdot(1\text{-}P_{ID}(\pi))\cdot(1\text{-}P_{ID}(\pi))$ events will have neither pion identified, and the rest will have exactly one pion identified. Therefore, we must know the probability that a track will be well-measured as well as the probability that a well-measured track will be identified as a pion.

The inefficiencies associated with most of the track cuts are either well understood or negligible. However the efficiency of the shower quality cut (the cut requiring that no more than half the shower energy is shared) is different for pions and leptons. It must be carefully measured. We estimate the efficiency of this cut for pions by looking at tracks from 2-prong events where the other track in the event was identified as a pion. In Fig. 3.3 we plot the fraction of pions failing the shower quality cut as a function of $z_{\rm LA}$ and momentum. Approximately 10% of all pions fail this cut. Using the lepton calibration samples, we find that approximately 5% of muons and 8% of electrons fail the cut. Because the efficiency differs for pions and leptons and the pion sample defined above contains leptons at low momentum, we estimate the systematic uncertainty associated with the measurement of this efficiency to be 3% below 300 MeV/c, falling to 1% for momenta greater than 500 MeV/c.

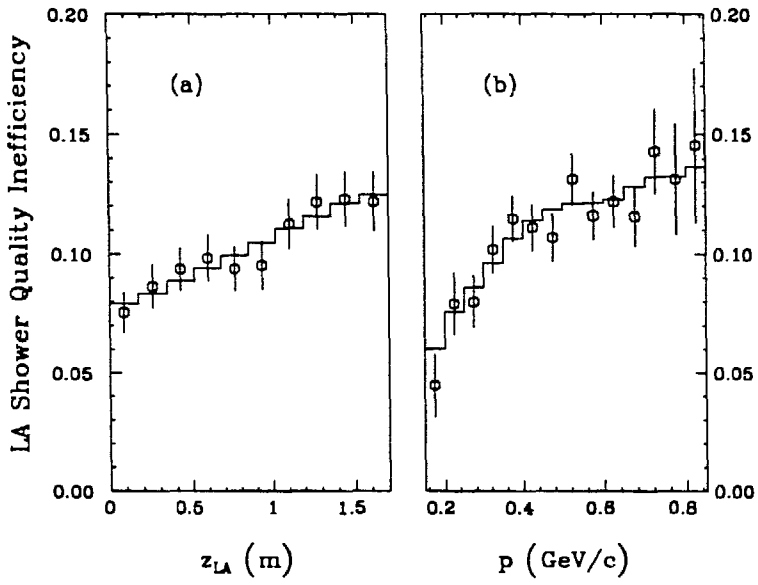

Figure 3.3 *Percentage of pions failing the shower quality cut: (a) as a function of z_{LA}, and (b) as a function of momentum. The histograms are from a fit to the efficiency as a function of both p and z_{LA}. We assume that the efficiency factorizes: i.e. $\varepsilon(p,z) = \varepsilon(p)\varepsilon(z)$. We find no evidence that this is not true.*

3.3.2 Calibration Samples for Pion Identification

In order to measure the pion pair spectrum, we must know the identification efficiency for pions and the residual background from leptons. Two strategies are available to us, each with difficulties to overcome. Using a Monte Carlo simulation, it is possible to study known events and to measure $P_{ID}(\pi, e, \mu)$ to the extent that our detector and its response is adequately modeled. However, we do not have a fully accurate simulation of hadronic interactions. Nor do we believe that the Monte Carlo simulation can be trusted to measure lepton misidentification probabilities that are on the order of 1%. The other strategy is to select events from the data where we can identify tracks as pions, electrons, and muons with reasonable certainty, not using any information from the LA calorimeter. Care must be taken to minimize errors introduced because of differences in the detector environment between simple 2-

prong events and the possibly more complicated events which contain our calibration samples. An additional powerful tool is available to us. In measuring the cross section for pion pairs, we separately determine the efficiencies and backgrounds for events which have one and two pions identified. A comparison between the two independently corrected event samples will either yield an indication of a systematic problem in the identification calibration, or confirm that the calibration was accurate. We use two different sources of calibration pions to measure $P_{ID}(\pi)$.

(1) Pions from K^0_S Decays

Using only information from the DC and VC, it is possible to reconstruct decays of K^0_S mesons into two pions. We use a previously developed Mark II program called VFINDP,[29] to identify tracks as coming from a secondary vertex. The invariant mass distribution after constraining the two tracks to come from the secondary vertex is shown in Fig. 3.4. The background in Fig. 3.4 has been artificially suppressed because only track pairs from events which were on a summary tape enriched in K^0_S decays are included in the plot. However, by looking at the TOF distribution for tracks with momenta less than 300 MeV/c, we can estimate the number of electrons and kaons included in the pion sample. In Fig. 3.5(a), we plot the number of tracks as a function of $\beta - \beta_\pi$ for momenta between 120 and 300 MeV/c, where β_π is the expected velocity if the track is a pion. The fit allows for some miscalibration of the TOF system, and a TOF resolution described by the sum of two Gaussians.

The shape of the contribution from kaons is complicated by the fact that kaons frequently decay in flight. It is determined using a Monte Carlo simulation. Only one track in the calibration sample is identified as a kaon.

At these low momenta it would be possible to observe a shoulder on the distribution due to electron contamination of the sample. None is seen. However the observed distribution is consistent with a contamination of up to 1%.

The only major source of muons in the pion sample that is not also a source of electrons is the decay in flight of pions. Since pions in the wanted 2-prong sample also decay, it is appropriate to include these in the calibration pion sample. The fits in Fig. 3.5 include an estimate of the effect of pion decays. Since muons travel at

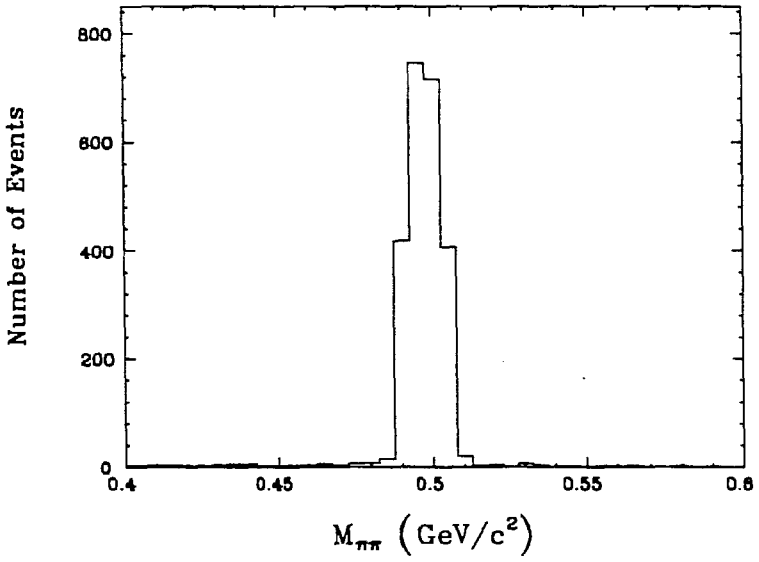

Figure 3.4 *Invariant mass distribution of track pairs forming a secondary vertex*

nearly the same speed as pions of the same momentum, it is not possible to reliably estimate the muon fraction from the fit. However, it is reasonable to suppose that the muon fraction is no worse than the electron fraction. With the above assumption, we find from the fit that the sample is 99% pions.

(2) Low Mass 4-prongs

The cross section for $\gamma\gamma\rightarrow$4-prongs is quite large, and is dominated by $\gamma\gamma\rightarrow 2\rho^0 \rightarrow\pi^+\pi^-\pi^+\pi^-$. To select the $\pi^+\pi^-\pi^+\pi^-$ sample, we apply the following event cuts:

- Events are required to have exactly four charged prongs. No attempt is made to exclude events with neutral tracks, since pion interactions often cause a neutral shower to be found where the scattered pion hit the LA.
- Standard Two-Photon total energy and $\sum p_t$ (net momentum transverse to the beam axis) cuts are made. The sum of charged and neutral energy (excluding SAT tracks) must be less than 7.5 GeV. If there is no SAT track, then $\sum p_t$ must be less than 200 MeV/c. Otherwise, $\sum p_t$ including the SAT track must

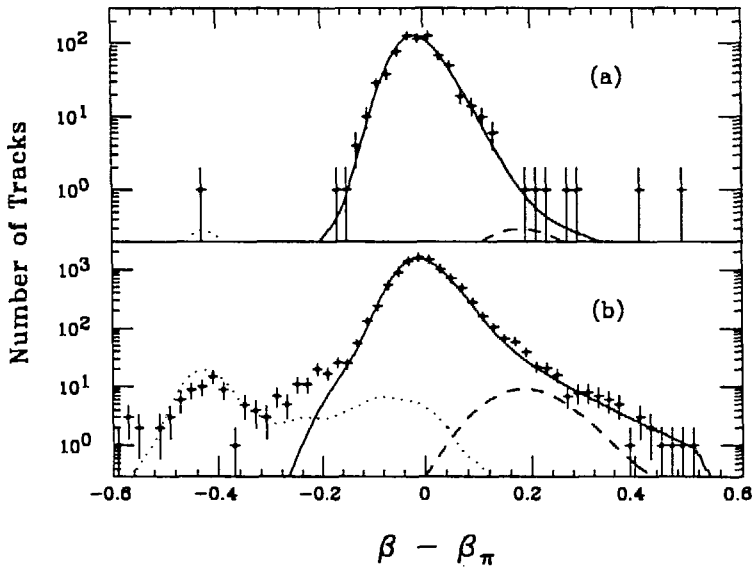

Figure 3.5 *Number of tracks as a function of $\beta - \beta_\pi$: (a) for tracks from reconsructed K^0_S decays, (b) for tracks in the 4-prong sample. The solid curves are the fit contributions from pions. The dotted and dashed curves show the components of the fits due to kaons and electrons respectively. The shape of the kaon contribution is from a Monte Carlo simulation, and includes the effect of kaon decays ($K \rightarrow \mu$ and $K \rightarrow \pi$). No estimate is made for the muon contribution, since muons cannot be distinguished from pions at these momenta.*

be less than 350 MeV/c. The $\sum p_t$ cut must be greater for tagged events because of the worse resolution in p_t of the SAT track.

- Events are searched for track pairs coming from the conversion of a photon. Very loose cuts are made in deciding whether an event contains a converted photon. All events with a track pair that passes the conversion cuts are discarded.
- All events with a track identified by the TOF system as anything other than a pion are discarded.
- Events with a track having a Muon Chamber hit associated with it are discarded.

In Fig. 3.5(b), we plot the distribution in $\beta - \beta_\pi$ for tracks in the $\pi^+\pi^-\pi^+\pi^-$ sample with momenta between 150 and 270 MeV/c. The fit value of the electron fraction is $0.91 \pm 0.32\%$. The largest source of electrons in the 4-prong sample is believed to be 2-prong events containing a photon which converted or a π^0 which underwent a Dalitz decay ($\pi^0 \rightarrow \gamma\, e^+e^-$). In most cases, the vertex of the decay can be reconstructed and the event rejected. Failure to reconstruct the decay is usually due to large multiple scattering. Since this problem is worse for low momentum tracks, we expect that the electron fraction in the 4-prong sample is negligible for momenta greater than 300 MeV/c. The only important mechanism for the sample to contain muons that cannot be estimated from the electron fraction is kaon decay. Generally, this can be estimated by looking at the number of kaons which do not decay. The only time this is not true is for kaons of momentum so low that they virtually all decay, producing muons of momenta between 200 and 300 MeV/c.

For momenta below 1 GeV/c, kaons are reasonably well separated from pions. The criteria for identification of a track as a kaon are that it hit a good TOF counter, and that the kaon weight, W_{m_K}, is at least 90%. The kaon weight is defined by

$$W_K = \frac{g(m_k)}{g(m_\pi) + g(m_K) + g(m_p) + g(m_d)} \tag{3.1}$$

where $g(m)$ is the Gaussian weight for a track to have a particular mass, m:

$$g(m) = \exp\left(\frac{-(t - t_0(m))^2}{2\sigma^2}\right). \tag{3.2}$$

In the above equation, t is the measured time-of-flight, $t_0(m)$ is the expected time if the particle has mass m, and σ is the resolution, which was assumed to be 325 psec.[†]

[†] The TOF resolution deteriorated over time. When they were first installed, the resolution was about 325 psec. This is the number which was used in the event reconstruction program (PASS2) where the TOF weights were calculated. Since the true resolution is somewhat worse, the calculated weights are off. This causes a slight mismeasurement of the kaon contamination, but since the contamination is small ($\sim$1%), a slight mismeasurement does not affect our analysis.

The efficiency for identification of a kaon is measured using a Monte Carlo simulation. Since the true TOF resolution was somewhat worse than was assumed both in the Monte Carlo and in PASS2, we expect the true efficiency to be slightly worse. This known mismeasurement is a negligible contribution to the overall systematic error. In Fig. 3.6 we plot the kaon identification efficiency for tracks which project toward the active region of the LA calorimeter as determined using a Monte Carlo simulation. One can see that very low momentum kaons, which generally decay, can not be identified. Consequently, there could be a sizable number of very low momentum kaons, which decay into muons, and we would not be able to tell. In fact, the cross section for $\gamma\gamma \to K^+K^-\pi^+\pi^-$ is reasonably large near threshold [30], leading us to suspect that there could be some muon contamination. Therefore, we will not use this sample for momenta between 200 MeV/c and 300 MeV/c.

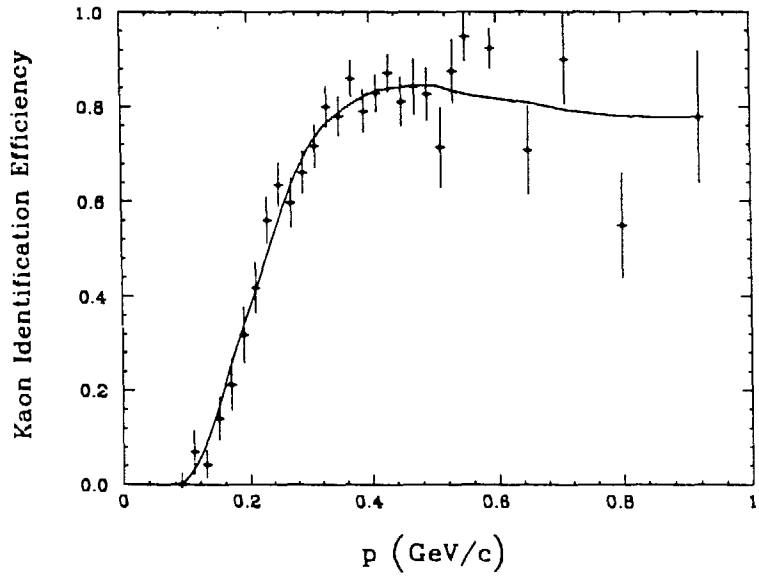

Figure 3.6 *TOF Identification efficiency for kaons projecting toward the LA Calorimeter from Monte Carlo simulation.*

From fits such as the one shown in Fig. 3.5(b), we determine that the fraction

of identifiable kaons present in the 4-prong sample varies between 2% and 4% for momenta between 300 MeV/c and 1 GeV/c. Using the kaon identification efficiency shown in Fig. 3.6, we conclude that the residual kaon fraction after rejecting events with an identified kaon is on the order of 1% in the above interval of momentum. Thus we estimate that the 4-prong sample is at least 97% pions for momenta greater than 300 MeV/c. For momenta below 200 MeV/c, we are dominated by poor statistics, so a muon contamination due to decays of low momentum kaons will cause a mismeasurement of $P_{ID}(\pi)$ by an amount that is small relative to the statistical uncertainty of ~15-30%

3.3.3 Calibration Samples for Lepton Misidentification

It is insufficient merely to have measured $P_{ID}(\pi)$. We must also have samples of electrons and muons in order to measure $P_{ID}(e,\mu)$, so we can understand the background. As for the pions, we use two different sources of electrons.

(1) Electrons from Photon Conversions

Low momentum photons are plentiful in the data. The beam pipe was thin (only .006 radiation lengths), but nevertheless, a finite fraction of the photons convert in the beam pipe into an e^+e^- pair. The algorithm we will use to search for these conversions will also find e^+e^- pairs from Dalitz decays of π^0's. There are numerous neutral pions in the data, 1.2% of which undergo Dalitz decay. Electron pairs from the above sources are found in all kinds of events. Therefore we will search all events, and then apply isolation criteria to the electrons we find in order to minimize the possibility that the measurement of $P_{ID}(e)$ is affected by the presence of other nearby tracks.

When photons convert, the opening angle of the outgoing tracks will generally be very small. In order to search for conversions, we use the following procedure:[27]

- Oppositely charged tracks are projected into the plane transverse to the beam. In this plane, each track is described by a circle. We define the quantity Δ_{xy} as the distance between the two tracks along the line joining the centers of the two circles. As shown in Fig. 3.7, Δ_{xy} measures the minimum distance between the

two tracks when they are parallel. Candidate conversions are required to have Δ_{xy} less than 5 mm. This requirement is also an effective track quality cut that is somewhat more stringent than the requirement that tracks in 2-prong events come within 1.5 cm of the interaction point in the xy-plane. However, since the resolution in the distance of closest approach of a track to the vertex in the xy-plane is better than 1 mm for tracks with momentum in the xy-plane of at least 150 MeV/c, neither cut rejects many tracks.

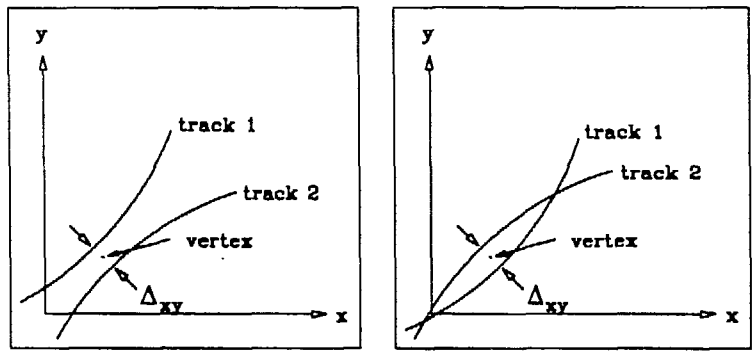

Figure 3.7 *Examples illustrating the definition of the quantity Δ_{xy}, for the cases of (a) non-overlapping and (b) overlapping tracks.*

- The vertex is defined as the point halfway between the two tracks along the line joining their centers (also shown in Fig. 3.7). The tracks must both be within 5 cm of the vertex along the Z-axis.
- The tracks must have the same dip angle within .02 radians.
- Pairs passing all of the above cuts are considered to be conversion pairs. A track from such a pair is included in the calibration sample if no other charged track points toward the same LA module, and if it passes all the other identification track cuts.

In order to estimate the background to the conversion pair sample, we plot in Fig. 3.8 the difference in dip angle for candidate conversion pairs which satisfy the other requirements. We estimate the background from the flat tail of this distribution to

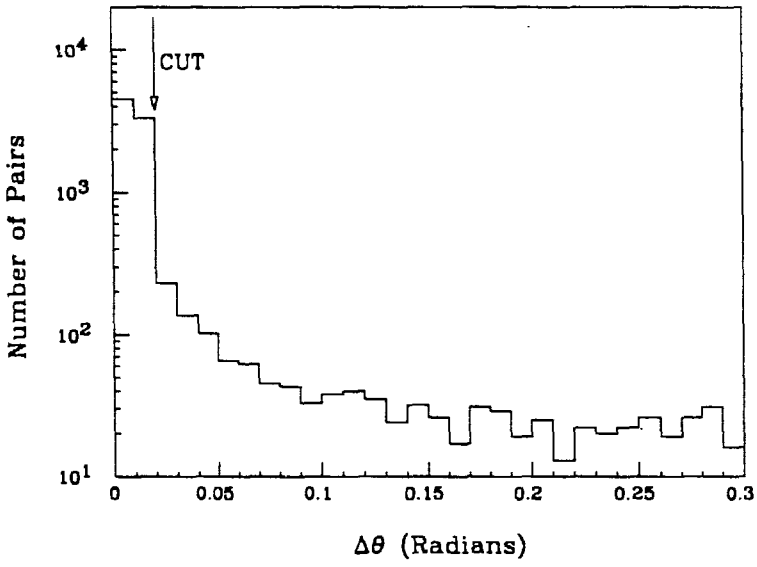

Figure 3.8 *Difference in angle relative to the beam ($\Delta\theta$) of the two tracks of conversion candidates. Pairs with $\Delta\theta < .02$ radians are accepted.*

be less than 1%.

(2) Electrons Identified by the TOF System

Electrons with momentum less than 250 MeV/c can be identified by their Time-of-Flight. Since electron pairs dominate the low mass 2-prong cross section, we can identify such pairs with very little background by requiring that at least one track is identified as an electron. The TOF identification criterion is that the electron weight is at least 95%, where the electron weight is defined analagously to the kaon weight:

$$W_e = \frac{g(m_e)}{g(m_e) + g(m_\pi)} \tag{3.3}$$

where $g(m)$ is as defined in Eqn. 3.2. By fitting to the distribution in t_{1+2} of the events in this sample, we find that it contains approximately 96% electrons, with the remaining 4% being virtually all muons. At the high end of the momentum range (250 MeV/c), where the TOF separation between electrons and muons is smallest,

the contamination from muons rises to ~10%. Since $P_{ID}(\mu)$ is probably comparable to $P_{ID}(e)$, we do not expect that a muon contamination of 10% will cause us to badly mismeasure $P_{ID}(e)$. A similar pion contamination would be disastrous, but since there are far fewer low momentum pions than muons, and since pions are better separated from electrons than are muons, we expect the pion contamination to be less than the muon contamination by at least a factor of 25.†

Muons from Cosmic Rays

In order to measure $P_{ID}(\mu)$, the probability that a muon will be misidentified as a pion, we take advantage of the copious supply of cosmic ray events interspersed in the regular data. Cosmic ray events consist of a single track which passes through the detector, but is reconstructed as two tracks, each coming from near the interaction region. These events look very much like the 2-prong events that are the subject of this analysis, and thus are well-suited for measuring $P_{ID}(\mu)$. We select these events by applying the same cuts as are used to select the $\pi^+\pi^-$ events, with the following modifications:

- Both reconstructed tracks must have Time-of-Flight information associated with them. The Times-of-Flight for the two tracks are measured with respect to a clock signal corresponding to the beam crossing, which is of course uncorrelated with the arrival of the cosmic ray. The individual TOF's are meaningless, but the difference, which is near zero for normal beam interactions, is at least 10 nsec for cosmic ray events. In particular, we require that the measured TOF

† For 250 MeV/c tracks perpendicular to the beam axis, the expected times of flight for electrons, muons, and pions are 5.00, 5.42, and 5.73 nsec respectively. The requirement for identification as an electron is $t < 4.93$ nsec. Assuming a resolution of .5 nsec, a somewhat conservative figure, 27% of muon pairs will have one track identified as an electron, while only 5% of pion pairs will have a track identified as an electron. Since there are at least 5 times as many muon pair events as pion pair events at low momentum, the contamination of the electron sample must include at least 25 times as many muons as pions.

difference is within 1 nsec (about 2 σ) of the expected difference for a cosmic ray muon. Besides selecting only cosmic rays, this cut eliminates protons and kaons up to momenta of 1 GeV/c. Pions could still contribute to the cosmic ray flux.

- Since cosmic rays do not necessarily pass through the origin, we do not make the track quality cut of requiring that the point of closest approach to the origin be within 1.5 cm in the plane perpendicular to the beam, and within 5 cm parallel to the beam. Instead, we make an equivalent cut. We require that the points of closest approach to the origin of the two prongs (which must physically be the same since they are really the same track) agree to within 1.5 cm in both x and y, and to within 10 cm in z.

A 200 MeV/c muon has a range of approximately 50 cm in aluminum. We therefore expect that virtually all muons of at least 200 MeV/c in momentum will pass through the magnet coil and deposit more than 130 MeV in the LA calorimeter. Since we do not expect muons to scatter in the coil, the only way for $E_{\rm LA}$ to be below threshold is if a muon is mistracked – similarly to a pion that scatters, a track that is mistracked will not have all of the energy it deposits in the LA calorimeter included in its associated $E_{\rm LA}$. If this is the only mechanism by which a muon can have $E_{\rm LA}$ below threshold, we can measure $P_{ID}(\mu)$ equally well with either prong of the cosmic ray. In Fig. 3.9 we plot the cosmic ray's $E_{\rm LA}$ for the incoming prong *vs.* the outgoing prong. Because the cosmic ray is losing energy as it traverses the LA and the magnet coil, we cannot necessarily expect the behavior of the two prongs to be the same. In fact, one might well expect that since a cosmic ray must pass through the LA in order to enter the tracking chamber, but not necessarily on the way out, that the average energy deposited would be less for the outgoing prong than for the incoming prong. However, we do not see any evidence in Fig. 3.9 that the distribution in $E_{\rm LA}$ is different for the two prongs. One possible reason for this is that the incoming prong can also scatter in the coil so that the projected road in the LA does not contain the actual path of the cosmic ray.

In examinining Fig. 3.9, we notice that there is a large group of events with both

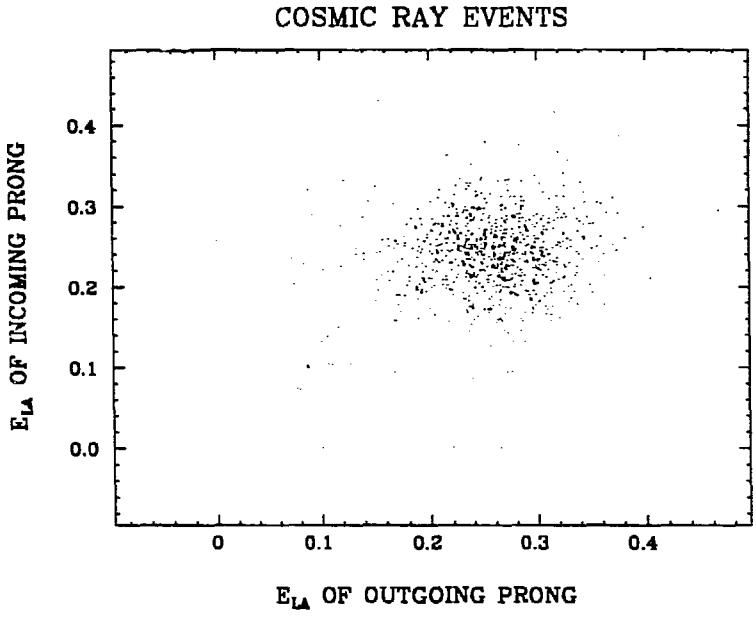

Figure 3.9 *E_{LA} of incoming prong of cosmic vs. outgoing prong for cosmic ray momenta* $250 < p < 400$ MeV/c.

prongs depositing minimum ionizing energy of near 250 MeV, and a smaller group of events where both tracks have E_{LA} less than 130 MeV. This leads us to suspect either that the cosmic ray sample contains pions, or that there is a correlation in the probability that the two prongs of a cosmic muon will have E_{LA} less than 130 MeV. The latter possibility cannot be ignored completely, since the two prongs are the same track, however we were unable to isolate any geometric quantity which showed a strong correlation with $P_{ID}(\mu)$. Turning our attention to the former possibility, we might first ask if it is reasonable to expect that a substantial fraction of low momentum cosmic rays should be pions. At 1 GeV/c, protons make up approximately 3.5% of cosmic rays, decreasing to .5% at 10 GeV/c.[31] Cosmic rays of less than 1 GeV/c cannot be expected to penetrate through to the central part of the detector. In order to observe a low momentum cosmic muon, we needed to start with a primary cosmic muon of a particular energy (about 1 GeV more than is measured in the Drift

Chamber when it first reaches the detector.) However, a proton of any momentum greater than a GeV/c or so can interact in the approximately 1000 gm/cm^2 of detector material it passes through, causing a low momentum pion to pass through the drift chamber. Thus while we expect that the overall hadronic component of the cosmic sample will be less than 3% (probably much less), the hadronic component of low momentum cosmic rays could be much larger than 3%.

By plotting $E_{\rm LA}$ of one prong of a cosmic ray muon versus $E_{\rm LA}$ of the other for several different momentum bins, using the measured value of the probability that a pion has $E_{\rm LA}$ less than 130 MeV from the $\pi^+\pi^-\pi^+\pi^-$ sample, we can fit for both the fraction of pions in the cosmic sample and the probability that a muon has $E_{\rm LA}$ less tha .30 MeV. The results of these fits are presented in Table 3.1. These results show general agreement with the expectations discussed above, but the correlation observed in Fig. 3.9 is even stronger than can be explained by the presence of pions in the sample. This is an indication that there may also be an unexplained correlation in the probabilities that the 2 prongs have $E_{\rm LA}$ less than 130 MeV, or that $P_{ID}(\pi)$ has been mismeasured. It follows that all we can say about the purity of the muon sample is that the pion contamination is no more than that shown in Table 3.1, and therefore that $P_{ID}(\mu)$ is limited on the low side by the values shown in Table 3.1, and on the high side by values determined under the assumption that the cosmic ray sample contains only muons.

3.3.4 Parametrization of $P_{ID}(\pi, e, \mu)$

Using the track samples collected above, we may now choose the cut on $E_{\rm LA}$ to optimize our measurement of the cross section for $e^+e^-\rightarrow e^+e^-\pi^+\pi^-$. In principle, this can be done if we know the cross sections in advance. In practice, however, we will attempt to minimize systematic uncertainty by choosing the cut such that the probabilities $P_{ID}(\pi, e, \mu)$ are not too sensitive to small changes in the cut, while minimizing statistical uncertainty by keeping $P_{ID}(\pi)$ as high as possible and by holding the background down to a fairly small fraction of the final data sample.

Since we have poor statistics on electrons in particular, and severe systematic

Table 3.1 *Results of fit to determine $P_{ID}(\mu)$ and the fraction of pions in the cosmic sample*

p	Total Cosmic Events	Events with 1 prong in pion region	Events with 2 prongs in pion region	$P_{ID}(\pi)$	Fit Pion Fraction	Fit $P_{ID}(\mu)$
.2-.3	1939	145	47	.29	.20 ± .02	0. ± .0016
.3-.5	3922	129	56	.41	.07 ± .01	0. ± .0010
.5-.7	3704	43	9	.25	.03 ± .01	0. ± .0012
> .7	63054	210	2	.20	.0005 ± .0003	.0015 ± .0001

problems with the muon sample, we make an accurate guess that we will be able to determine the leptonic probabilities $P_{ID}(e,\mu)$ to not much better than 50%. (In practice, we do better at some momenta because of our ability to correct $P_{ID}(\pi,e,\mu)$ by requiring that the efficiency corrected distributions of events with one or two tracks identified as pions are in agreement.) Since the leptonic cross section is known to be greater than the $\pi^+\pi^-$ cross section by a factor of at least 10 at low invariant mass ($M_{\pi\pi}$< 700 MeV/c^2), we would have to keep $P_{ID}(e,\mu)$ less than $P_{ID}(\pi)$ by a factor of 10 in order to keep the systematic uncertainty due to background subtraction to less than 50%. At higher mass, the $\pi^+\pi^-$ cross section and the leptonic cross sections are nearly equal. For $M_{\pi\pi}$ near the $f_2(1270)$, if we suppress the leptonic background by a factor of 10, we will keep the error from background subtraction to under 5%.

In Fig. 3.10 we show scatter plots of $E_{\rm LA}$ *vs.* momentum for tracks in the three different calibration samples. The curve shown was selected so as to exclude muons above 400 MeV/c and electrons at lower momenta.

In Fig. 3.11 we plot probabilities $P_{ID}(\pi,e,\mu)$ as a function of momentum as measured using the above samples of electrons, pions, and muons. The data points in Fig. 3.11 are simply the probability that a track in the appropriate calibration sample was identified as a pion according to the criteria shown in Fig. 3.10. The curves shown in Fig. 3.11(a) and (b) result from fits to determine $P_{ID}(\pi)$ and $P_{ID}(e)$ as a function

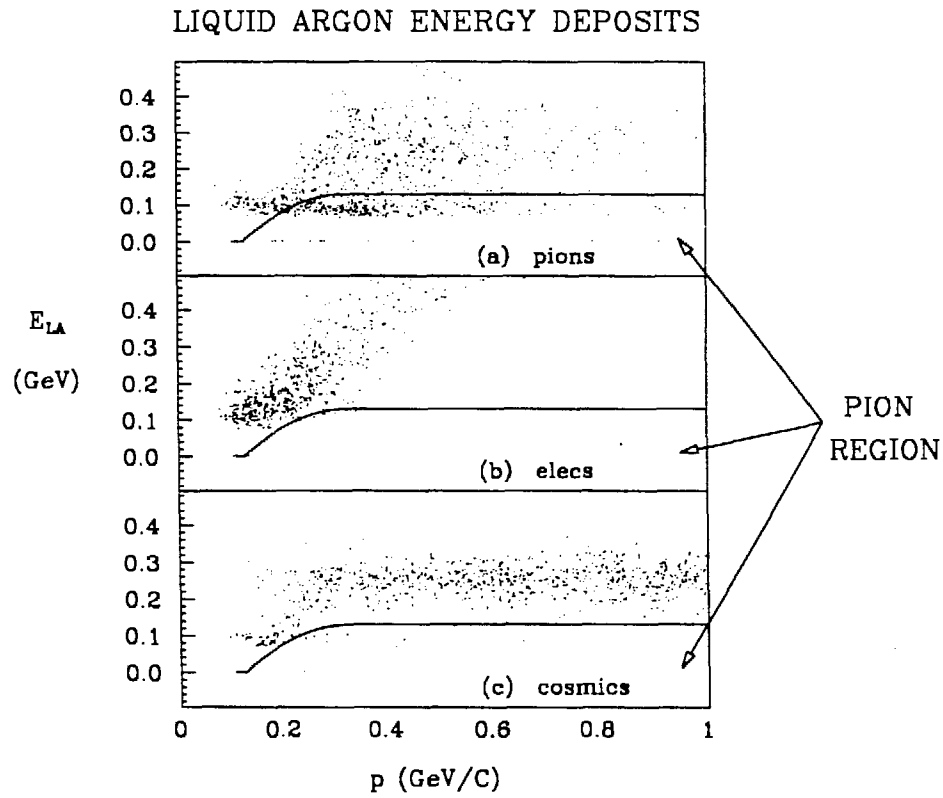

Figure 3.10 *Scatter plots of E_{LA} vs. momentum: (a) pion sample; (b) electron sample; (c) cosmic ray sample. Tracks in the PION REGION, below the curves, are these particles identified as pions.*

of both momentum and z_{LA}. The fits also yield estimates of the uncertainties in $P_{ID}(\pi)$ and $P_{ID}(e)$ which will be used later to estimate the uncertainties in $P_n(\pi\pi)$ and $P_n(ee)$.

As previously discussed, the muon sample probably contains a fair number of low momentum pions, but the exact number is in doubt because of the possibility that some of the excess of cosmic ray events with both prongs identified as pions is due to a correlation in $P_{ID}(\mu)$ (or $P_{ID}(\pi)$) of the two prongs of a cosmic. Eventually, we will resort to adjusting $P_{ID}(\mu)$ by requiring that the final pion pair cross section is the same whether determined from events with one or two pions identified. However, it is

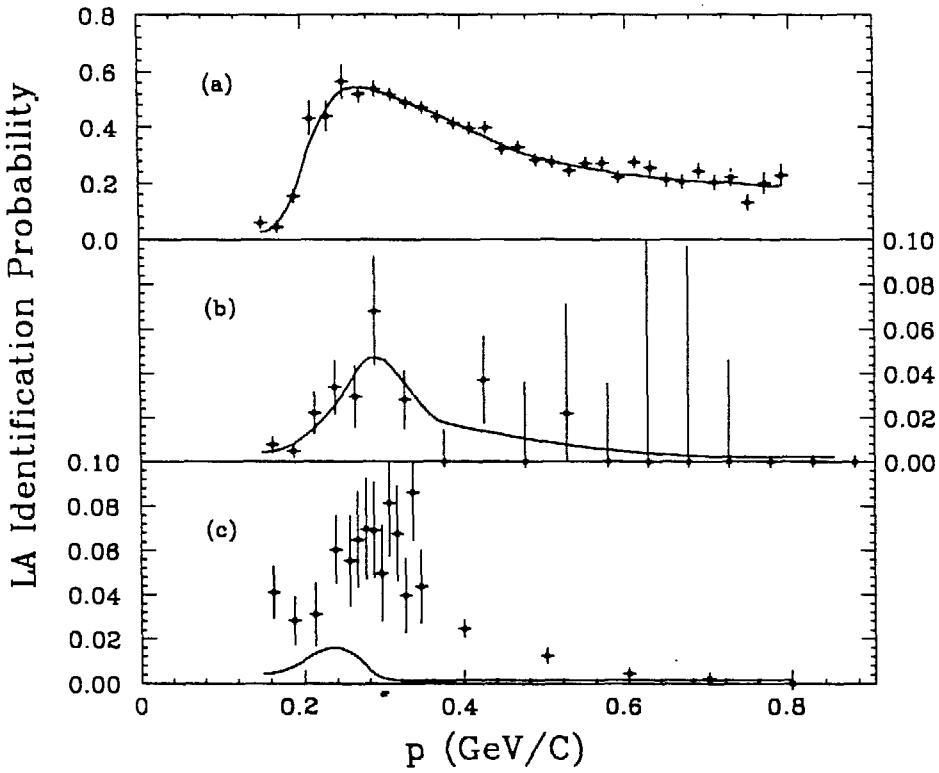

Figure 3.11 *Probability that E_{LA} is in the "pion region" as defined in Fig. 3.10 for tracks in the calibration samples: (a) π's; (b) e's; (c) cosmic ray tracks.*

desirable to make a reasonable estimate of $P_{ID}(\mu)$ and of the uncertainty associated these estimates.

The fit results shown in Table 3.1 give $P_{ID}(\mu)$=0 for momenta between 200 and 700 MeV/c, with a statistical uncertainty of approximately .1%. This value depends on the fit result that all low momentum cosmics with E_{LA} less than 130 MeV/c are pions. This is true only if the two prongs of the cosmic ray behave in a statistically independent but equivalent manner. For higher momenta, the fit indicates that only 10±10% of cosmics identified as pions are actually pions. Therefore the fit value of $P_{ID}(\mu)$=.15% for momenta greater than 700 MeV/c is probably reasonable. To the extent that this represents a finite possibility that the muon was mistracked, low

momentum muons should have at least an equal probability of being misidentified as a pion. Thus one possible first guess is that $P_{ID}(\mu)$=.15% independent of the muon momentum. Another possible first guess is that the probability that a muon is mistracked is the same as the probability that an electron is mistracked, or that $P_{ID}(\mu)$=$P_{ID}(e)$. Since low momentum electrons can radiate a substantial fraction of their energy, making tham more difficult to track, this will probably be wrong, but it is likely to be a valid upper limit, and a reasonable starting point for momenta less than 700 MeV/c. The curve in Fig. 3.11(c) is our initial guess. It is equal to the fit value of P_{ID}(e) at the lowest momenta, and to the limit from cosmic ray muons at higher momenta, with a smooth transition between 200 and 300 MeV/c. The dependence of $P_{ID}(\mu)$ on $z_{\rm LA}$ is assumed to be the same as that of $P_{ID}(e)$. This introduces some additional systematic error, but the uncertainty in $P_{ID}(\mu)$ is already so large, that we are relatively insensitive to the initial guess for $P_{ID}(\mu)$.

3.3.5 Systematic Uncertainties in the Measurement of $P_{ID}(\pi, e, \mu)$

Contamination of the $\pi^+\pi^-\pi^+\pi^-$ sample by other species at levels of 1% will cause a mismeasurement of $P_{ID}(\pi)$ by no more than 1%. Therefore, we will assign a systematic uncertainty in the measurement of $P_{ID}(\pi)$ of 2% due to lepton and kaon contamination. A potentially more serious uncertainty arises from the difference in the overall event environment between 4-prongs and 2-prongs. 4-prong events may have some unspecified number of neutrals depositing energy in various parts of the LA. It is also possible that an interaction of one pion will lead to energy deposit in a section of the LA that a different pion was headed toward. Since the event environment is different for events containing a reconstructed K^0_S than it is for 4-prongs, we estimate this uncertainty by comparing $P_{ID}(\pi)$ as measured using the two different pion samples. In Fig. 3.12 we compare $P_{ID}(\pi)$ for the two samples described above. The only regime in which the efficiency for the two samples appears to disagree is for momenta between 200 and 300 MeV, We previously argued that the $\pi^+\pi^-\pi^+\pi^-$ sample is suspect in this range, and decided not to use it. Otherwise, the two samples give consistent results and allow us to place a limit of 4% on the

difference. Thus we claim that the systematic uncertainty in the measurement of $P_{ID}(\pi)$ using the 4-prong sample is 4%.

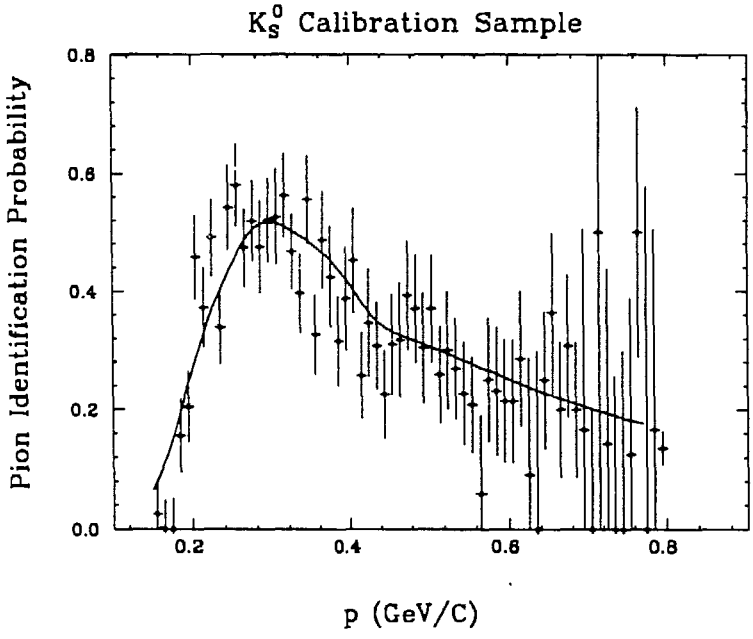

Figure 3.12 *$P_{ID}(\pi)$ as measured using pions from reconstructed K_S^0's. The curve is $P_{ID}(\pi)$ measured with pions from the 4-prong sample.*

Systematic uncertainty in $\sigma(\gamma\gamma \rightarrow \pi^+\pi^-)$ due to the measurement of $P_{ID}(e)$ is dominated by the statistics of the electron sample and by the uncertainties associated with the parametrization of $P_{ID}(e)$ as a function of momentum. We estimate it at 25%. Uncertainty in $P_{ID}(\mu)$ is more difficult to estimate, because of the poorly known pion contribution to the cosmic ray sample. We take it to be 100%.

Chapter 4. NORMALIZATION

When measuring cross sections, one must know the luminosity. At the Mark II, we measure the luminosity by looking at wide angle Bhabha's[32]. The total luminosity for the data used in this analysis is 209 pb^{-1}. We must also know the efficiency of the analysis. In this thesis, the pion pair cross section is measured for three distinct regions of $M_{\pi\pi}$, summarized in Table 4.1. The low mass analysis includes the mass range covered by both the TOF identified pairs and the LA identified pairs. The cuts, and therefore the efficiencies are different for the three mass regions, but many of the factors are the same.

Table 4.1 *Range of $M_{\pi\pi}$ covered in the different analysis regions*

ANALYSIS NAME	REGION OF $M_{\pi\pi}$ (GeV/c^2)
High Mass Analysis	1.7 – 3.5
Low Mass Analysis	.35 – 1.6
(a) TOF Identified Pair Analysis	.35 – .40 MeV/c^2
(b) LA Identified Pair Analysis	.54 – 1.6

The efficiency ($\mathcal{E}_{event}$) is the probability that a produced event will be included in our final event sample. $\mathcal{E}^{\rm LA}$ and $\mathcal{E}^{\rm TOF}$ refer specifically to the LA and TOF identified pair analyses. $\mathcal{E}_{event}$ naturally divides into four factors:

$$\mathcal{E}_{event} = \mathcal{E}_{fiducial} \cdot \mathcal{E}_{trigger} \cdot \mathcal{E}_{analysis} \cdot \mathcal{E}_{rowson} \tag{4.1}$$

- $\mathcal{E}_{fiducial}$ is the probability that a two photon event will produce two tracks which reach the TOF counters. This is a requirement for the Mark II charged trigger. It is determined by the kinematics of two-photon interactions, and the

geometry of the detector. Since most two-photon events are boosted along the beam axis, we expect $\mathcal{E}_{fiducial}$ to be small. We use a Monte Carlo simulation to determine it.

- $\mathcal{E}_{trigger}$ is the probability that an event with two tracks in the fiducial volume will trigger. This efficiency cannot be measured using Monte Carlo. We must measure $\mathcal{E}_{trigger}$ for charged tracks in events which triggered independently of those tracks.
- $\mathcal{E}_{analysis}$ is the probability that an event which triggered will be included in the final event sample. It is qualitatively different for the three mass regions, and must be measured separately for each case. In general, we measure $\mathcal{E}_{analysis}$ with the Monte Carlo, but for the TOF identified pairs, it includes two additional factors: $\mathcal{E}_{\rm TOFQ}$ and $\mathcal{E}_{\rm PASS2}$. These represent contributions which cannot be measured with the Monte Carlo, and are discussed later.
- For about half of the data, the voltage in the Drift Chamber was lowered to prevent excessive current draw due to aging wires.† During these periods, the performance of the DC was degraded, causing a loss of efficiency. This additional inefficiency, which we call $\mathcal{E}_{rowson}$, was measured by P.C. Rowson[33] by comparing the data from the "POOR" runs to the data from the "GOOD" runs. By looking at the multiplicity of hadronic events in the two samples, he determined that there was an inefficiency of 10% per track in the worst part of the data. Using Rowson's measurement, we predict that the observed 2-prong cross section for the first 130 pb^{-1} of data, which contain all the BAD runs, should be 12% lower than for the GOOD runs. We have checked this for pion pair masses between 500 MeV/c^2 and 1.5 GeV/c^2. We find agreement with the prediction, independent of $M_{\pi\pi}$. When applied to the full data sample, this yields an overall correction of $\mathcal{E}_{rowson} = .93 \pm .01$.

These factors should be nearly the same for the QED processes $\gamma\gamma \to e^+e^-$ and $\gamma\gamma \to \mu^+\mu^-$ as they are for $\gamma\gamma \to \pi^+\pi^-$. In this chapter, we will discuss each

† This problem was eventually solved by adding oxygen to the gas mixture.

of these factors, and then use them to measure the known lepton pair cross sections as a check on the overall normalization. Where possible, we will determine each of these factors separately for the different species. Occasionally, such as for $\mathcal{E}_{trigger}$, this will not be possible.

4.1 Monte Carlo Simulation

In two photon interactions, the event will usually be boosted along the beam axis. For large boosts, the produced tracks have a small angle with respect to the beam axis (λ). Therefore, we expect $\mathcal{E}_{fiducial}$ to be fairly low. To measure this probability, we use a Monte Carlo event generator called GGDEPA[34] which is based on the equivalent photon approximation convoluted with either the lowest order QED cross section for the production of lepton pairs by real photons, or the Born approximation for pion pair production. This generator used the uncorrected Low formula for the luminosity function, which leads to two problems. The Low formula overestimates the luminosity function by 13-15% for the $\gamma\gamma$ energies in this analysis. Where the normalization of GGDEPA is important, we will simply correct by this factor. The Low formula also fails to accurately predict the $\gamma\gamma$ $\sum p_t$ distribution. The $\sum p_t$ distribution was measured from the data and put into GGDEPA by hand. The overall normalization of GGDEPA has been checked against the theoretical lepton pair cross section:[35]

$$\frac{d\sigma}{d\cos\theta^*} = \frac{2\pi\alpha^2}{W_{\gamma\gamma}^2} \cdot \frac{\beta \cdot (2\beta^2 \sin^2\theta^* - \beta^4 \sin^4\theta^* + 1 - \beta^4)}{(1 - \beta^2\cos^2\theta^*)^2} \tag{4.2}$$

where β is the velocity of either lepton in the center of mass. After correction of GGDEPA by the difference between the Low formula and the more exact luminosity function of Bonneau, Gourdin, and Martin, the normalization is found to agree (within 2%). The $\sum p_t$ distribution was checked by comparing the visible[†] cross section from GGDEPA with the prediction of a more sophisticated generator – G4QQZ0.[36] G4QQZ0 calculates the QED cross section for $e^+e^- \to e^+e^-l^+l^-$ directly

[†] By visible cross section, we mean that both generated tracks are in the fiducial volume defined by the event cuts, and that the $\sum p_t$ is less than 150 MeV/c.

from all contributing lowest order diagrams, and therefore does not use a luminosity function at all. GGDEPA (with corrected normalization) agrees with G4QQZ0 within statistics (2%).

The $\sum p_t$ distribution assumed by GGDEPA has been checked for lepton pairs, but could be different for pion pairs if the $\pi^+\pi^-$ cross section has a different $\sum p_t$ dependence. Because of this, we assign a systematic uncertainty due to the measurement of the efficiency of 5%.

In Fig. 4.1 we plot $\mathcal{E}_{fiducial}$ as a function of $W_{\gamma\gamma}$ and $\cos\theta^*$. As expected, this probability is nearly the same for the different pairs except for the mass dependent threshold. On the other hand, we do expect differences in $\mathcal{E}_{analysis}$ between species. This is primarily because pions occasionally decay, and electrons undergo hard bremsstrahlung. Each of these processes is a species dependent source of inefficiency, because it introduces a kink in the track which makes it more difficult to reconstruct.

The Monte Carlo is also used to measure the detector resolution in $M_{\pi\pi}$ and $\cos\theta^*$. To be wholly accurate, we would have to measure a four dimensional efficiency matrix giving the observed distributions of $M_{\pi\pi}$ and $\cos\theta^*$ as a function of the produced values, to allow us to unfold the underlying differential cross section as a function of $M_{\pi\pi}$ and $\cos\theta^*$ from the measured distributions. However, since the resolution of the detector in $\cos\theta^*$ is quite good, and the angular distributions are reasonably well approximated by GGDEPA, it is sufficient to simply define the efficiency as a function of $\cos\theta^*$ to be the detected number of Monte Carlo events in a given bin of reconstructed $\cos\theta^*$ divided by the number of events generated with the same value of $\cos\theta^*$. Even in a region where the angular distribution is different in the data than it is in GGDEPA (*e.g.* pion pairs near the $f_2(1270)$ resonance), the cross section is slowly changing relative to the resolution. We estimate that in the worst case, we might mismeasure the efficiency in the last bin ($.5 < |\cos\theta^*| < .6$) by as much as 5%. In determining the efficiency as a function of invariant mass, we use the same procedure. Later, in fitting to a theoretical model which may have structure that is small relative to the resolution in $M_{\pi\pi}$, we will smear the theoretical

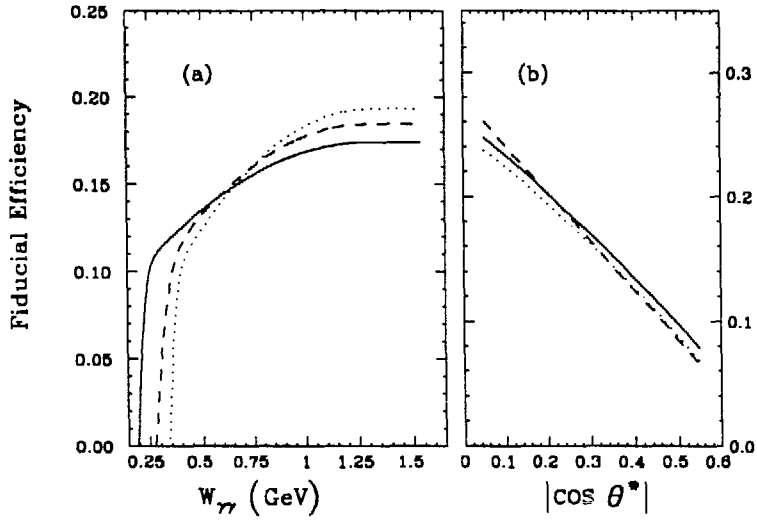

Figure 4.1 *$\mathcal{E}_{fiducial}$ – Monte Carlo probabilities that both tracks project toward the LA calorimeter with $z_{LA} < 1.7$ m, each with $p_t > 100$ MeV/c – (a) as a function of invariant mass ($W_{\gamma\gamma}$) for center-of-mass scattering angles $|\cos\theta^*| < 0.6$; (b) as a function of $\cos\theta^*$ for $W_{\gamma\gamma} > 500$ MeV/c^2. The solid curves are for electron pairs, the dashed curves for muon pairs, and the dotted curves for pion pairs.*

prediction by the measured detector resolution before comparing to the data.

We also use the Monte Carlo to measure $\mathcal{E}_{analysis}$. When looking at data, one usually does not know whether a given event is a pion pair or a lepton pair (except statistically). In the LA identified pair analysis we assume that each event is a pion pair, and calculate all kinematic variables on the basis of that assumption. Therefore, $\mathcal{E}^{\rm LA}_{analysis}$ is measured as a function of $M_{\pi\pi}$for all pairs. In practice, $\mathcal{E}^{\rm LA}_{analysis}$ is measured in conjunction with $\mathcal{E}_{fiducial}$. The combined Monte Carlo efficiency – $\mathcal{E}_{MC}$ (by this we mean the efficiency measured by Monte Carlo, which for the LA identified pair analysis is just $\mathcal{E}_{fiducial}\cdot\mathcal{E}_{analysis}$) is shown for the LA identified pair analysis as a function of $M_{\pi\pi}$ for pion pairs and lepton pairs in Fig. 4.2. Also shown is a fit to the pion pair efficiency. The center curve is the best fit, while the other curves are

the one sigma upper and lower limits on the fit. The systematic uncertainty from the fit varies from 3% to 5% at $\cos\theta^*$=0, and from 5% to 12% at $\cos\theta^*$=.6, for $M_{\pi\pi} >$ 500 MeV/c^2. Comparing Fig. 4.2 to Fig. 4.1, we see can that $\mathcal{E}^{\rm LA}_{analysis}$ is generally in the range of 60-70%.

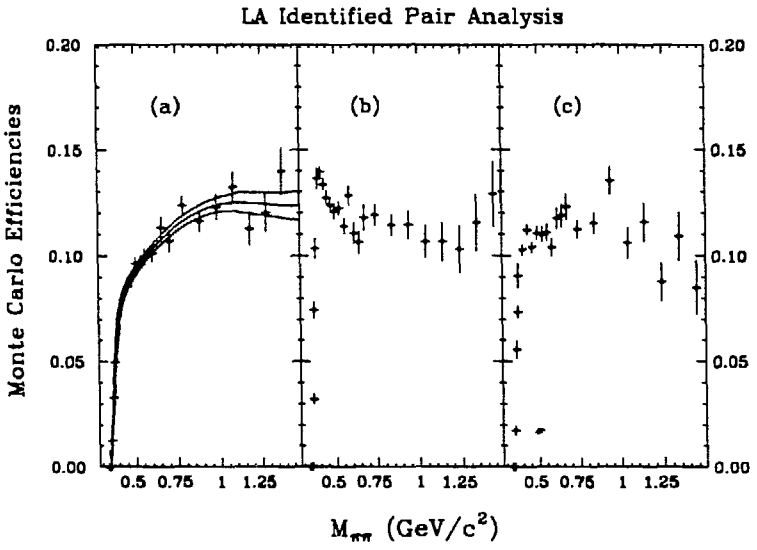

Figure 4.2 $\mathcal{E}^{\rm LA}_{fiducial}\cdot\mathcal{E}^{\rm LA}_{analysis}$ *– Monte Carlo efficiency for (a) pion pairs, (b) electron pairs, and (c) muon pairs as a function of* $M_{\pi\pi}$. *The curves in (a) are a fit to the pion pair efficiency, and the one sigma upper and lower limits on the fit.*

4.2 Trigger Efficiency

The Mark II had several different triggers, but low energy two photon events generally satisfy only the charged trigger. Therefore, we will measure only the charged trigger efficiency. The charged trigger requires that the curvature modules find at least two hardware tracks. A curvature module fires when there is a coincidence of tracking chamber hits and a TOF hit along a road of predefined curvature programmed into the module (see Fig. 2.3). The time of the coincidence provides an initial estimate of the azimuthal angle of the track, with a resolution of about 5°. A hardware track

is found when one or more curvature modules fire at the same azimuth. In order to measure the probability that a charged track will latch (be found by the hardware), we look at 4-prong events. We include only 4-prong events that as much as possible, pass the same cuts as we impose on the 2-prong event sample. We use 4-prong events if they pass the following cuts:

- The event must have a primary vertex.
- The net charge of the event must be 0.
- The $\sum p_t$ of the event must be less than 200 MeV/c. The $\sum p_t$ cut is slightly larger for 4-prongs than for 2-prongs because the $\sum p_t$ resolution is worse for 4-prong events than for 2-prong events.

Tracks from 4-prong events are included in the trigger sample if they satisfy the following criteria:

- Each track must pass the fiducial volume cuts which we apply to both tracks of every event in the 2-prong sample. It must have $z_{\rm LA} < 1.7$ meters, and must come within 1.5 cm of the origin in the xy-plane, and within 5 cm in z.
- At least two of the other tracks in the event must have latched. This ensures that the measurement of the single track latch probability is not biased by the fact that the event triggered.
- We say that a DC track latched if it is within 20° in azimuth of a hardware track, and if it is the closest DC track to that hardware track. We require that the track be at least 40° from all other tracks in the event. This ensures that a hardware track within 20° of that track cannot be associated with any other DC track.

Using the sample defined above, we estimate the latch probability by measuring the probability that a DC track will agree in azimuth with a hardware track (within 20°). In Fig. 4.3 we plot the latch efficiency as a function of p_t, the component of the track momentum in the xy-plane. One can see that it drops off sharply for $p_t < 100$ MeV/c, and that the errors are fairly large. Therefore, to ensure that the trigger efficiency is well known, we will require that $p_t > 100$ MeV/c.

Except for a very small number of runs, the charged trigger required 2 hardware

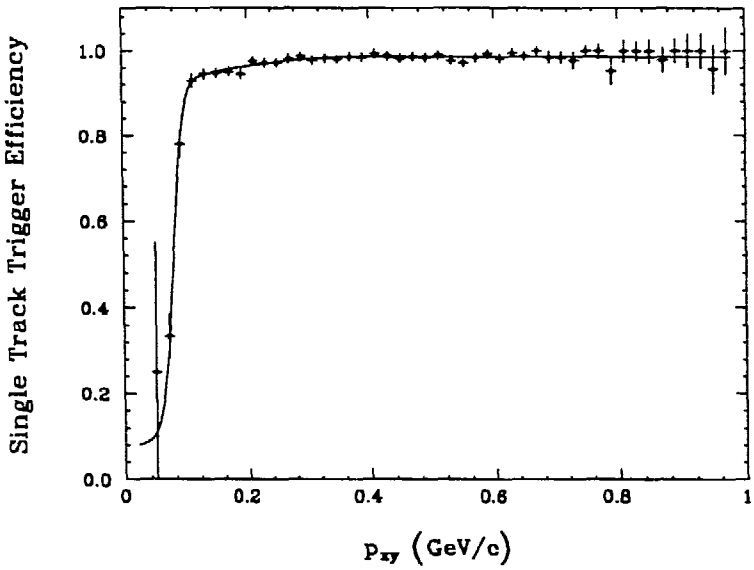

Figure 4.3 *Efficiency for a track to be found by the trigger hardware as a function of p_t. The curve is a fit to the points.*

tracks. Therefore the event trigger efficiency ($\mathcal{E}_{trigger}$) is the product of the latch efficiencies of the two tracks in the event. Since tracks with different p_t contribute to a given bin of $M_{\pi\pi}$ and $\cos\theta^*$, we use the Monte Carlo to determine $\mathcal{E}_{trigger}$ from the p_t spectrum and the single track latch efficiency. This is done by running the Monte Carlo with no trigger simulation. We then weight each event, which has passed all the analysis cuts (including the requirement that $p_t > 100$ MeV/c for each track) by the probability that the event triggered. The efficiency for that bin is then the sum of all the event weights divided by the number of events. In Fig. 4.4 $\mathcal{E}_{trigger}$ is plotted as a function of $M_{\pi\pi}$, averaged over $|\cos\theta^*| < .6$, assuming an isotropic distribution. The two sets of curves are for latch efficiencies measured using two different data samples. † We use the average, which agrees within errors with the individual measurements.

† The dashed curve, which has higher statistics, is measured from 4-prongs selected from two photon summary tapes[37], made using cuts similar to those used in this

The systematic uncertainty is 3% at $M_{\pi\pi} = 400$ MeV/c^2, and 1% for $M_{\pi\pi} > 700$ MeV/c^2.

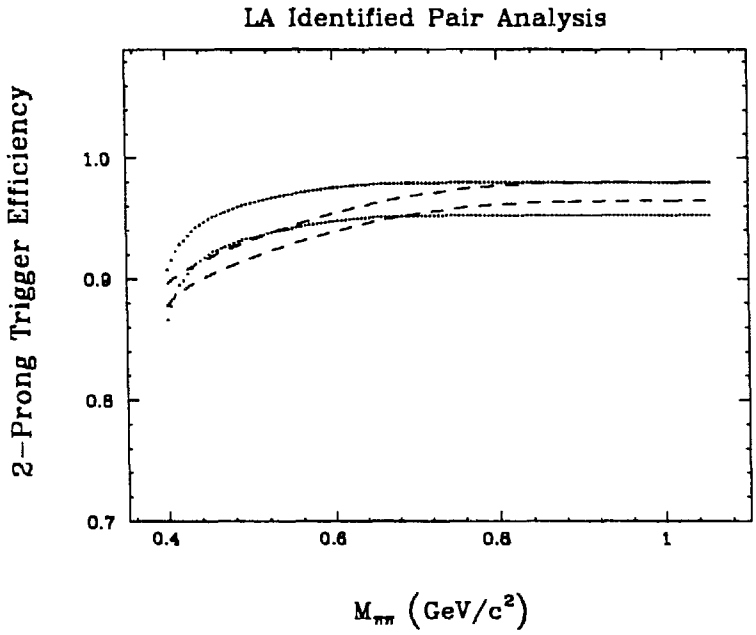

Figure 4.4 *Event trigger efficiency as a function of $M_{\pi\pi}$, averaged over $|\cos\theta^*| < .6$. The pairs of dashed and dotted curves represent the allowed values of $\mathcal{E}_{trigger}$ as determined from two photon summary tapes and for a fraction of the PASS2 and KEEPASS2 tapes respectively (see footnote).*

For $M_{\pi\pi}$ below 400 MeV/c^2, pions are identified by their TOF. The cuts for the TOF identified pion pairs are somewhat different than for the rest of the analysis. In particular, the minimum p_t cut is lowered to 90 MeV/c, and there is effectively a maximum p_t cut imposed by the requirement that pions can be distinguished from muons by their TOF. This puts us in a region where the trigger efficiency is not well known. The trigger efficiencies measured from the two samples of 4-prongs disagree

---

analysis. The dotted curve is from GOOD runs on the PASS2 and KEEPASS2 tapes. The difference, which is consistent with statistics for $p_t > 100$ MeV/c, is taken as an estimate of the systematic uncertainty in the trigger efficiency.

by 10 to 40% in this region. $\mathcal{E}^{\rm TOF}_{trigger}$ is plotted in Fig. 4.5. Once again, we use the average of the two control samples, and assign a systematic uncertainty of half the difference.

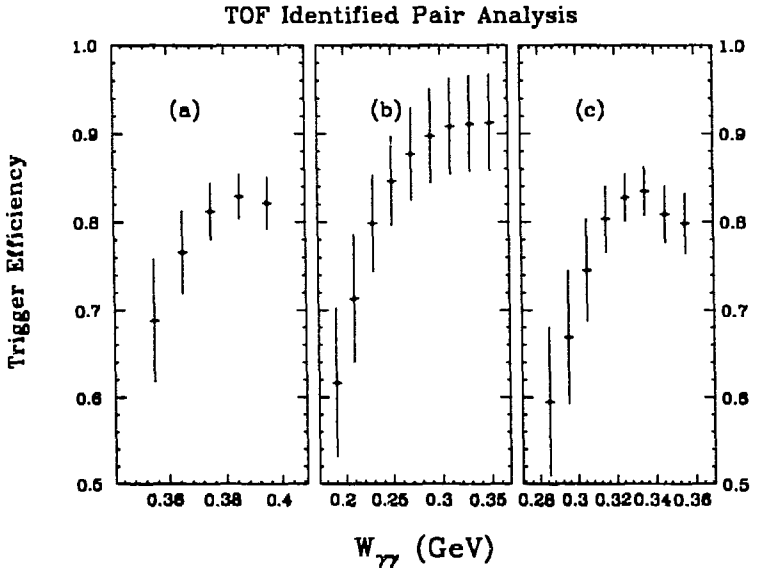

Figure 4.5 $\mathcal{E}^{\rm TOF}_{trigger}$ – *trigger efficiencies for TOF identified pairs: (a) pions, (b) electrons, and (c) muons*

Also shown is $\mathcal{E}^{\rm TOF}_{trigger}$ as a function of lepton pair mass. We attempted to separately determine the trigger efficiency for electrons. There is an indication that the electron trigger efficiency is slightly worse than that determined from looking at the 4-prong sample, which is predominantly pions. By looking at well separated tracks identified[27] as an electron in the LA calorimeter, we find that for p_t between 200 MeV/c and 1 GeV/c, the trigger efficiency for electrons is 3.0 $\pm$ 1.5% worse than for all well separated tracks. However, in order to get statistics, it was necessary to not make event cuts such as were made for the 4-prong sample, and are also made for the 2-prong sample. The result is that the trigger efficiency measured for all tracks in this sample is substantially worse than if tight event cuts are made. The sensitivity

of the measured trigger efficiency to the event cuts, and the impossibility of obtaining a sample of identified electrons using such tight event cuts leads us to guess that the trigger efficiency is the same for electrons as for pions, but to assign a systematic error to the electron pair trigger efficiency of 3% per track (6% per event). This uncertainty is included in the errors shown in Fig. 4.5(b).

4.3 Luminosity from Lepton Pairs

As mentioned in the previous chapter, for very low particle momenta, we can identify muons and electrons with the TOF system. We can also look at the combined lepton spectrum as predicted by Monte Carlo, and compare it to the total 2-prong spectrum with the estimated contribution from pion pairs subtracted. For invariant pion pair masses below 900 MeV/c^2, the contribution to the total 2-prong cross section from pions is expected to be no more than 15%. Therefore uncertainty in the measurement of the lepton pair spectrum due to a conservative estimate of 15% uncertainty in the pion spectrum will be at most 2%. In this section we will first present separate measurements of the lepton pair spectra for $W_{\gamma\gamma} < 360$ MeV, and then a combined measurement as a function of $M_{\pi\pi}$ for $M_{\pi\pi} < 1$ GeV/c^2.

4.3.1 TOF Identified Lepton Pairs

In order to gain statistics on the measurement of lepton pair spectra using the TOF system, we slightly loosen the requirement on p_t of each track. For TOF identified pairs, we accept all tracks with $p_t > 90$ MeV/c. There are also several other cuts specific to the analysis of TOF identified lepton pairs. We require that both tracks hit good TOF counters[†], and that the expected value of t_{1+2} (t_{ll}) is at least 2 nsec away from the expected value for all other mass hypotheses. We also required that the TOF quality was good for both tracks. In particular, the position at which a track hit the TOF counter, as determined from the difference of the signal times at

[†] Three of the 48 scintillators were instrumented at only one end. The resolution for these TOF counters was worse by a factor of $\sqrt{2}$. Therefore we chose not to use them.

the two ends of the scintillator, had to agree with the projected value from the DC track within 25 cm.

We collected data from 168 pb^{-1} of the KEEPASS2 tapes. To determine the number of electron or muon pairs in a given mass bin, we plot $t_{1+2} - t_{ll}$ for all pairs such that M_{ll} (the invariant mass calculated under a given hypothesis) is in that bin, and such that $t_{\mu\mu} - t_{ee}$ for electron pairs or $t_{\pi\pi} - t_{\mu\mu}$ for muon pairs† is at least 2 nsec. We then fit the distribution. Only the peak for the species being measured will be Gaussian. The other peaks will be a sum of Gaussians centered at different distances from the central peak. (The number of pion pairs will be determined in the same way.) An example of such a plot is shown in Fig. 4.6.

In Fig. 4.7 we plot the results of fitting the distributions in $t_{1+2}-t_{ee}$ and $t_{1+2}-t_{\mu\mu}$ as a function of the lepton pair invariant mass. The TOF separation of the species is large enough so that the systematic errors from the fit are less than 5%, which is small compared to other sources of systematic error in this measurement.

Measured cross sections for $\gamma\gamma$ production of x^+x^- pairs to be compared to theoretical cross sections (of Eqn. 4.2 for lepton pairs) as a function of $W_{\gamma\gamma}$ are determined from the detected number N_{xx} of x^+x^- events as follows:

$$\sigma(\gamma\gamma \to x^+x^-) = \frac{dN_{xx}/dW_{\gamma\gamma}}{\mathcal{L} \cdot \mathcal{E}_{event} \cdot d\mathcal{L}_{\gamma\gamma}/dW_{\gamma\gamma}} \tag{4.3}$$

where $\mathcal{L}$ is the luminosity and $d\mathcal{L}_{\gamma\gamma}/dW_{\gamma\gamma}$ is the luminosity function approximated by the Low formula of Eqn. 1.6.

The angular distributions for lepton pairs are well-known. Therefore, we will sum over $\cos\theta^*$ when presenting the lepton pair cross sections. In Fig. 4.8 we plot $\mathcal{E}^{\rm TOF}_{event}$ as a function of $W_{\gamma\gamma}$ for TOF identified lepton pairs. The efficiency for TOF identified pion pairs is also shown summed over $\cos\theta^*$, assuming the angular distribution of the Born approximation. These efficiencies include all the factors mentioned in Eqn. 4.1.

† It can be shown trivially that $t_{\mu\mu} - t_{ee}$ is always greater than $t_{\pi\pi} - t_{\mu\mu}$, so that when analyzing muon pairs, it is sufficient to require $t_{\pi\pi} - t_{\mu\mu} > 2$ nsec in order to ensure that $t_{\mu\mu} - t_{ee}$ is also greater than 2 nsec

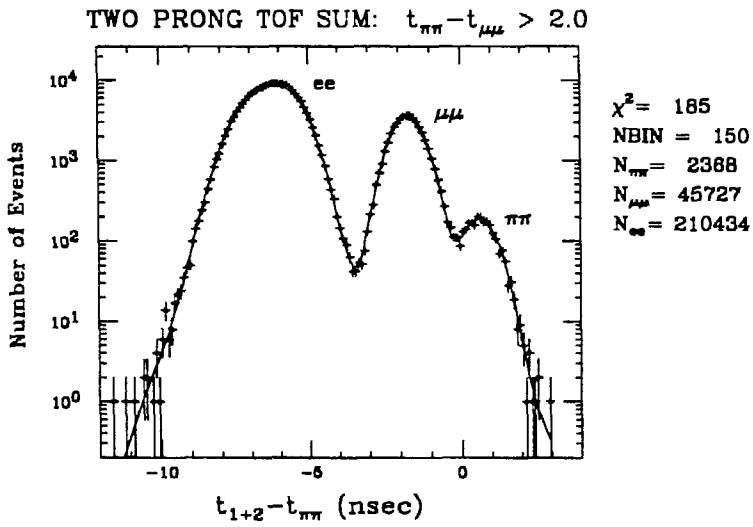

Figure 4.6 *$t_{1+2} - t_{\pi\pi}$ plotted for all pairs such that $350 < M_{\pi\pi} < 400$ MeV/c^2. The results of a fit to determine the number of pion pairs, electron pairs, and muon pairs are shown.*

as well as $\mathcal{E}_{\rm PASS2}$ and $\mathcal{E}_{\rm TOFQ}$, which are specific to the TOF analyses:

- For runs included on the KEEPASS2 tapes, 97% of pairs used in the TOF analysis are on the KEEPASS2 tapes. We have chosen to use only data from these tapes. Therefore, there is an inefficiency due to neglecting the PASS2 tapes. This was measured by looking at a small fraction of the data on the PASS2 tapes. $\mathcal{E}_{\rm PASS2}$ is defined as the efficiency for events to be on the KEEPASS2 tapes. For the TOF analysis, it is 97%.
- We noticed that the TOF quality cut removed more events than expected from the Monte Carlo. Monte Carlo events pass the TOF quality cut 99.5% of the time. For events which fail the cut, the resolution is somewhat degraded, but it is still possible to determine the fraction of electrons, although $\pi - \mu$ separation is no longer possible. By looking at a small sample of the data removed by this cut, we conclude that muon pairs fail the cut 3% of the time, and that

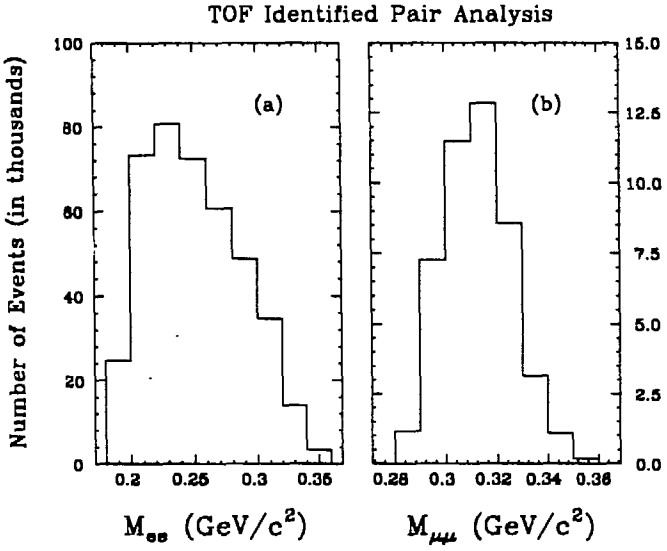

Figure 4.7 *Detected number of (a) electron pairs and (b) muon pairs in 168 pb^{-1} of data*

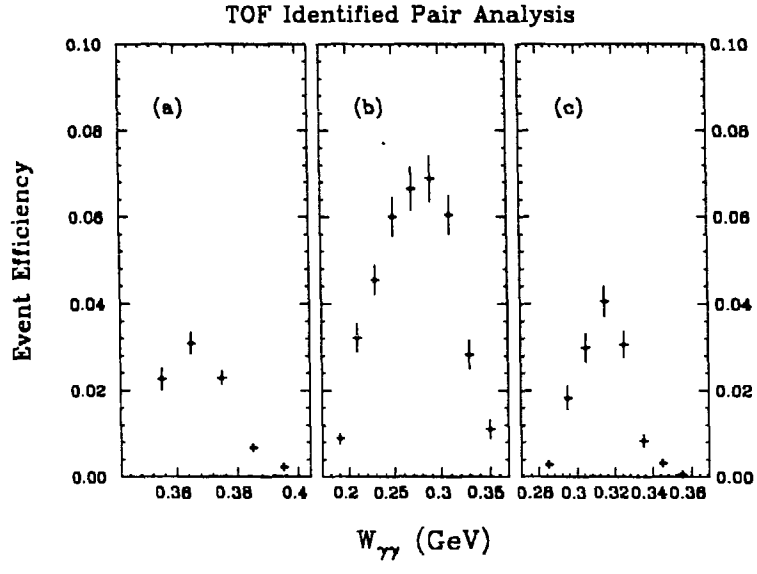

Figure 4.8 *$\mathcal{E}^{TOF}_{event}$ for (a) pion pairs, (b) electron pairs, and (c) muon pairs.*

electron pairs fail the cut 6% of the time. For pion pairs, we take the average

of the above numbers. The efficiency of this cut is called $\mathcal{E}_{\rm TOFQ}$. Corrections and efficiencies used in calculating the measured cross sections from Eqn. 4.3 are summarized in Table 4.2.

Table 4.2 *Corrections and efficiencies used in calculating measured cross sections*

Correction to the Luminosity Function	$d\mathcal{L}_{\gamma\gamma}^{\rm true}/dW_{\gamma\gamma} = .877 \cdot d\mathcal{L}_{\gamma\gamma}^{\rm Low}/dW_{\gamma\gamma}$			
Efficiency Factors	TOF Identified Pair Analysis			LA Identified Pair Analysis
	$\pi^+\pi^-$	e^+e^-	$\mu^+\mu^-$	$\pi^+\pi^-$, e^+e^-, $\mu^+\mu^-$
$\mathcal{E}_{MC}$	0-3%	0-7%	0-4%	10-13%
$\mathcal{E}_{trigger}$	69-83%	62-92%	60-84%	94-98%
$\mathcal{E}_{rowson}$	93%	93%	93%	93%
$\mathcal{E}_{\rm PASS2}$	97%	97%	97%	
$\mathcal{E}_{\rm TOFQ}$	96%	94%	97%	

In Fig. 4.9 we compare the measured two photon cross sections for lepton pair production with the prediction of Eqn. 4.2. The electron pairs fall below the prediction, while the the muons are high relative to the prediction, but the errors are fairly large. One large contribution to the error is from uncertainty in the trigger efficiency. We do not independently measure the trigger efficiency for electrons and muons. However, it is not unreasonable to suppose that muons, which do not decay or radiate, might trigger more efficiently than electrons. The error bars are mostly systematic, and correlated between points, so the overall disagreement with the prediction is not too bad. We find no convincing evidence that the normalization is wrong. A more stringent test on the normalization can be made by looking at the combined lepton spectrum.

4.3.2 Combined Lepton Pair Spectrum

For lepton pair masses higher than in the preceding section, it is not possible to identify electrons and muons by their TOF. However, since the lepton pairs make

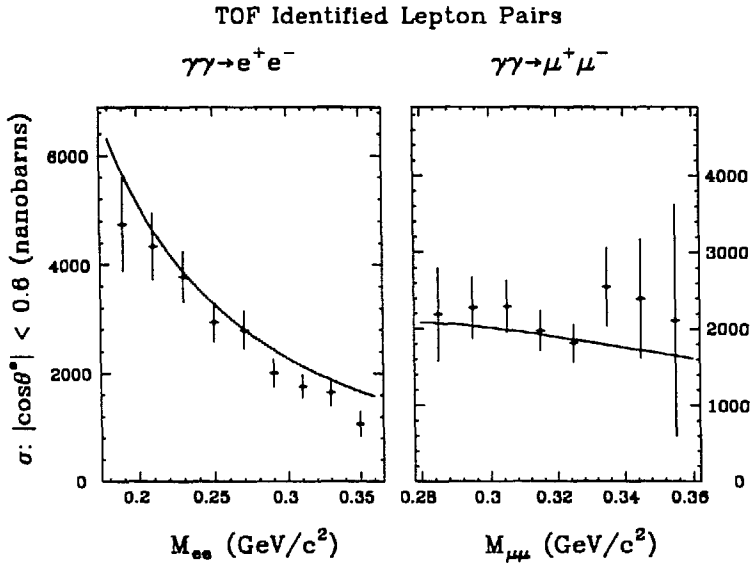

Figure 4.9 *Fully corrected and normalized measured cross sections for two photon production of lepton pairs, using TOF identified electrons and muons. The data are compared with the lowest order QED cross section for the production of lepton pairs by two real photons. The error bars include systematic errors.*

up the vast majority of the 2-prong cross section for masses below 1 GeV/c^2, we can measure the combined lepton pair cross section by simply subtracting the estimated small contribution from pion pairs, and the even smaller contribution from other final states. For the purposes of this measurement, since we must subtract off a contribution from pion pairs that is measured as a function of the pion pair mass, we choose to make this measurement as a function of $M_{\pi\pi}$.

Using the known equivalent luminosity of a Monte Carlo sample of both electrons and muons (4.83 inverse pb^{-1} of electron pair Monte Carlo, and 5.34 inverse pb^{-1} of muons), corrected by the ratio of the true luminosity function to the equivalent photon approximation used in GGDEPA, and multiplied by $\mathcal{E}^{\rm LA}_{trigger}$, we predict the number of leptonic pairs expected in the final data sample (209 inverse pb^{-1}). We then compare this directly to the data, where the contribution from pion pairs (determined later

in this thesis) has been subtracted. The results of this comparison are shown in Fig. 4.10. The normalization agrees strikingly well.

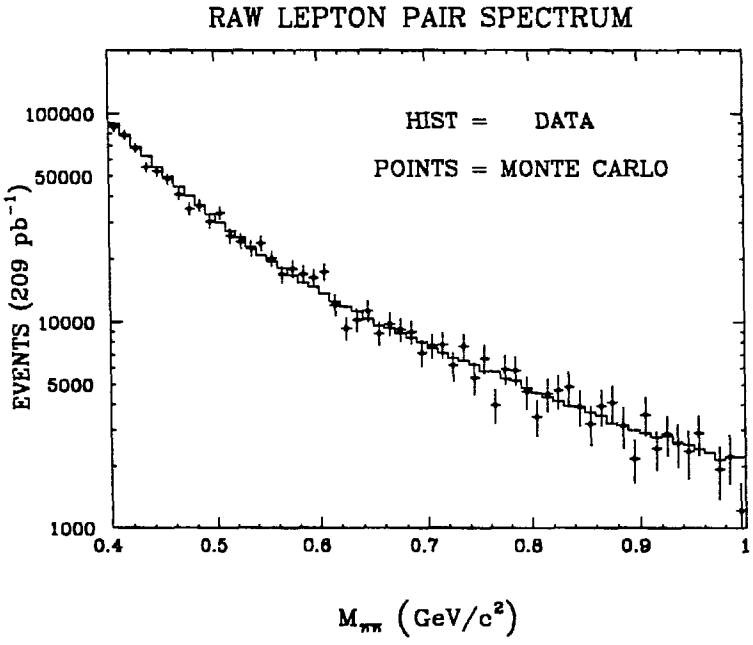

Figure 4.10 *Number of 2-prongs detected, with the contribution from pion pairs subtracted, compared to a Monte Carlo prediction for electron pairs and muon pairs combined.*

Chapter 5. HIGH MASS ANALYSIS

Photon-photon scattering is an excellent testing ground for quantum chromodynamics (QCD). In a QCD model, Brodsky and Lepage[16] have calculated the cross section for the exclusive two-body processes $\gamma\gamma \to h^+h^-$ at large $\gamma\gamma$ invariant mass $\sqrt{s}$ and fixed $\gamma\gamma$ center-of-mass scattering angle θ^*. They assume that the matrix element factorizes into a hard-scattering amplitude and a distribution function related to the pion form factor, whose value is taken from experiment. In particular, their absolute prediction is that near 90° in the $\gamma\gamma$ center-of-mass system,

$$\frac{d\sigma(\gamma\gamma \to \pi^+\pi^-)/dt}{d\sigma(\gamma\gamma \to \mu^+\mu^-)/dt} \simeq \frac{4|F_\pi(s)|^2}{1-\cos^2\theta^*} \sim \frac{0.6\text{GeV}^4}{s^2} \text{ at } \cos\theta^* = 0 \qquad (5.1)$$

Their predictions are rather insensitive to the detailed form of the distribution function.

Previous measurements[1,2] have verified the order of magnitude of the cross section predicted by this model. We have measured† the differential cross section for the combined production of pion and kaon pairs,

$$\frac{d\sigma}{d\cos\theta^*}(e^+e^- \to e^+e^-(\pi^+\pi^-, K^+K^-)) \qquad (5.2)$$

for di-pion masses‡ ($M_{\pi\pi}$) between 1.7 and 3.5 GeV/c^2 with substantially improved statistics. (By "$\pi^+\pi^-$,K^+K^-" we mean $\pi^+\pi^-$ or K^+K^-.) The acceptance of the detector effectively limits us to the large angle region of $|\cos\theta^*| < 0.5$.

---

† This measurement has been previously published[38]. Excerpts are reprinted here verbatim.

‡ All tracks were assumed to be pions. The true mass of kaon pairs is 125-250 MeV/c^2 higher than the calculated pion pair mass for $M_{\pi\pi}$ between 1.7 and 3.5 GeV/c^2.

The basis of the measurement is to use the liquid-argon calorimeters (LA) and the muon system to efficiently reject electrons and muons arising from the QED processes $e^+e^- \rightarrow e^+e^-e^+e^-$ and $e^+e^- \rightarrow e^+e^-\mu^+\mu^-$.

We require events to have two well-measured oppositely charged tracks whose vertex is within 10 cm of the interaction point along the beam direction and within 5 cm in radius. Their total charged energy is required to be less than 40% of $E_{\rm c.m.}$ and their net p_t ($\sum p_t$) must be < 300 MeV/c. Events are rejected if they contain a detected photon that deposits more than 200 MeV in the liquid argon (250 MeV in the end caps), unless the photon is within 40 cm of the nearest charged track, or makes a low invariant mass with either charged track. A photon found within 40 cm of a charged track is assumed to be associated with it, and its energy in the LA is added to that of the charged track. These cuts isolate $\gamma\gamma$ events with a true 2–prong topology. Purely QED processes are then rejected by a series of cuts requiring that both tracks be in a fiducial volume that ensures good muon and electron identification. Neither track may deposit more than 60% of its energy in the liquid argon. This cut ensures that the electron pair contamination is negligible ($< 1\%$). Events are also rejected if either track has enough muon-chamber hits so that it is consistent with the hypothesis that it is a muon.

Efficiencies are determined by generating pion pairs, kaon pairs, and muon pairs with the Monte Carlo event generator GGDEPA[39] and the full detector simulation. The efficiencies were determined as a function of $\cos\theta^*$ and $M_{\pi\pi}$ and were found to vary from 2% at 1.7 GeV/c^2 for $0.3 < |\cos\theta^*| < 0.5$ to 15% at 3.5 GeV/c^2 for $|\cos\theta^*| < 0.3$. For hadrons the efficiency must be corrected for interactions in the coil or LA that cause energy deposited in the LA to surpass the above electron cut. A pure sample of pions from $\psi \rightarrow \rho\pi$ decay (taken at the SLAC e^+e^- storage ring SPEAR) was used to measure the probability that a pion will deposit more than 60% of its momentum in the LA. We find this probability to vary from 50% to 10% over the momentum range $0.2 < p < 1.5$ GeV/c. The same result is used for kaons.

Two estimates are made of the residual muon contamination. First, the Monte Carlo simulation is used to determine the probability that a muon is called a pion.

For the second method we consider events having one identified pion and one identified muon. These are primarily muon pairs with one misidentified track. The small contribution of pion pairs where one pion is called a muon is subtracted by use of the pion-pair Monte Carlo simulation. The ratio of these events to the number of detected muon pair events gives another measure of the probability that a muon is called a pion. Finally, we use the Monte Carlo simulation to determine the detection efficiency for muon-pair events, which together with the above probability and the number of detected muon pair events measures the muon contamination. The resulting corrections agree and range from 2% to 21% with the associated errors approximately half those values. The contamination from $\gamma\gamma \rightarrow \bar{p}p$ is negligible[40]

All events are treated as pion pairs. The number of observed events in each bin, $N(\cos\theta_i^*, M_{\pi\pi_j})$, varies from 62 ($0 < |\cos\theta^*| < 0.3$, $1.7 < M_{\pi\pi} < 1.8$) to 2 ($0.3 < |\cos\theta^*| < 0.5$, $3.0 < M_{\pi\pi} < 3.5$). The efficiencies and the luminosity function[†] are used to determine the cross section $\sigma(\gamma\gamma \rightarrow \pi^+\pi^-, K^+K^-)$ in bins of $M_{\pi\pi}$ for two intervals of $|\cos\theta^*|$. The efficiency for each bin of $(\cos\theta_i^*, M_{\pi\pi_j})$ is taken as a weighted average of the efficiencies for pion pairs and for those kaon pairs which contribute to the same bin when treated as pions. the relative numbers of kaons and pions are calculated from the parent distributions predicted by Ref. 16 and its *Ansatz*, that at fixed $\sqrt{s}$,

$$\frac{d\sigma(\gamma\gamma \rightarrow K^+K^-)}{dt} = \left(\frac{f_K}{f_\pi}\right)^4 \frac{d\sigma(\gamma\gamma \rightarrow \pi^+\pi^-)}{dt} \tag{5.3}$$

with $(f_K/f_\pi)^4 = 2.0$. The weights are proportional to the luminosity function at the appropriate values of $\sqrt{s}$. Since the cross section is a steeply falling function of $\sqrt{s}$, and the invariant mass of kaon pairs contributing to a given bin of $M_{\pi\pi}$ is higher, the expected contributions from pion pairs and kaon pairs are similar for most of the mass range.

The results are shown in Fig. 5.1 compared to the absolute hard-scattering pre-

[†] In the published version of this chapter, we used the Low formula for the luminosity function. In the curves shown in this chapter, we have used the formula of Bonneau, Gourdin, and Martin[24] as discussed in chapter 1

dictions of Ref. 16 integrated over the same two intervals in $|\cos\theta^*|$. While there is good agreement above 2.1 GeV/c^2, there is a discrepancy at lower masses, where the influence of the $f_2(1270)$ is still large. Higher-mass resonances as well as resonance interference with the $\pi^+\pi^-$ continuum can also contribute.

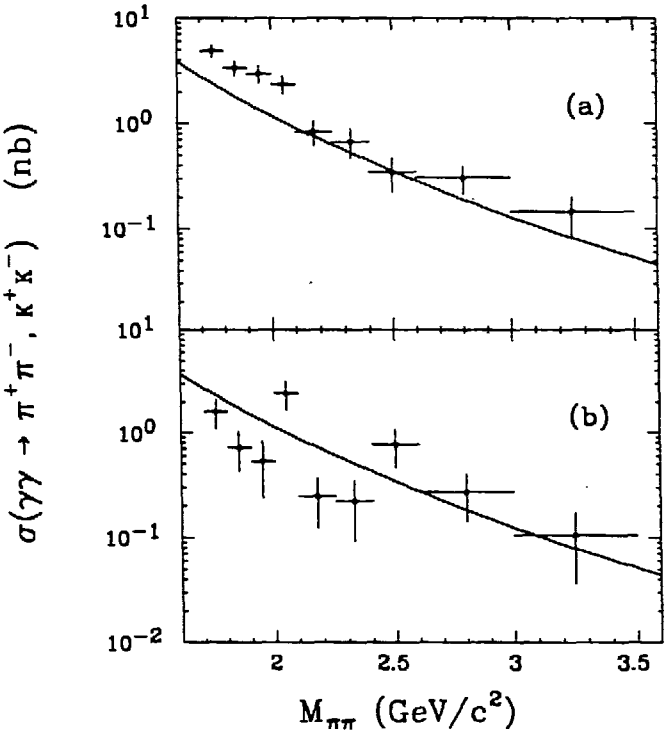

Figure 5.1 *The cross section $\sigma(\gamma\gamma \to \pi^+\pi^-, K^+K^-)$ as a function of the $\pi^+\pi^-$ invariant mass for the intervals of $\gamma\gamma$ center-of-mass scattering angle (a) $0.0 < |\cos\theta^*| < 0.3$ and (b) $0.3 < |\cos\theta^*| < 0.5$. The solid curve is the absolute prediction of Ref. 16. The $M_{\pi\pi}$ region above 2.1 GeV/c^2 contains 48 observed events in (a) and 20 observed events in (b).*

In Fig. 5.2 we replot these same data as a function of $|\cos\theta^*|$. Following Ref. 16, we express the ordinate as the scaling function $s^4 d\sigma/dt$. The limited statistics and angular range prevent us from checking the predicted rise with $|\cos\theta^*|$ in the mass region above 2.1 GeV/c^2. We conclude that, at even relatively modest invariant masses between 2.1 and 3.5 GeV/c^2, the predictions of the QCD model are consistent with our observations. The statistical errors[†] of our measurements are still relatively

[†] Systematic errors were not analyzed in detail for the high mass analysis, but

large, however, and so detailed comparisons of the differential cross section with that expected from QCD will require more data.

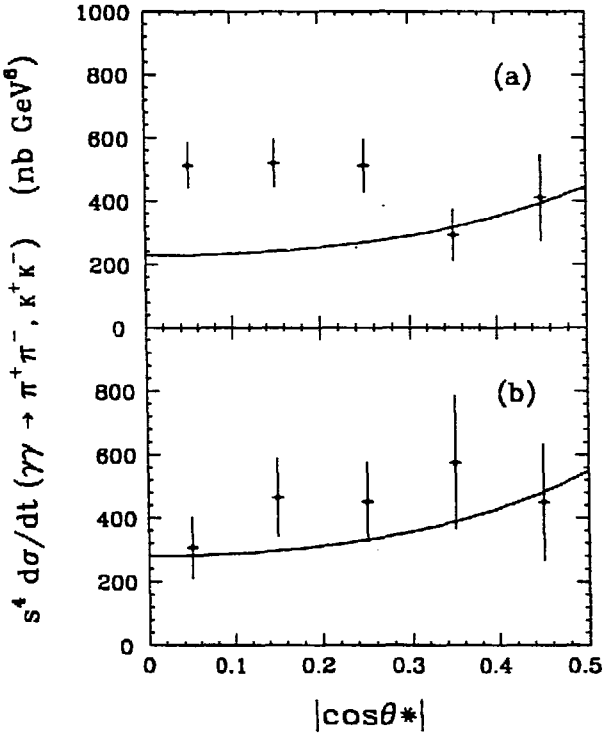

Figure 5.2 *The $\cos\theta^*$ dependens of the scaling function $s^4 d\sigma/dt(\gamma\gamma \to \pi^+\pi^-, K^+K^-)$ for (a) $1.7 < M_{\pi\pi} < 2.1$ GeV/c^2 and (b) $2.1 < M_{\pi\pi} < 3.5$ GeV/c^2.*

---

they are at the 10-20% level, or small relative to the statistical errors for $M_{\pi\pi} > 2.1$ GeV/c^2.

Chapter 6. LOW MASS ANALYSIS

In the high mass regime, we compared the observed hadron pair continuum to a comparatively simple prediction. The situation at lower masses is somewhat more complex. It is well established that the cross section is dominated by a continuum that is in qualitative agreement with the prediction of the Born approximation interfering with the large $f_2(1270)$ resonance. However, our improved statistics allow us to confront a number of important questions about the details of the pion pair spectrum.

One of the features of $\pi^+\pi^- \to \pi^+\pi^-$ scattering experiments is the observation of a scalar resonance near K^+K^- threshold – the $f_0(975)$. One might expect that such an object would have a measureable two photon width. There is recent evidence[12] of this in the neutral channel ($\gamma\gamma \to \pi^0\pi^0$), but statistics are limited. With our improved statistics, we are sensitive to radiative widths $\Gamma(R \to \gamma\gamma)$ as low as a few tenths of a keV. The radiative width of a resonance R is its full width times the branching ratio into $\gamma\gamma$:

$$\Gamma(R \to \gamma\gamma) = \Gamma_R \cdot BR(R \to \gamma\gamma) \tag{6.1}$$

Another experimental question that has been raised is the possibility of a resonance or enhancement to the Born approximation near threshold (below 500 MeV/c^2). We are in a position to shed some light on this issue as well.

In this chapter, we will present the measurement of the pion pair cross section for invariant masses between 350 MeV/c^2 and 1.6 GeV/c^2. We will then compare this data to several theories, and attempt to extract radiative widths for the $f_2(1270)$ and for another possible resonance near 1 GeV for which we observe evidence.

6.1 Event Selection

By event selection, we mean the selection of all exclusive 2-prong events, pion pairs and lepton pairs. Later, we use the particle identification techniques previously

described to extract the pion pairs. The event selection cuts are applied to all of the PASS2 tapes and the KEEPASS2 tapes after the magnetic field was reduced to 2.3 kG. Some cuts were applied in making the KEEPASS2 tapes, but these were duplicated (approximately) in the analysis cuts, so the measured event efficiency is applicable equally to both data sets. Because some data was not included on the KEEPASS2 tapes, we always weight the KEEPASS2 data such that we may use the luminosity of the PASS2 tapes. Combining the two data sets and appropriately weighting the KEEPASS2 events, for the full data sample of 209 pb^{-1}, we accept approximately 1.5 million events with $M_{\pi\pi}$ between 350 MeV/c^2 and 1.6 GeV/c^2. The mass spectrum of these events is shown in Fig. 6.1. One can already see the $f_2(1270)$ resonance over the mostly leptonic background.

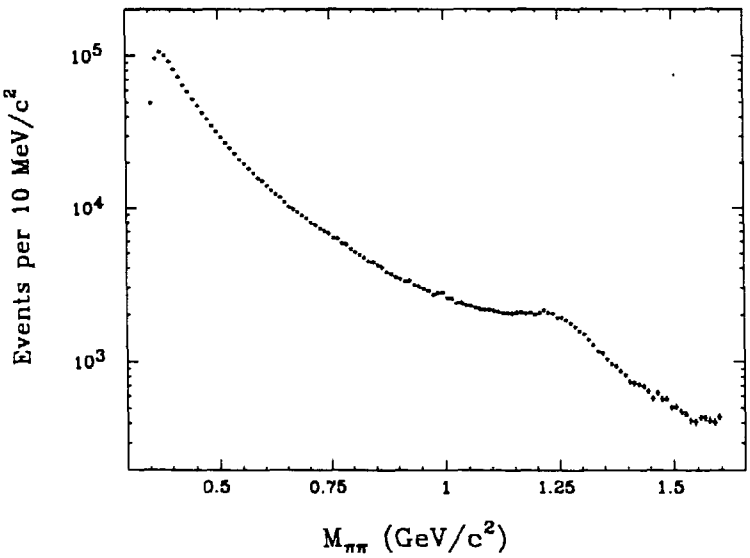

Figure 6.1 *Invariant mass spectrum of all accepted 2-prong events (calculated with all events considered as pion pairs).*

6.2 TOF Identified Pion Pairs

The details of TOF identification of pion pairs have been presented in earlier

chapters. The method closely parallels the TOF identified lepton pairs. The acceptance is a strongly correlated function of $M_{\pi\pi}$ and $\cos\theta^*$. This makes it difficult to extract meaningful information about the angular distribution in this region. We will assume that it is well described by the Born approximation, which is nearly flat for $\cos\theta^* < .6$.

In Fig. 6.2 the distribution in $t_{1+2} - t_{\pi\pi}$ is shown for the 5 bins of $M_{\pi\pi}$ between 350 and 400 MeV/c^2 for which we have wide acceptance. The systematic uncertainty from the fit is due to the tails of the distributions. In the fits, we have allowed for small non-gaussian tails. To estimate the uncertainty, we refit requiring no tails. The resulting values of $N_{\pi\pi}$ are all about 6% higher, but the values of χ^2 are all at least 70 worse for between 120 and 150 bins. Thus we estimate that the systematic uncertainty is no more than 6%. One other possible systematic problem is the effect of pion decays. This is quite difficult to model in a fit, but Monte Carlo simulation indicates that the distribution of pion pairs in $t_{1+2} - t_{\pi\pi}$ is not noticeably assymetric. The only effect is a slight broadening of the curve, which does not cause us any problem.

Most of the systematic uncertainty in the measurement of the cross section comes not from the fit to $N_{\pi\pi}$, but from the measurement of the efficiency (Fig. 4.8), and from the overall normalization. In Fig. 6.3 we show the cross section from TOF identified pion pairs. The error bars include all systematic errors except for the overall normalization. The data are compared to the Born approximation and to the prediction of Morgan and Pennington[17]. The results agree quite well. Other experiments[13–15] have reported an enhancement by a factor of two relative to the Born term in this mass region, however the uncertainties were quite large, so the discrepancy was only one standard deviation. Our data covers the mass range between 350 and 400 MeV/c^2, which corresponds to one point from each of these experiments, and does not confirm such an enhancement. Higher pion pair masses are studied using pions identified in the Liquid Argon calorimeter.

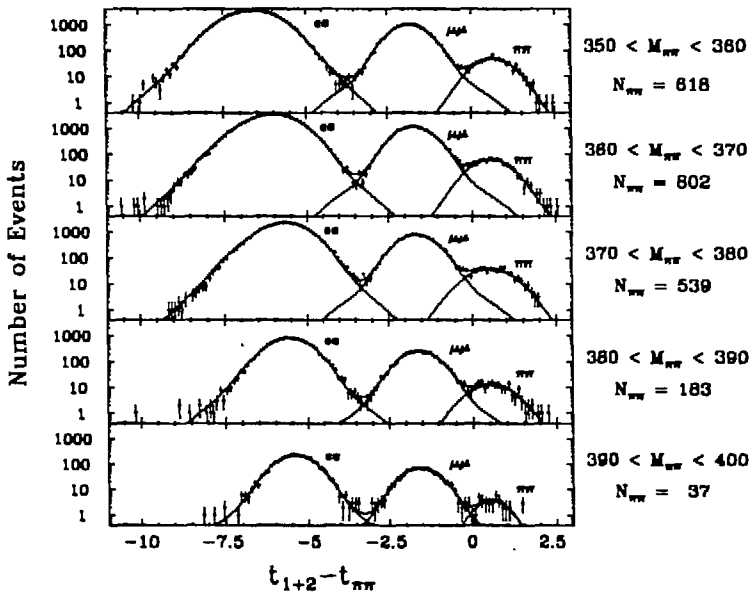

Figure 6.2 *TOF Identified Analysis – $t_{1+2} - t_{\pi\pi}$ distributions are shown for $M_{\pi\pi}$ between 350 and 400 MeV/c^2. Only 168 pb^{-1} of data are included. The curves show the fit contributions from e^+e^-, $\mu^+\mu^-$, and $\pi^+\pi^-$.*

6.3 LA Identified Pion Pairs

In chapter 3, we described LA pion identification procedure. In this section, we separately analyze events with one and two pions identified. (The two identified pion sample is excluded from the one identified to keep the samples independent.) We will use the combined information from the two samples to obtain a more reliable measurement of the pion pair cross section than would be possible using only one sample. We will be able to check and where necessary correct the measurements of $P_{ID}(\pi, e, \mu)$.

In Fig. 6.4 we plot the detected numbers of events in the two samples. We must

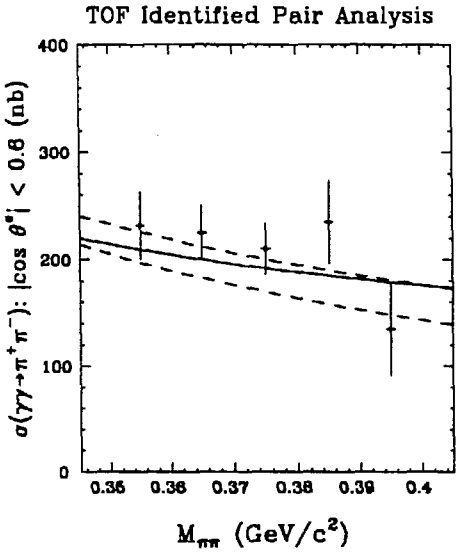

Figure 6.3 *Pion pair cross section from TOF identified pion pairs. The solid curve is the Born approximation. The dashed curves show the allowed values of the Born term plus final state interactions in the model of Morgan and Pennington.*

now subtract the remaining leptonic background, and correct the distributions by the probabilities to identify one or two pions. We have already measured the single track identification probabilities. $P_{ID}(\pi)$ was reasonably well measured, but $P_{ID}(e,\mu)$ were rather poorly measured.

We use the single track probabilities ($P_{ID}(\pi,e,\mu)$) to determine the pair probabilities ($P_n(\pi\pi,ee,\mu\mu)$), that a given number of tracks in each event type will be identified as a pion, as a function of $M_{\pi\pi}$ and $\cos\theta^*$. For each event, we calculate these probabilities as follows:

$$\begin{aligned} P_1(\pi\pi) &= P_{ID}(\pi_1)\cdot(1-P_{ID}(\pi_2)) + P_{ID}(\pi_2)\cdot(1-P_{ID}(\pi_1)) \\ P_2(\pi\pi) &= P_{ID}(\pi_1)\cdot P_{ID}(\pi_2) \end{aligned} \tag{6.2}$$

$P_n(ee,\mu\mu)$ are determined similarly. The pair probabilities $P_n(\pi\pi,ee,\mu\mu)$ are then averaged over all detected events contributing to each bin of $M_{\pi\pi}$ and $\cos\theta^*$. The only implicit assumption in this process is that the distributions over the kinematic variables p and z_{LA} of events in a given bin are the same for pion pairs and lepton pairs. This assumption has been checked with Monte Carlo, and found to be reasonable.

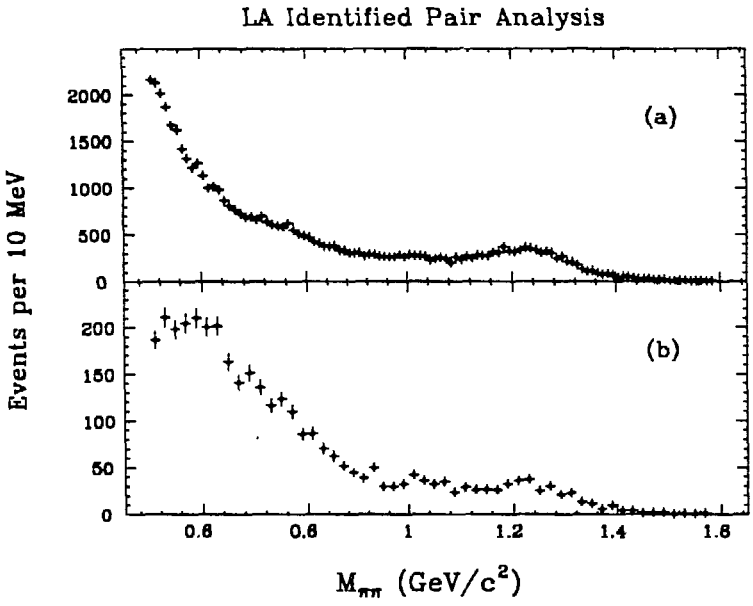

Figure 6.4 *Events with (a) one, or (b) two tracks identified as a pion.*

We must also estimate the uncertainty associated with $P_n(\pi\pi, ee, \mu\mu)$. The averaging process itself is over many events, and so introduces only negligible uncertainty. The uncertainty in $P_{ID}(\pi)$ is known from the fit. For events where both tracks have the same values of p and $z_{\rm LA}$, the uncertainty on the identification probability of the two tracks is completely correlated:

$$\delta P_2(\pi\pi) = 2P_{ID}(\pi) \cdot \delta P_{ID}(\pi) \tag{6.3}$$

However, when p and $z_{\rm LA}$ of the two tracks are different, the uncertainties are at least partially uncorrelated. For partially correlated errors with a correlation coefficient C, we may write the uncertainty in $P_n(\pi\pi)$ as:

$$\delta^2 P_n(\pi\pi) = \partial_i P_n(\pi\pi) \cdot V_{ij} \cdot \partial_j P_n(\pi\pi) \tag{6.4}$$

where, V is the error matrix:

$$V = \begin{pmatrix} \delta^2 P_{ID}(\pi_1) & C \cdot \delta P_{ID}(\pi_1) \cdot P_{ID}(\pi_2) \\ C \cdot \delta P_{ID}(\pi_1) \cdot P_{ID}(\pi_2) & \delta^2 P_{ID}(\pi_2) \end{pmatrix} \tag{6.5}$$

We estimate the correlation coefficient in the following way:

- We alter the measured pion identification probability for each momentum bin and refit. Typically, the new fit will differ only in the vicinity of the bin with the changed point. The details of the way in which the fit changes depend on the parametrization we choose for $P_{ID}(\pi)$. However, to a reasonable approximation, we may describe the change as gaussian of width σ_p in momentum space.
- We may then write the correlation coefficient as

$$C = \exp\left(\frac{(p_1 - p_2)^2}{2\sigma_p^2}\right) \tag{6.6}$$

The uncertainty in $P_n(\pi\pi, ee, \mu\mu)$ is then averaged over all events in each bin of $M_{\pi\pi}$ and $\cos\theta^*$.

6.3.1 *Identification Efficiency Corrected Pion Pair Spectra*

The next step is to use the measured values of $P_n(\pi\pi, ee, \mu\mu)$ to determine the leptonic background and correct for the identification efficiency. We use Monte Carlo to tell us the relative population of electrons and muons in the detected sample. The lepton pair misidentification probability ($P_n(ll)$) is then the average of $P_n(ee, \mu\mu)$ weighted by the relative populations. We define N as the total number of events in a given bin (any number identified, including zero), and $N_{\pi\pi}$ as the number of these events that are pions. The leptonic background N_n^L in the sample with n identified pions is then

$$N_n^L = (N - N_{\pi\pi}) \cdot P_n(ll) \tag{6.7}$$

The detected numbers of events N_n in the samples with n identified pions will be

$$N_n = N_n^L + N_{\pi\pi} \cdot P_n(\pi\pi) \tag{6.8}$$

We may then solve Eqns. 6.7 and 6.8 for $N_{\pi\pi}$ in terms of the measured efficiencies $P_n(\pi\pi, ee, \mu\mu)$ and the detected numbers of events N_n:

$$N_{\pi\pi} = \frac{N_n - N \cdot P_n(ll)}{P_n(\pi\pi) - P_n(ll)} \tag{6.9}$$

This gives us independent measurements of $N_{\pi\pi}$ from the event samples with 1 and 2 pions identified respectively. If $P_n(\pi\pi, ee, \mu\mu)$ have been well measured, the two independent values of $N_{\pi\pi}$ will agree. In Fig. 6.5 we show $N_{\pi\pi}$ as a function of $M_{\pi\pi}$ for the two samples, calculated from Eqn. 6.9. For $M_{\pi\pi} > 750$ MeV/c^2, the distributions agree quite well, but at low masses, where the leptonic background is worst, they do not agree. Therefore, for $M_{\pi\pi}$ greater than 750 MeV/c^2, we may naively combine the samples and use the nominal values of $P_n(\pi\pi, ee, \mu\mu)$. For $M_{\pi\pi}$ below 750 MeV/c^2, we must take a different approach.

We decided instead to fit for $N_{\pi\pi}$, allowing for corrections to $P_n(\pi\pi, ee, \mu\mu)$. To do this, we form a joint χ^2 between the expected and detected numbers of events N_1 and N_2, and between the measured and corrected values of $P_n(\pi\pi, ee, \mu\mu)$. The fit values of $N_{\pi\pi}$ depend crucially on $P_2(\pi\pi)$. For $M_{\pi\pi}$ below 540 MeV/c^2, $P_2(\pi\pi)$ drops rapidly, and the relative uncertainty rises rapidly from just over 10% at $M_{\pi\pi}$= 540 MeV/c^2, to near 50% at 450 MeV/c^2. We conclude that this method is only good for $M_{\pi\pi} > 540$ MeV/c^2. For lower $M_{\pi\pi}$, the LA identification method breaks down. Therefore, we will not be able to measure the pion pair cross section between 400 and 540 MeV/c^2. (Below 400 MeV/c^2, we identify pions pairs with the TOF system.

The uncertainty in $P_{ID}(e, \mu)$ from the unknown makeup of the cosmic ray sample must be estimated. The results of the fit do not depend strongly on this estimate as long as the estimated uncertainties in $P_n(ll)$ are large compared to the uncertainties in $P_n(\pi\pi)$.

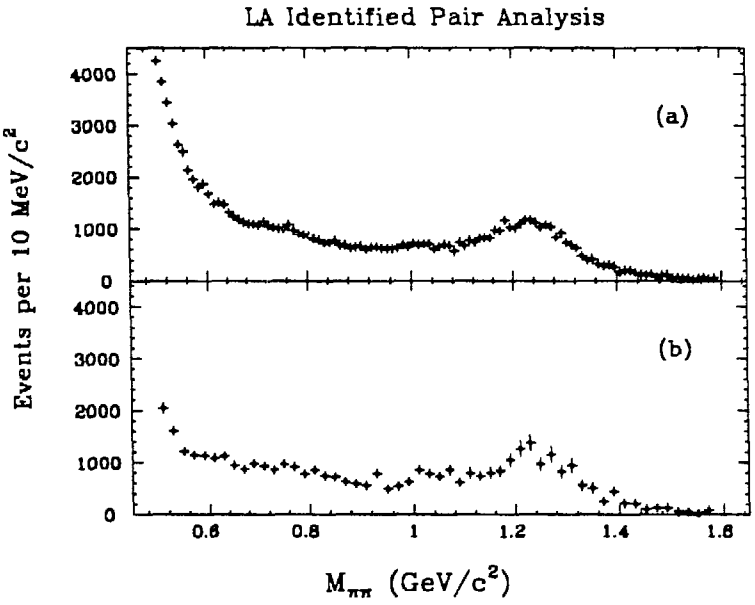

Figure 6.5 *Pion pair spectra calculated from Eqn. 6.9 for samples with (a) 1 track identified as a pion, and (b) both tracks identified. The normalization is to the total number of detected events (not necessarily identified).*

Before fitting, we sum over $\cos\theta^*$ and over several bins of $M_{\pi\pi}$ to gain enough statistics to constrain $P_n(\pi\pi, ee, \mu\mu)$. We assume that any correction to $P_n(ll)$ is applied equally to electron pairs and muon pairs. This assumption need not be true. However, requiring that the correction be applied only to muon pairs changes the answer very little.

As a check on $P_{ID}(\pi, e, \mu)$, we compare the corrected and measured identification probabilities. They agree very well above 750 MeV/c^2, but diverge at lower masses, confirming our decision to use only the fit values of $N_{\pi\pi}$ at lower masses. The fits yield a measurement of $N_{\pi\pi}$ with errors which include the contribution from uncertainties in $P_n(\pi\pi, ee, \mu\mu)$. They are highly correlated, but do give an indication of the systematic uncertainty due to particle identification. The pion pair spectrum from the fit is shown in Fig. 6.6. We now believe that we have correctly subtracted the leptonic

background. We must also consider sources of pion pairs from processes other than $\gamma\gamma \rightarrow \pi^+\pi^-$.

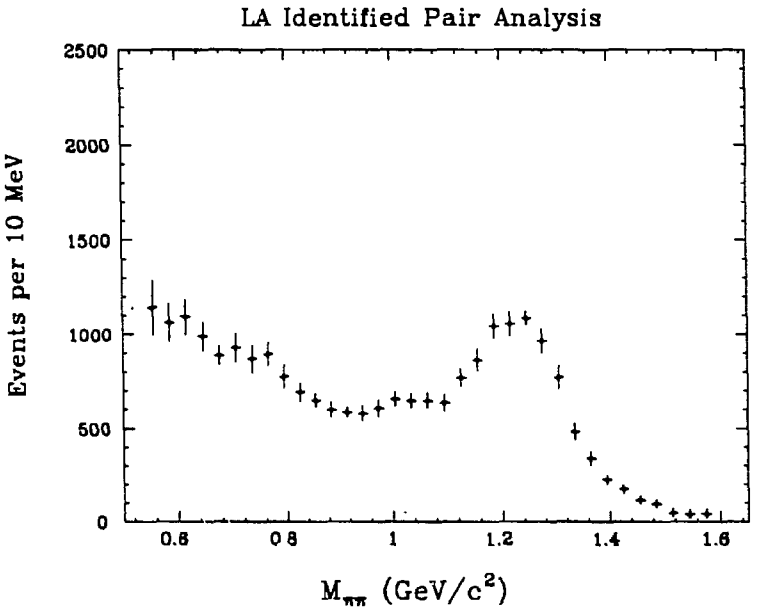

Figure 6.6 *Pion pair spectrum from joint fit to identification efficiencies and the distributions with 1 and 2 identified pions. The errors include the systematic errors from the identification. The normalization is the same as in Fig. 6.5.*

6.4 Hadronic Backgrounds

We have considered a number of possible backgrounds to the exclusive final state pion pairs. We mention only briefly those backgrounds which were determined to be negligible ($< 1\%$ everywhere).

Kaon and proton pairs are rejected efficiently by the TOF cut, and their cross sections are relatively small compared to the pion pair cross section (primarily because of the reduced $\gamma\gamma$ luminosity for kaon and proton pair masses contributing to a given bin of $M_{\pi\pi}$. Both backgrounds are estimated to be less than .1%. Other backgrounds checked with Monte Carlo and found to be negligible include hadronic annihilation events and τ pairs (both annihilation and 2 photon produced).

6.4.1 *Beam Gas Background*

The background from beam-gas events is estimated by looking at the distribution in z of the position of the primary vertex (z_V). Beam-gas events are distributed nearly uniformly in z. Therefore by looking at events with $|z_V|$ greater than 5 cm, we may estimate the beam-gas background. In Fig. 6.7, we plot z_V for events passing all cuts except the z_V cut. One can see a large peak at $|z_V| < 5$ cm over a fairly flat continuum.

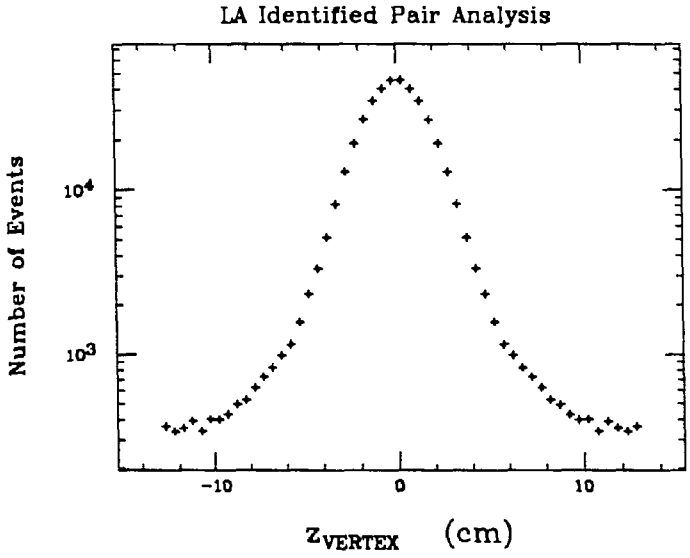

Figure 6.7 *Vertex position along the beam axis for events passing all cuts except for the z_V cut.*

The situation is somewhat complicated by the fact that some real events (*i.e.* e^+e^- interactions) are reconstructed with $|z_V| > 5$ cm. This is due both to non-gaussian tails on the beam spot, which has a nominal resolution in z of 1.5 cm, and to hard scattering in the beam pipe, causing the reconstructed vertex position to be displaced. Neither of these effects are well-simulated by the Monte Carlo. Our method for untangling the beam-gas contribution is to look at the $\sum p_t$ distribution. Beam-gas events have a broad distribution in $\sum p_t$. In Fig. 6.8, we plot the $\sum p_t$ distribution for 3 different bins of z_V. The shape of the $\sum p_t$ distribution for beam-gas events is determined from events with $|z_V| > 10$ cm. The normalization of beam-gas events

for $|z_V|$ between 5 cm and 10 cm is allowed to float. Normally, one would expect that the normalization would be the same, but some events with $|z_V| > 10$ cm were lost because of a cut on the KEEPASS2 tapes which required at least one track to be within 10 cm of the interaction point. We do however expect that the beam-gas normalization will be flat for $|z_V| < 10$ cm.

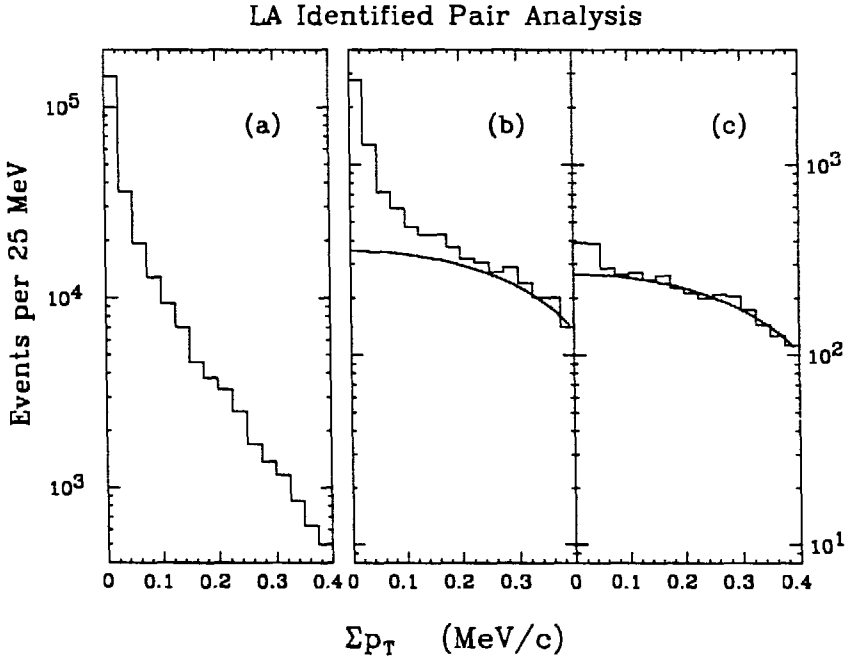

Figure 6.8 *$\sum p_t$ distributions for events with (a) $|z_V| < 5$ cm, (b) 5 cm $< |z_V| < 10$ cm, and (c) 10 cm $< |z_V|$ 15 cm. The curves in (b) and (c) are fits to the contribution from beam-gas events. Only 30 pb^{-1} of data is shown*

To determine the mass dependence of the beam-gas background, we use the shape of the $\sum p_t$ distribution above together with the shape of the $\sum p_t$ distribution of the real events from Fig. 6.8(a) to fit the beam-gas contribution for different bins of $M_{\pi\pi}$. In Fig. 6.9 a we plot the expected number of beam-gas events in the full data sample. The $\cos\theta^*$ dependence of the beam-gas background is found to be isotropic (*i.e.* proportional to $\mathcal{E}_{event}$).

We must also determine the composition of the beam-gas background. To do

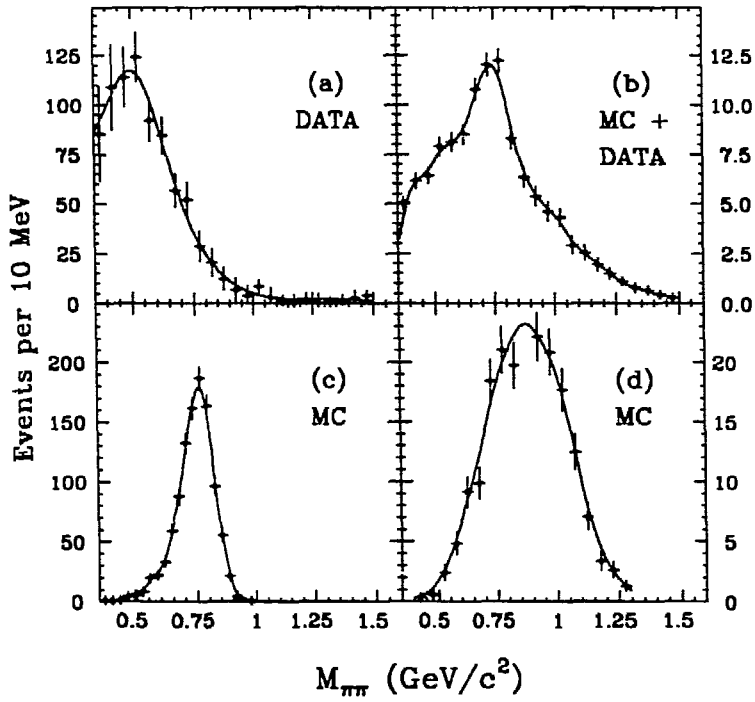

Figure 6.9 *Invariant pion pair mass distributions of hadronic backgrounds: (a) beam-gas data; (b) $\rho^0\rho^0 \rightarrow \pi^+\pi^-\pi^+\pi^-$ (data) + $\rho^+\rho^- \rightarrow \pi^+\pi^-\pi^0\pi^0$ (Monte Carlo); (c) $\eta' \rightarrow \rho^0\gamma$(Monte Carlo); (d) $a_2(1320) \rightarrow \rho\pi$ (Monte Carlo). The normalization is the same as in Fig. 6.5*

this, we fit the data for 5 cm $< |z_V| <$ 10 cm to determine the contributions from pion pairs and lepton pairs. We follow the procedure described earlier for the data, using the observed numbers of events with 0, 1, or 2 tracks identified as pions to fit the pion pair contribution. We find that the fit pion pair spectrum is in agreement with the hypothesis that beam-gas events are all pion pairs. Therefore, we will subtract the unidentified beam-gas spectrum plotted in Fig. 6.9(a) from the identification efficiency corrected pion pair spectrum.

The beam-gas background for TOF identified pion pairs is found by the same method to be about 1%.

One consequence of this method is that we may determine the inefficiency due to the z_V cut. It is about 2%, compared to the Monte Carlo prediction of 1.3%. We correct for this slight difference.

6.4.2 *Background from 4-prongs*

The two photon production of four pions is quite large, and is dominated by the $\gamma\gamma \rightarrow \rho\rho \rightarrow \pi\pi\pi\pi$. This is a background to pion pairs in the case where two pions are missed down the beam pipe, or where two of the pions are neutral. We estimate this background in the following way:

- We determine the mass spectrum of the background by looking at all oppositely charged pairs embedded in 4-prong events. Each pair must satisfy the 2-prong events cuts.
- We must then use a Monte Carlo simulation to normalize the background. To simulate the 4-prong continuum, we create a broad resonance at 1.6 GeV with width .5 GeV, which we force to decay into $\rho^0\rho^0$. We then take the ratio of 2-prong events from this sample to pairs embedded in 4-prong events (from the same sample). This ratio normalizes the $\pi^+\pi^-\pi^+\pi^-$ background. The normalization varies by 50% depending on the angular distribution assumed in the Monte Carlo, but the background is less than 2% at the ρ peak, and less than 1% everywhere else.

The cross section for $\gamma\gamma \rightarrow \rho^+\rho^-$ is lower than for $\rho^0\rho^0$, but the efficiency is slightly higher because the neutral pions may go anywhere. Out of 20,000 generated $\rho^+\rho^-$ events, corresponding to an integrated luminosity of approximately 160 pb^{-1}, 220 events survived the 2-prong event cuts. The resulting background is approximately 1% at 850 MeV/c^2. The shape of the background is approximately the same as for $\rho^0\rho^0$, except that there is no ρ peak. (The charged pions come from different ρ's.) The combined contributions from $\rho^+\rho^-$ and $\rho^0\rho^0$ are shown in Fig. 6.9(b).

6.4.3 *Background from the $\eta\prime$*

We must also consider the background from two photon production of resonances which decay into pion pairs and other neutral particles. The largest of these is the $\eta\prime$. It's dominant 2-prong decay modes are $\eta\prime \rightarrow \rho^0\gamma$ and $\eta\prime \rightarrow \eta\pi^+\pi^-$. Both are determined by Monte Carlo. The $\eta\pi^+\pi^-$ background is negligible above 500 MeV/c^2. It amounts to approximately 5% of the TOF identified pions. The $\rho^0\gamma$ background

is the largest background. It amounts to 20% of the data at the ρ peak. We show the expected background in Fig. 6.9(c). The uncertainty on the background is approximately 20%, and is dominated by the uncertainties in the Monte Carlo $\sum p_t$ distribution and in radiative width of the $\eta\prime$.

6.4.4 *Background from the $a_2(1320)$*

The only other resonance with a large two photon width which decays into two pions plus neutrals is the $a_2(1320)$, which decays predominantly into $\rho^+\pi^-$ (or the charge conjugate). The neutral decay ($a_2(1320) \rightarrow \rho^0\pi^0$) is forbidden. The expected background from the $a_2(1320)$, as determined by Monte Carlo, is shown in Fig. 6.9(d). It amounts to approximately 3% of the data at 850 MeV/c^2.

The fit pion pair spectrum from Fig. 6.6, with all known hadronic backgrounds subtracted is shown in Fig. 6.10.

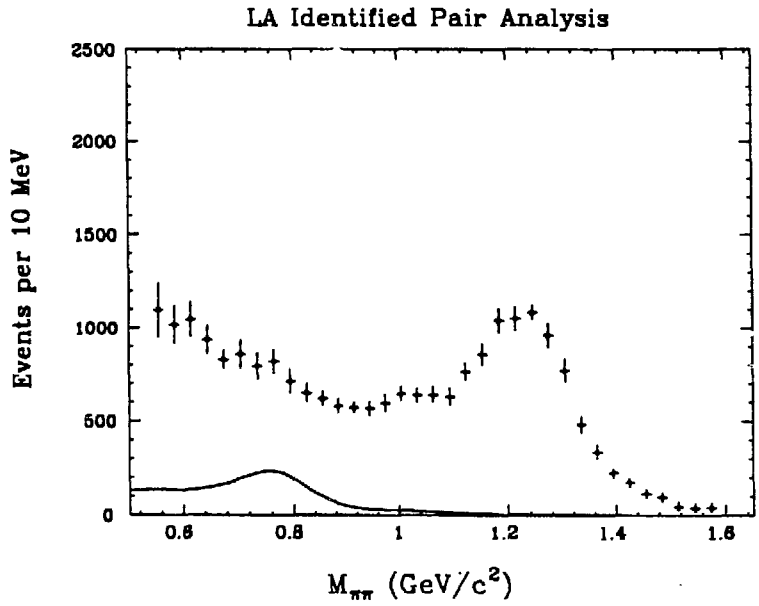

Figure 6.10 *Fig. 6.6 replotted with hadronic background subtracted. The curve corresponds to the subtracted background.*

6.4.5 *Limit on Other Backgrounds*

Backgrounds consisting of two pions plus other particles will have a very different $\sum p_t$ distribution than exclusive pion pairs. For example, 55% of the $\eta\prime$ background has pion pair $\sum p_t$ between 100 and 150 MeV/c, as compared to only 10% of the data. By looking at the $\sum p_t$ distribution as a function of invariant mass, we can place a limit on other such backgrounds to the extent that they have noticeable mass structure. We can also check the reasonableness of the backgrounds we have already subtracted. We consider all events with at least one identified pion. Using the measured pion identification probabilities, we can predict the contribution to this sample from the known backgrounds. In Fig. 6.11, we plot the fraction of the event sample in the $\sum p_t$ ranges 50 to 100 MeV/c and 100 to 150 MeV/c. The histogram is the normalized background which has already been subtracted. One can see that the contribution from the ρ background is quite evident in both $\sum p_t$ ranges. There appears to be some remaining structure, but it is not correlated between Fig. 6.11(a) and Fig. 6.11(b). Any background which, like the ρ, is peaked at high $\sum p_t$, as is expected if there are missing particles, should be visible if it is as large as 10% of the data. We conclude that there is no other such background.

6.5 Predicting the Cross Section for $\gamma\gamma \rightarrow \pi^+\pi^-$

In the low mass regime, we will fit the cross section to a comparatively simple phenomenological model. We will also compare our data to the predictions of some more complex models. Our simple model may violate constraints imposed by theory, some of which the more complex models satisfy, but we will discuss the sensitivity of the measured radiative widths to these constraints. In our simple model, we will describe the non-resonant continuum in the Born approximation. Any bumps are assumed to be resonances which we describe with the relativistic Breit-Wigner formalism.

6.5.1 *The Born Approximation*

In the Born approximation, one assumes a point-like coupling of the photons to charged spin-zero mesons. The calculation then proceeds as in QED, with the

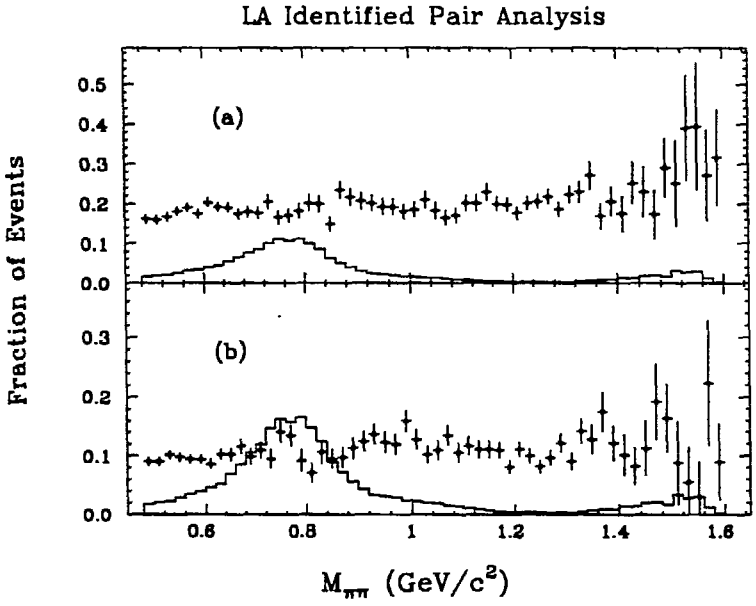

Figure 6.11 *Fraction of pion pair event sample with (a) $50 < \sum p_t < 100$ MeV/c, and (b) $100 < \sum p_t < 150$ MeV/c. The histogram is the ratio of the subtracted hadronic backgrounds (see Fig. 6.9) in each $\sum p_t$ range to the total number of pion pairs shown in Fig. 6.10.*

contributing Feynman diagrams shown in Fig. 6.12. The result of such a calculation is[41]

$$\frac{d\sigma(\gamma\gamma \to \pi^+\pi^-)}{d\cos\theta^*} = |\mathcal{B}_0|^2 + |\mathcal{B}_2|^2$$
$$\mathcal{B}_0 = \frac{\alpha\sqrt{\beta}}{W\sqrt{2}} \frac{1-\beta^2}{1-\beta^2\cos^2\theta^*} \tag{6.10}$$
$$\mathcal{B}_2 = \frac{\alpha\sqrt{\beta}}{W\sqrt{2}} \frac{\beta^2\sin^2\theta^*}{1-\beta^2\cos^2\theta^*}$$

where $\mathcal{B}_2$ and $\mathcal{B}_0$ are the helicity-2 and helicity-0 components (referring to the cases where the spins of the photons are parallel and anti-parallel respectively). This approximation should be valid where final state interactions are negligible, and where the wavelength of the photon is large compared to the size of the pion. Most of our data lies at masses where the above statements do not hold, but it is useful to consider this Born approximation anyway. It has been argued under the hypothesis of PCAC

(partially conserved axial current) and current algebra[42] that the Born approximation should be good up to the vicinity of the ρ mass. Previous experiments[2-13] have indicated that it is reasonable up to the mass of the $f_2(1270)$.

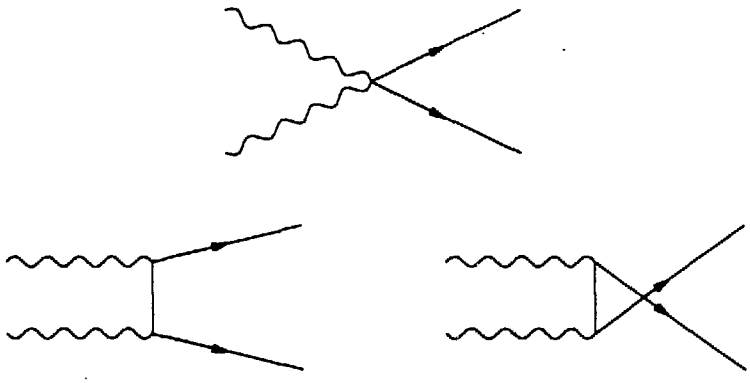

Figure 6.12 *Feynman diagrams contributing to the Born approximation for* $\gamma\gamma \rightarrow \pi^+\pi^-$

We have seen in the previous chapter that for $M_{\pi\pi} < 2$ GeV/c^2, the cross section is not well described by the prediction of Brodsky and Lepage, which covers the region where the photons couple directly to the quarks. The Born approximation has a $1/s$ dependence, while the cross section of Brodsky and Lepage has a $1/s^3$ dependence, due to the additional $1/s$ dependence of the pion form factor. We might expect that we would observe an intermediate behavior in some transition region. In fitting the data, we will allow for the possibility that the continuum has an intermediate s dependence.

6.5.2 *Final State Interactions and Unitarity*

Unitarity applied to $\gamma\gamma \rightarrow \pi^+\pi^-$ leads to an important constraint on the amplitude. It may be written as:

$$\text{Im}\,\mathcal{F}(\gamma\gamma \rightarrow \pi^+\pi^-) = \sqrt{\frac{s-4m_\pi^2}{s}} \sum_n \mathcal{F}^*(\gamma\gamma \rightarrow n)\,\mathcal{T}(n \rightarrow \pi^+\pi^-) \qquad (6.11)$$

where $\mathcal{F}$ and $\mathcal{T}$ are scattering matrix amplitudes of definite spin J and isospin I, and the condition holds separately for all J and I. In the regime where $\pi^+\pi^-$ is the only energetically accessible strongly interacting intermediate state n, this reduces to the requirement known as Watson's theorem[43], which states that for every partial wave of definite spin and isospin, the phase of $\mathcal{F}(\gamma\gamma \rightarrow \pi^+\pi^-)$ must be the same as the phase of $\mathcal{T}(\pi^+\pi^- \rightarrow \pi^+\pi^-)$. If other intermediate states are allowed, the theorem still holds approximately as long as the contribution from other channels is small compared to $\pi^+\pi^-$. For $M_{\pi\pi}$ above the threshold for K^+K^- production, the first other strongly interacting intermediate state, the phase of $\mathcal{F}$ is still constrained, but now in terms of the two amplitudes: $\mathcal{T}(\pi^+\pi^- \rightarrow \pi^+\pi^-)$ and $\mathcal{T}(K^+K^- \rightarrow \pi^+\pi^-)$.

Equation 6.11 is linear in $\mathcal{F}$, so it does not directly constrain the modulus. However, since the amplitude must be unitary, the modulus is contrained in terms of an integral of the phase. Therefore, to the extent that the phase is known, one may predict the modulus. Morgan and Pennington have done this in Ref. 17. They use the measured $\pi^+\pi^-$ phases from hadronic scattering data. They find that the Born term is enhanced near threshold ($M_{\pi\pi} < 350$ MeV/c^2) by about 20% with an uncertainty of 10%, and that it is suppressed for $M_{\pi\pi} > 400$ MeV/c^2 by a similar amount. One may think of this effect as being due to final state interactions. In the vicinity of a resonance, pion pairs are produced via the real Born amplitude, and then resonate in the final state, acquiring the phase of the Breit-Wigner resonance. In this picture, it is not very meaningful to separate the complete amplitude into a resonant and a non-resonant component. One must therefore be very careful what is meant by the radiative width when it is measured in the presence of a continuum with the same quantum numbers.

In the case of $\gamma\gamma \rightarrow \pi^+\pi^-$, the dominant resonance is the spin–2 $f_2(1270)$. It is believed that the $f_2(1270)$ is produced mostly with helicity–2. Our data supports this, as we will show later. In the region of the $f_2(1270)$, the largest component of the Born term is $\mathcal{B}_2$, which is mostly spin–2. In the simplest non-unitarized model, one writes down the expression for a Breit–Wigner resonance, and allows it to interfere with $\mathcal{B}_2$. Since we measure the cross section as a function of $\cos\theta^*$, but use unpolarized e^+e^- beams, the interference between terms of different helicity is zero, but we must include the effect of interference between all terms of the same helicity, even if they have different spin.

In a slightly improved version of the most naive model, where we still wish to preserve the illusion that the cross section can be separated into resonant and non-resonant components, we must come up with a scheme for ensuring that Watson's theorem is satisfied (within limits imposed by the relative amplitudes for $K^+K^- \rightarrow \pi^+\pi^-$ and $\pi^+\pi^- \rightarrow \pi^+\pi^-$). The phase of the combined amplitude must have the phase of the Breit–Wigner, whose parameters have been determined in hadronic scattering experiments. However, Watson's theorem applies only to amplitudes of the same spin. Since the cross section is mostly $I = 0$, $J = 2$, $\lambda = 2$, we will only concern ourselves at this time with the unitarization of this partial wave. Therefore, we must separate out the $J = 2$ component of $\mathcal{B}_2$. This is done by writing $\mathcal{B}_2$ as a linear combination of spherical harmonics $Y_{J\lambda}$, and then multiplying by Y_{22} and integrating. The result is

$$\mathcal{B}_{22} = \frac{15\alpha\sqrt{\beta}\sin^2\theta^*}{16W\sqrt{2}} \cdot \left[\frac{(1-\beta^2)^2}{\beta^3}\ln\frac{1+\beta}{1-\beta} - \frac{2}{\beta^2} + \frac{10}{3}\right] \tag{6.12}$$

Now to apply Watson's theorem, we must modify the phase of either $\mathcal{B}_{22}$ or the Breit–Wigner amplitude. At first, it might seem that there are an infinite number of ways to do this, since the moduli might also be changed. However, we have the more complete model of Ref. 17 to guide us. According to Ref. 17, the correct procedure leads to a modified Born term which disappears at the $f_2(1270)$, guaranteeing that the phase is purely imaginary. Mennessier[18] comes to the same conclusion via a similar

procedure. The effect on the radiative width of the $f_2(1270)$ is that it must be higher than in the most simple model to explain the observed height of the peak.

A different approach is suggested by Lyth[19]. It is somewhat less aesthetically pleasing, but leads to very similar predictions for the radiative width of the $f_2(1270)$. It is also much easier to implement. He allows the coupling for $\gamma\gamma \rightarrow f_2(1270)$ to acquire a phase such that at resonance, the Breit–Wigner amplitude has a real part which precisely cancels the Born term. Aside from the unpleasant aspects of having a complex coupling, this scheme does not guarantee that the phase is correct everywhere. In fact, if one insists that the Born term not be modified, the only way to satisfy Watson's theorem is to modify the $f_2(1270)$ amplitude in such a way that the additional piece exactly cancels the Born term everywhere. This would lead to the conclusion that the cross section is completely resonant, which is absurd: the phase of the spin–2 partial wave is non-zero even below K^+K^- threshold, where we believe that Watson's theorem must be nearly exact, but the cross section is far higher than can be explained by a Breit–Wigner amplitude alone. Despite these difficulties, we find the Lyth scheme to be a convenient way to estimate the effects of unitarity on the radiative width of the $f_2(1270)$.

6.5.3 Parameterization of Breit-Wigner Resonances

A resonance occurs in a partial wave of definite I and J for some scattering process when the phase of that partial wave rises by π radians. In the absence of other amplitudes with the same quantum numbers, the phase passes through $\pi/2$ at the peak of the cross section. The mass of the resonance is defined to be the point where the phase passes through $\pi/2$, and the full width Γ of the resonance is defined such that the cross section falls by a factor of 2 from the peak at scattering energies $\Gamma/2$ away from the peak. The angular dependence of a spin-J, helicity-λ resonance is contained in the spherical harmonic $Y_{J\lambda}$. The mass dependence of a resonance R is given by the relativistic Breit-Wigner:

$$\mathcal{G}(W) = \frac{8\pi(2J+1)}{W} \frac{M_R\Gamma^2(W) \cdot BR(R \rightarrow \gamma\gamma) \cdot BR(R \rightarrow \pi^+\pi^-)}{(W^2 - M_R^2)^2 + M_R^2\Gamma^2(W)} \tag{6.13}$$

For scalar resonances, the full width $\Gamma(W)$ is a constant. However, for higher spin resonances, $\Gamma(W)$ contains an additional mass dependence due to the centrifugal potential which we parameterize[44] as:

$$\Gamma(W) = \Gamma_R \left[\frac{q(W^2)}{q(M_R^2)}\right]^{2J+1} \frac{D_J(q(W^2)\cdot r)}{D_J(q(M_R^2)\cdot r)} \tag{6.14}$$

where

$$q(s) = \sqrt{\frac{s}{4} - m_\pi^2} \tag{6.15}$$

and where r is an effective interaction radius. For the $f_2(1270)$, r is constrained from hadronic scattering data [45]: $r = 5.3 \pm 1.2(\mathrm{GeV}/c)^{-1}$. For tensor resonances, D_J is given by

$$D_2(z) = \frac{1}{9 + 3z^2 + z^4} \tag{6.16}$$

The branching ratios into $\pi^+\pi^-$ are taken from the particle data compilation:[46]

$$\begin{aligned} BR(f_2(1270) \to \pi^+\pi^-) &= \frac{2}{3} \times 0.86 \\ BR(f_0(975) \to \pi^+\pi^-) &= \frac{2}{3} \times 0.78 \end{aligned} \tag{6.17}$$

The factor of 2/3 is the Clebsch-Gordon coefficient for an $I = 0$ resonance to decay into $\pi^+\pi^-$ instead of $\pi^0\pi^0$. The phase δ_R of a resonance is given by:

$$\tan\delta_R(W) = \frac{M_R\Gamma(W)}{M_R^2 - W^2} \tag{6.18}$$

This leaves a phase ambiguity which is irrelevant in the absence of any interfering amplitudes. If there is interference, then the observed peak of the cross section will be shifted. The direction of this shift will resolve the ambiguity. In the case of the $f_2(1270)$ in the $\gamma\gamma \to \pi^+\pi^-$ channel, the resonance is shifted down relative to the known mass from $\pi^+\pi^- \to \pi^+\pi^-$ scattering. This leads us to assign $\delta_{f_2(1270)} = \pi/2$.

We will fit our data using the above parameterization for the $f_2(1270)$. Then we will unitarize according to the scheme suggested in Ref. 19. This will amount to adding a constant δ_B to the usual phase for the $f_2(1270)$ such that at the mass of

the $f_2(1270)$, its amplitude will have a real component (proportional to $\sin\delta_B$) that exactly cancels $\mathcal{B}_{22}$.

In our data, we observe a bump at just over 1 GeV/c^2. The only known resonance which decays into $\pi^+\pi^-$, has mass near 1 GeV/c^2, and has quantum numbers such that it can be produced in $\gamma\gamma$ interactions is the $f_0(975)$. Therefore we will fit our distribution on the assumption that it is the $f_0(975)$. There could be some scalar continuum that causes the observed shift in this channel, but it would have to be substantially larger than the known scalar component of the Born term, even after modification by final state interaction effects. It will turn out that our data is well described by the Born term plus the $f_2(1270)$ plus a scalar resonance (possibly the $f_0(975)$) at a mass of around 1010 MeV/c^2. We leave it to others to speculate as to whether this bump is the $f_0(975)$, or something else. For convenience, however, we refer to it as the $f_0(975)$.

Before moving on to the actual fitting of the data, we will review the current thinking about the $f_0(975)$, and the possibility of a measurable two photon width.

6.5.4 *The S^* Effect*

The $f_0(975)$, formerly called the S^*, was first observed as a sharp rise of the $J = 0$ partial wave in $\pi^+\pi^- \rightarrow \pi^+\pi^-$ scattering. In this channel, the measured phase rises slowly to around $\pi/2$ below the $f_0(975)$, and then quickly through π to $3\pi/2$ near K^+K^- threshold. The effect on the observed cross section is that it dips sharply at resonance. There has been some speculation that the gradual rise below the $f_0(975)$ could be due to a broad σ resonance[17] with mass in the vicinity of 900 MeV/c^2, and width around 600 MeV. This is just a convenient way to fit the observed phase shift. Since we do not constrain the Born term exactly, and since the angular distribution of $\mathcal{B}_2$ is nearly the same as that of a scalar resonance, we are not sensitive to the existence of such a broad low mass object in the channel $\gamma\gamma \rightarrow \pi^+\pi^-$.

The $f_0(975)$ has also been observed in inclusive ψ decays[47]. There it is observed as a peak with mass 972 MeV/c^2.

There is also the possibility that there is more than one resonance in the vicinity.

Originally, the $f_0(975)$ was thought to be a member of the $0^{++}q\bar{q}$ nonet. Some have speculated on the possibilities that it is a $K\overline{K}$ molecule, a 4–quark state, or a glueball. A review of these possibilities can be found in Ref. 48. Whatever it is, or whatever the object we observe is, its $\gamma\gamma$ width is an important probe of its parton content. In particular, most expectations are that a normal $q\bar{q}$ meson would have a radiative width of several keV, while more exotic states should have radiative widths that are smaller by about an order of magnitude.

6.6 Fitting the $\pi^+\pi^-$ Spectrum with Systematic Errors

We fit the gross features of our data first, using the spectrum shown in Fig. 6.6 together with the TOF identified data shown in Fig. 6.3. Fitting these data, which include mass dependent systematic errors, will give a good estimate on the errors of the parameters which describe the continuum. Later we will fit to the sum of the 1–identified and 2–identified data samples in the region where they are most reliable ($M_{\pi\pi} > 750$ MeV/c^2) to determine the best values and statistical errors on the parameters describing the resonances. Systematic errors will be discussed as we go along.

In Fig. 6.13, we show the results of the first fit. For this fit, we fixed the mass of the $f_2(1270)$ at 1274 MeV/c^2, but allowed the mass of the $f_0(975)$ to float. The full widths and branching ratios into $\gamma\gamma$ were allowed to vary. The $f_0(975)$ was assumed to be scalar, and the $f_2(1270)$ was assumed to be a tensor produced wholly in the helicity–2 state. We were unable to obtain a reasonable fit using the unmodified Born term, so we used the following procedure to parameterize the continuum:

- We first modified the Born term so as to make its mass dependence agree with the prediction of Morgan and Pennington. We modify both helicity components in the same way:

$$\begin{aligned} \mathcal{B}'_\lambda &= A_B(s) \cdot \mathcal{B}_\lambda \\ A_B(s) &= A_0 + A_1/s \end{aligned} \tag{6.19}$$

  We reproduce Morgan and Pennington's prediction within their quoted uncertainty for $A_0 = .57$ and $A_1 = .07$. We can fit most of our data reasonably

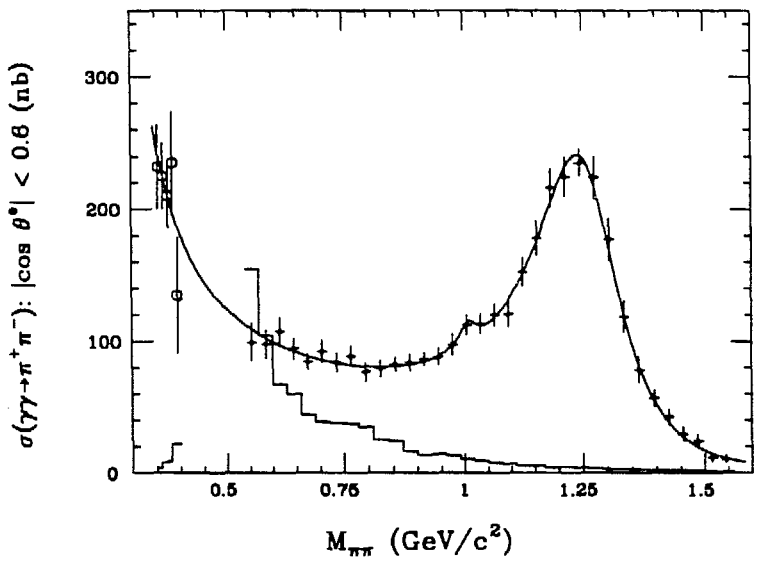

Figure 6.13 *Best fit to the $\pi^+\pi^-$ spectrum with systematic errors included. The large circles are the TOF identified data. The histogram is the subtracted background.*

well using $\mathcal{B}'_\lambda$ for the Born term. However, the mass of the $f_2(1270)$ must be allowed to float in order to get decent agreement.

- Therefore, we allow an additional modification to the Born term:

$$\begin{aligned} \mathcal{B}''_\lambda &= A'_B(s) \cdot \mathcal{B}'_\lambda \\ A'_B(s) &= A'_0 + A'_1 \cdot \sqrt{s} + A'_2 \cdot s \end{aligned} \tag{6.20}$$

This now allows us to obtain the fit shown in Fig. 6.13.

In Fig. 6.14, we compare $\mathcal{B}''_\lambda$ with $\mathcal{B}'_\lambda$ and the nominal Born term. The additional modification we made ($\mathcal{B}''_\lambda$) is slight except at high masses, where one might expect that the continuum would begin to fall off more rapidly because of the onset of a $1/s^3$ mass dependence.

The parameters which produced the fit in Fig. 6.13 are shown in Table 6.1. The errors in Table 6.1 are probably reasonable estimates of the systematic uncertainty on

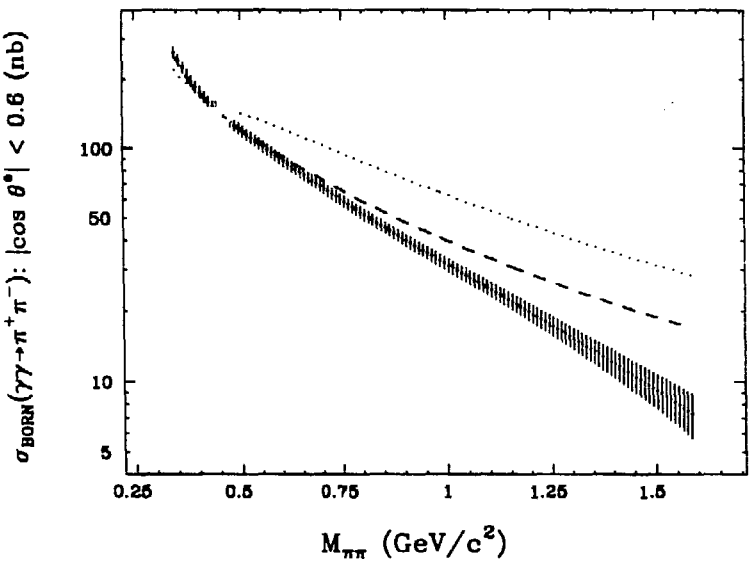

Figure 6.14 *The Modified Born term. The points are the allowed values of B''_λ from a fit to our data. The dotted curve is the nominal Born term, and the dashed curve is B'_λ, the Born term modified to reproduce the prediction of Ref. 17*

A'_i. Since the systematic errors on the points are correlated, the errors on the other parameters are probably overstated. These errors will be discussed more when we fit with statistical errors only.

6.6.1 The Effect of the Mass Dependence of $\Gamma_{f_2(1270)}$

The mass dependence of the full width of the $f_2(1270)$ was parameterized in terms of an effective interaction radius r. For the above fit, we used $r = 5.3$ (GeV/c)$^{-1}$. Hadronic scattering data allows us the freedom to vary r by $\pm$ 1.2. Setting r at 6.5 and 4.1, we find that the fit for B''_λ changes by an amount that is small compared to the errors in Fig. 6.14. The radiative widths change by less than 2%. Thus the systematic uncertainty due to setting $r = 5.3$ is negligible.

Table 6.1 *Parameters of the fit in Fig. 6.13. The errors reflect the systematic uncertainty due to particle identification.*

PARAMETER	VALUE	UNCERTAINTY
A'_0	1.10	0.03
A'_1	0.11	0.02
A'_2	-0.20	0.02
$\Gamma_{f_2(1270)}$	214 MeV/c^2	7 MeV/c^2
$\Gamma(f_2(1270) \rightarrow \gamma\gamma)$	3.33 keV	0.08 keV
$M_{f_0(975)}$	1008 MeV/c^2	18 MeV/c^2
$\Gamma_{f_0(975)}$	47 MeV/c^2	43 MeV/c^2
$\Gamma(f_0(975) \rightarrow \gamma\gamma)$	0.21 keV	.19 keV

6.6.2 The Effect of Unitarity

In the above fit, we have used Lyth's method for satisfying Watson's theorem. If we do not unitarize at all, the only appreciable effect on the parameters is that $\Gamma(f_2(1270) \rightarrow \gamma\gamma)$ decreases by ~13%. Since we believe that Lyth's method gives approximately the right answer for $\Gamma(f_2(1270) \rightarrow \gamma\gamma)$, we claim that the systematic uncertainty due to the unitarization scheme is only 7%.

6.7 Fitting the $\pi^+\pi^-$ Spectrum with Statistical Errors Only

To determine statistical errors on the masses and full widths of the $f_2(1270)$ and the $f_0(975)$, we fit to the sum of the 1–identified and 2–identified samples. We fit only to the TOF identified data (350 – 400 MeV/c^2) and to the LA identified data for $M_{\pi\pi}$ between 750 MeV/c^2 and 1.5 GeV/c^2. For this fit, we also divide the data into bins of $\cos\theta^*$ (except for the TOF data). The results of the fit are shown in Fig. 6.15 and Table 6.2. The errors on the radiative widths are strongly correlated with the full widths.

To obtain a better estimate of the statistical error on the radiative widths, we fix the masses and full widths at their best values, and then refit. The result is that

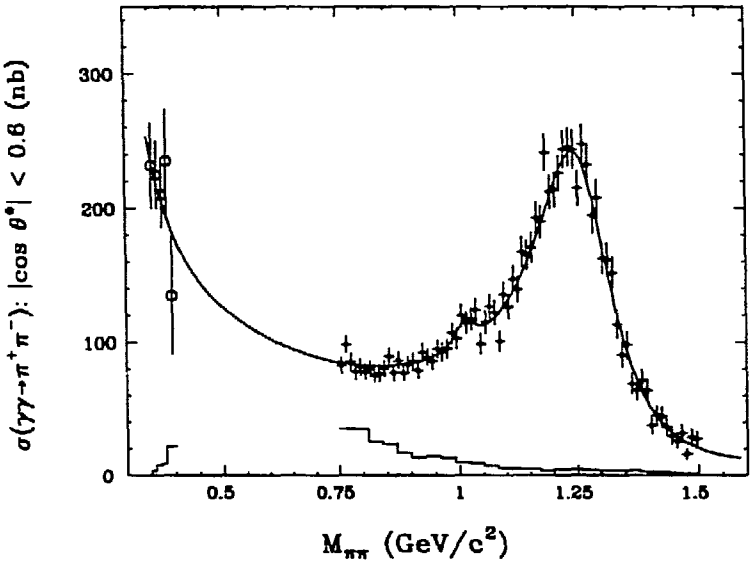

Figure 6.15 *Results of the fit with statistical errors only. Only data used in the fit are shown in the plot. The large circles are the TOF identified data. The other points are the sum of the 1-identified and 2-identified samples in the LA identified data. The histogram is the subtracted leptonic and hadronic background.*

the statistical errors on the widths are

$$\begin{aligned} \Gamma(f_2(1270) \to \gamma\gamma) &= 3.15 \pm .04 \text{ keV} \\ \Gamma(f_0(975) \to \gamma\gamma) &= 0.29 \pm .07 \text{ keV} \end{aligned} \tag{6.21}$$

Another check on the statistical significance of the $f_0(975)$ is made by refitting the data without the $f_0(975)$. The resulting χ^2 is worse by 20 for 3 fewer degrees of freedom, indicating that the statistical significance is approximately 4σ.

6.7.1 Angular Distributions

We have assumed that the $f_0(975)$ is a scalar, and that the $f_2(1270)$ is produced in a pure helicity-2 state. We can check this by looking at the angular distributions. In Fig. 6.16, we show the angular distributions for three different mass regions. In

Table 6.2 *Parameters of the fit in Fig. 6.15. The errors are statistical only.*

PARAMETER	VALUE	UNCERTAINTY
A'_0	0.86	0.18
A'_1	0.62	0.40
A'_2	-0.68	0.21
$\Gamma_{f_2(1270)}$	202 MeV/c^2	6 MeV/c^2
$\Gamma(f_2(1270) \rightarrow \gamma\gamma)$	3.15 keV	0.07 keV
$M_{f_0(975)}$	1012 MeV/c^2	7 MeV/c^2
$\Gamma_{f_0(975)}$	52 MeV/c^2	20 MeV/c^2
$\Gamma(f_0(975) \rightarrow \gamma\gamma)$	0.29 keV	.11 keV

the vicinity of the $f_0(975)$, the fit is very good. However, the $f_0(975)$ contributes only a small fraction of the cross section, so we are not very sensitive to its angular distribution. From statistical uncertainty alone, a scalar distribution for the $f_0(975)$ is favored over a $\sin^2\theta^*$ distribution by just under 1σ.

In the region of the $f_2(1270)$, we have fit to the angular distribution alone, fixing the contribution from the Born continuum at its fit value (B'_λ in Fig. 6.14). We define $\mathcal{F}^0_{f_2}$ and $\mathcal{F}^2_{f_2}$ as the helicity-0 and helicity-2 components of the amplitude for $\gamma\gamma \rightarrow f_2(1270)$:

$$\Gamma(f_2(1270) \rightarrow \gamma\gamma) \propto |\mathcal{F}^0_{f_2}|^2 + |\mathcal{F}^2_{f_2}|^2 \tag{6.22}$$

Fitting with statistical errors only, the best fit is for $\mathcal{F}^0_{f_2}$=0, with a 1σ upper limit on the ratio $\mathcal{F}^0_{f_2}$ to $\mathcal{F}^2_{f_2}$ of .12. Repeating the fit without unitarization, (thereby increasing the contribution of the relatively isotropic Born continuum) the upper limit increases to .18. Systematic uncertainties due to the shape of the continuum are comparable to the statistical uncertainties. Therefore, including systematic contributions of .09 from the unitarization question and .12 from the $\cos\theta^*$ dependence of the

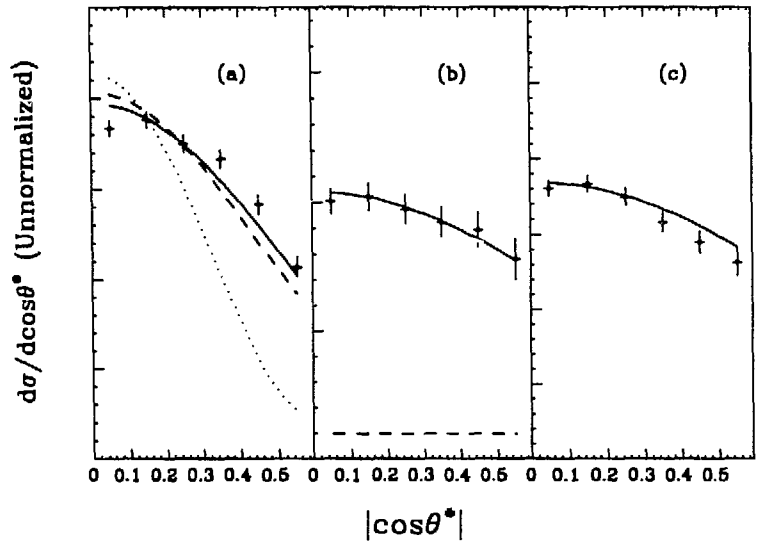

Figure 6.16 *Angular distributions in the region of (a) the $f_2(1270)$ ($1100 < M_{\pi\pi} < 1400$ MeV/c^2) and of (b) the $f_0(975)$ ($980 < M_{\pi\pi} < 1050$ MeV/c^2). The solid curves are the fit from Table 6.2. The dotted curve in (a) is the angular distribution for a helicity–0 $f_2(1270)$. The dashed curve in (a) shows the expected angular distribution if the ratio of the helicity–0 component of the $f_2(1270)$ amplitude to the helicity–2 component is 1/2. The dashed line in (b) shows the contribution of the $f_0(975)$. For completeness, we also show the angular distribution for $750 < M_{\pi\pi} < 900$ MeV/c^2 in (c).*

efficiency, we place a 1σ upper limit on the ratio:

$$\frac{\mathcal{F}^0_{f_2}}{\mathcal{F}^2_{f_2}} < 0.20 \tag{6.23}$$

To compare to other results which are expressed as 90% confidence limits on the ratio of the helicity components of the radiative width, we may rewrite our limit as:

$$\frac{\Gamma_0(f_2(1270) \to \gamma\gamma)}{\Gamma_2(f_2(1270) \to \gamma\gamma)} < 0.05 \quad \text{(90\% Confidence Level)} \tag{6.24}$$

where Γ_λ are the helicity–λ components of the radiative width. Most other experiments have shown angular distributions for the $f_2(1270)$ consistant with helicity–2.

Only one published upper limit exists. In Ref. 10, the Crystal Ball group sets an upper limit of .5 at the 1σ level. They had greater angular coverage than we have, but only limited statistics. In Ref. 5, which is not published, Johnson sets an upper limit from DELCO of 0.15 (90% Confidence). The angular acceptance of the DELCO detector is similar to that of the Mark II, but they have poorer statistics. Thus ours is the most stringent limit to date.

We estimate the uncertainty in $\Gamma(f_2(1270) \rightarrow \gamma\gamma)$ due to the helicity–2 assumption by fitting with $\mathcal{F}^0_{f_2}$ fixed at its upper limit. This increases $\Gamma(f_2(1270) \rightarrow \gamma\gamma)$ by 2%.

As expected for masses well below the $f_2(1270)$, the observed angular distribution is flatter than it is at the $f_2(1270)$ peak.

6.8 Systematic Errors

The relevant contributions to systematic uncertainties in the radiative widths of the $f_0(975)$ and the $f_2(1270)$ have been discussed as they arose. In Table 6.3 we list the systematic errors on $\Gamma(f_2(1270) \rightarrow \gamma\gamma)$ and $\Gamma(f_0(975) \rightarrow \gamma\gamma)$. The dominant contribution to the systematic uncertainty in the radiative width of the $f_0(975)$ is from the uncertainty in its full width (40% statistical). This could be reduced if we assume that the observed enhancement really is the $f_0(975)$, with mass shifted by some interference, and assume that its full width is that listed in the particle data compilation[46]: $\Gamma_{f_0(975)}$=34 $\pm$ 6 MeV. Because such a large mass shift is rather unlikely for such a narrow resonance, we do not feel that it is appropriate to assume that what we observe is the $f_0(975)$.

The largest contribution to the uncertainty in $\Gamma(f_2(1270) \rightarrow \gamma\gamma)$ is from the unitarization scheme. This amounts to an uncertainty in the shape of the underlying continuum. Several other systematic errors listed in Table 6.3 contribute at the 5% level. Adding all the systematic errors in quadrature, we obtain the following results for the radiative widths:

$$\begin{aligned} \Gamma(f_2(1270) \rightarrow \gamma\gamma) &= 3.15 \pm .04 \pm .39 \text{ keV} \\ \Gamma(f_0(975) \rightarrow \gamma\gamma) &= 0.29 \pm .07 \pm .12 \text{ keV} \end{aligned} \tag{6.25}$$

Table 6.3 *Systematic errors on $\Gamma(f_2(1270) \rightarrow \gamma\gamma)$ and $\Gamma(f_0(975) \rightarrow \gamma\gamma)$ considered in this analysis*

SYSTEMATIC ERROR SCOURCE	$\delta\Gamma(f_2(1270) \rightarrow \gamma\gamma)$	$\delta\Gamma(f_0(975) \rightarrow \gamma\gamma)$
$\delta\Gamma_R$ (Full width)	5%	40%
$\delta\mathcal{E}_{event}$ (Event Efficiency)	5%	5%
$\delta\mathcal{L}$ (Luminosity)	5%	5%
δLyth (Unitarization Scheme)	7%	<1%
$\delta P_{ID}(\pi)$ (Pion Identification)	4%	3%
$\delta P_{ID}(e,\mu)$ (Leptonic Subtraction)	2%	5%
Hadronic Backgrounds	<1%	2%
Helicity Hypothesis	2%	—
Mass dependence of $\Gamma_{f_2(1270)}$	2%	2%

Chapter 7. CONCLUSIONS

We have measured the cross section for $\gamma\gamma \rightarrow \pi^+\pi^-$ for invariant pion pair masses between 350 MeV/c^2 and 1.6 GeV/c^2, and for $\gamma\gamma \rightarrow \pi^+\pi^- + K^+K^-$ for $M_{\pi\pi}$ between 1.7 and 3.5 GeV/c^2. In the high mass region, we found approximate agreement with the absolute hard-scattering prediction of Brodsky and Lepage for $M_{\pi\pi} > 2.1$ GeV/c^2. For masses between 1.7 and 2.1 GeV/c^2, we observed an excess consistent with the hypothesis that either resonance production is still important, or that the hard-scattering calculation is not valid at these lower masses.

In the low mass region, we observed and measured the radiative widths of the $f_2(1270)$, and another possible resonance at a mass of ~1010 MeV/c^2. We also found that the underlying continuum is well-described by the Born approximation, modified for final state interactions, except at the high end, where we needed to modify the Born term downward in order to obtain good agreement with our data.

In Fig. 7.1, we show the combined $\pi^+\pi^-$ cross section from the two analyses. For the high mass data, we estimated the contribution of pion pairs using the *Ansatz* of Brodsky and Lepage (Eqn. 5.3) as to the relative cross sections† for $\gamma\gamma \rightarrow \pi^+\pi^-$ and $\gamma\gamma \rightarrow K^+K^-$.

The continuum has the expected $1/s$ behavior at low mass, and the expected $1/s^3$ behavior at high mass. Both the excess of the continuum in the high mass analysis and its deficiency in the low mass analysis appear consistent with the hypothesis that the continuum undergoes a gradual change in the mass region between 1 and 2.1 GeV/c^2.

---

† The TPC Collaboration measured the $\pi^+\pi^-$ and K^+K^- cross sections separately. Their results agree reasonable well with ours except in the region below 2.0 GeV/c^2, where their data is about 35% higher than our estimated $\pi^+\pi^-$ contribution. This could be explained by the fact that the excess relative to the hard-scattering prediction in this region is mostly $\pi^+\pi^-$.

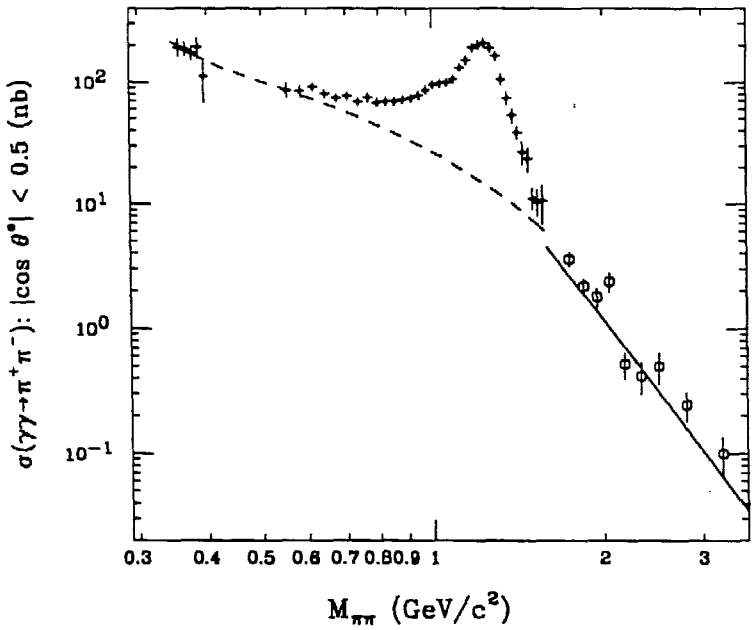

Figure 7.1 *Combined data from the low-mass and high-mass analyses. The large circles are the $\pi^+\pi^-$ cross section deduced from our measurement of the combined $\pi^+\pi^-$ and K^+K^- cross section under the hypothesis that the relative amounts of $\pi^+\pi^-$ and K^+K^- are accurately predicted in the model of Brodsky and Lepage. The solid line is the prediction of Brodsky and Lepage for pion pairs alone, and the dashed line is the modified continuum from the fit to the low-mass data (see Fig. 6.14). The angular region covered by the low mass data has been restricted so as to agree with that covered by the high mass data.*

We have observed a shoulder in the 1 GeV/c^2 region which we tentatively identify as the $f_0(975)$. This shoulder is well described as a scalar resonance with the following parameters:

$$\begin{aligned} M_{f_0} &= 1010 \pm 7 \pm 10 \text{ MeV}/c^2 \\ \Gamma_{f_0} &= 50 \pm 20 \pm 10 \text{MeV}/c^2 \\ \Gamma(f_0 \to \gamma\gamma) &= 0.29 \pm .07 \pm .12 \end{aligned} \tag{7.1}$$

The radiative width of the $f_0(975)$ has been measured only with low statistics. In the neutral channel ($\gamma\gamma \to \pi^0\pi^0$), The highest statistics measurement[12] was made by the Crystal Ball collaboration They also observe a shoulder in the 1 GeV/c^2 region at approximately the 2σ level. Their preliminary result was $\Gamma(f_0(975) \to \gamma\gamma) = 0.31 \pm 0.14 \pm 0.09$, in good agreement with our result. In the charged channel,

the highest statistics measurements[3,5] other than ours were made by the TPC and DELCO collaborations. Both show their data in 50 MeV bins. TPC appears to have a 1σ fluctuation in the bin covering 1000 to 1050 MeV/c^2, consistent with our data. DELCO, which has poorer mass resolution, shows no obvious effect. Our measured radiative width supports the hypothesis that the object we observe is not a normal $q\bar{q}$ meson.

The radiative width of the $f_2(1270)$ has been measured in many other experiments. The world average given in the Particle Properties Data Compilation[46] is $\Gamma(f_2(1270) \rightarrow \gamma\gamma)$=2.8 $\pm$ 0.2 KeV. However, since the result is somewhat model dependent, and several different models have been used, it is appropriate to identify which measurements have been made with which models and to compare our measurement with measurements made using similar models. For comparison with other experiments, we include two values of $\Gamma(f_2(1270) \rightarrow \gamma\gamma)$ from our data, one where we have not unitarized, and one where we have unitarized following the method of Lyth[19]. Our results are compared with those of other experiments in Table 7.1. Statistical and systematic errors have been combined quadratically.

The first analyses simply parameterized the $\pi^+\pi^-$ spectrum as a Breit-Wigner and a non-interfering continuum. This is quite reasonable in the neutral channel where the continuum is small, but it was quickly seen to be inadequate in the charged channel, where the observed peak of the $f_2(1270)$ is shifted by interference with the continuum. The average of these measurements is 3.09 $\pm$ 0.25.

The next generation of analyses used the Born approximation to calculate the continuum which was than allowed to interfere with the $f_2(1270)$. (We refer to this model as Born int.) We found that the Born approximation overestimates the continuum by a factor of 2 to 4 in the region of the $f_2(1270)$. Others observed the same problem, but chose to solve it by the physically unrealistic method of allowing only partial interference. We find that one can fit the data well with such a model, but it fails to satisfy the constraint of unitarity. The average of these measurements, using only the most recent values from each experiment, is 2.94 $\pm$ 0.19. Our result using

Table 7.1 *Measurements of* $\Gamma(f_2(1270) \rightarrow \gamma\gamma)$. [a]*Measurements in the* $\pi^0\pi^0$ *channel are not as model dependent, because the non-resonant interfering continuum is much smaller.* [b]*The interference between the Born term and the* $f_2(1270)$ *was multiplied by an arbitrary parameter, usually around .5.* [c]*The QCD prediction of Brodsky and Lepage was used for* $M_{\pi\pi} > 1$ GeV/c^2. [d]*The Born term was modified to reflect the onset of a* $1/s^3$ *behavior behavior expected from QCD in the vicinity of the* $f_2(1270)$. [e]*The unpublished analysis is more recent than the published analysis, and is therefore assumed to supercede it.*

Experiment	Ref.	Model	Decay	$\Gamma(f_2 \rightarrow \gamma\gamma)$ (keV)
TASSO	7	no int.	$\pi^+\pi^-$	$3.2 \pm .2 \pm .6$
Crystal Ball (SPEAR)	10	no int.[a]	$\pi^0\pi^0$	$2.7 \pm .2 \pm .6$
Crystal Ball (DORIS)	12 (prel.)	no int.[a]	$\pi^0\pi^0$	$3.26 \pm .16 \pm .28$
JADE	6 (prel.)	no int.[a]	$\pi^0\pi^0$	$3.09 \pm .10 \pm .39$
Mark II (SPEAR)	11	Born int.[b]	$\pi^+\pi^-$	$3.6 \pm .3 \pm .5$
Mark II (PEP)	2	Born int.[c]	$\pi^+\pi^-$	$2.52 \pm .13 \pm .38$
Mark II (PEP)	this work	Born int.[d]	$\pi^+\pi^-$	$2.80 \pm .04 \pm .28$
DELCO	4	Born int.[e]	$\pi^+\pi^-$	$2.70 \pm .05 \pm .2$
DELCO	5 (unpub.)	Born int.[e]	$\pi^+\pi^-$	$2.77 \pm .07 \pm .3$
PLUTO	13	Born int.	$\pi^+\pi^-$	$3.25 \pm .25 \pm .5$
TPC/2γ	3	Born int.[b]	$\pi^+\pi^-$	$3.2 \pm .1 \pm .4$
PLUTO	13	Mennessier	$\pi^+\pi^-$	$2.85 \pm .25 \pm .5$
CELLO	8	Mennessier[e]	$\pi^+\pi^-$	$2.5 \pm .1 \pm .5$
CELLO	9 (prel.)	Mennessier[e]	$\pi^+\pi^-$	$3.0 \pm .1 \pm .5$
DELCO	5 (unpub.)	Mennessier	$\pi^+\pi^-$	$2.93 \pm .07 \pm .29$
DELCO	5 (unpub.)	Lyth	$\pi^+\pi^-$	$3.34 \pm .07 \pm .34$
Mark II (PEP)	this work	Lyth[d]	$\pi^+\pi^-$	$3.15 \pm .04 \pm .31$

this method is $\Gamma(f_2(1270) \rightarrow \gamma\gamma) = 2.80 \pm 0.28$, where the systematic uncertainty due to model dependence is neglected. Including this result, the new average is 2.90 ± 0.16.

The first fully unitary model was that of Mennessier. He imposed unitarity by modifying the Born term. A consequence of this is that the radiative width has a slightly different meaning than in the model of Lyth. In Ref. 5, Johnson claims that the relation between the radiative widths in the two models is

$$\Gamma_{\rm Lyth}(f_2(1270) \rightarrow \gamma\gamma) = \Gamma_{\rm Mennessier}(f_2(1270) \rightarrow \gamma\gamma) + .257 \text{ KeV} \qquad (7.2)$$

Several experiments have presented measurements using Mennessier's model. The average is 2.92 ± 0.19, which is extremely close to the average of the Born int. models. This must be thought of as somewhat of a coincidence.

Only one other measurement was made using the model of Lyth. The result given in Ref. 5 is 3.34 ± 0.35, compared to our result of 3.15 ± 0.31 (systematic error due to model dependence not included). Using Eqn. 7.2 to compare to measurements in the model of Mennessier, we find excellent agreement.

We have taken an experimentally motivated approach to fitting the low mass data. In Fig. 7.2, we compare our data to the prediction of Morgan and Pennington, and to two sample curves from Mennessier. The Mennesier curves are predictions for $\cos\theta^*=0$, normalized to our angular acceptance by assuming an isoscalar angular distribution. Since the true angular distribution is peaked at large $\cos\theta^*$ near threshold, but at $\cos\theta^*=0$ at the $f_2(1270)$, we have slightly underestimated the Mennessier prediction at low masses, and overestimated it near the $f_2(1270)$ by $\sim$ 30%. The normalization of the Mennessier curves looks high for the radiative widths he claims to have used (2 - 3 keV) for the $f_2(1270)$, but others who have used the Mennessier model to fit their data have measured values for $\Gamma(f_2(1270) \rightarrow \gamma\gamma)$ consistant with ours. Thus, there is some uncertainty as to the meaning of the normalization in Mennessier's paper.

The model of Morgan and Pennington does fairly well, but has no provision for an $f_0(975)$ of the size we observe. They do predict structure in the $J = 0$ partial wave due to final state interactions, but the predicted magnitude of such structure is down by a factor of 100 relative to the $J = 2$ partial wave. Most of the rest of the

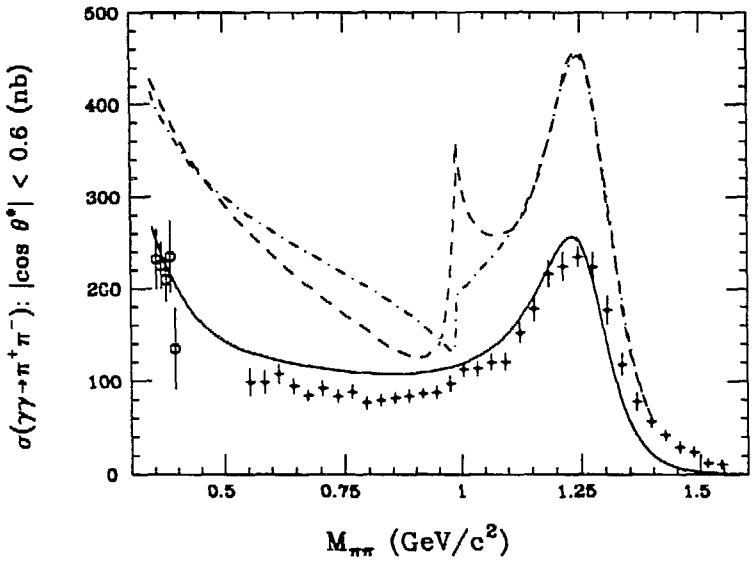

Figure 7.2 *Low mass data compared to sample predictions of Morgan and Pennington (solid curve), and of Mennessier (dashed and dot-dashed curves).*

discrepancy can be explained by varying the detailed shape of the $f_2(1270)$ resonance in their model.

The model of Mennessier does predict visible structure (under certain conditions). He allows for two s–wave resonances – the $f_0(975)$, and a broad scalar σ or ϵ resonance at lower mass. He also predicts structure using only a broad s–wave, because of the requirement of unitarity (final state interactions). While Mennessier does predict structure qualitatively similar to what we observe near 1 GeV/c^2, the broad scalar resonance necessary to achieve this structure predicts an unacceptably large cross section at lower masses. This appears to be true even given the uncertainty in the normalization in the Mennessier curves, because he explicitly predicts an enhancement near threshold by a factor of $\sim$2 relative to the Born term. A broad scalar resonance with a radiative width large enough to predict such an enhancement, would also be observable in the $\pi^0\pi^0$ channel. Preliminary data[12] for $\gamma\gamma \to \pi^0\pi^0$ show no such enhancement.

Both models incorporate known final state interaction effects, and give qualitatively reasonable results, but an overall fit to the charged and neutral pion pair cross sections is needed to better determine the detailed parameters. It appears, however, that it will be challenging for either model to simultaneously explain our observation of structure near 1 GeV/c^2 and the lack of a large continuum in the neutral channel.

Appendix A. Tables of Results for Pion Pair Cross Section

High Mass Results

For the high mass analysis, only statistical errors are shown.

$M_{\pi\pi}$ (GeV/c^2)	$\sigma(\gamma\gamma\to\pi^+\pi^-,K^+K^-)$ (nanobarns)	
	$0.0 < \lvert\cos\theta^*\rvert < 0.3$	$0.3 < \lvert\cos\theta^*\rvert < 0.5$
1.7 - 1.8	4.9 ± .7	1.6 ±.5
1.8 - 1.9	3.4 ± .6	0.73 ±.30
1.9 - 2.0	3.0 ± .5	0.53 ±.30
2.0 - 2.1	2.4 ± .5	2.4 ±.8
2.1 - 2.25	0.84 ± .23	0.25 ±.13
2.25 - 2.4	0.67 ± .21	0.22 ±.13
2.4 - 2.6	0.35 ± .13	0.77 ±.31
2.6 - 3.0	0.30 ± .09	0.27 ±.13
3.0 - 3.5	0.14 ± .06	0.10 ±.07

Low Mass Results

For the low mass analysis, $\sigma(\gamma\gamma\to\pi^+\pi^-)$ is shown in nanobarns, integrated over center-of-mass scattering angles – $|\cos\theta^*| < 0.6$. Statistical and systematic errors are given separately. The overall normalization error of ~7% (5% from luminosity and 5% from efficiency) is not included in the systematic errors.

$M_{\pi\pi}$ (GeV/c^2)	$\sigma(\gamma\gamma \to \pi^+\pi^-)$ (nanobarns)	$M_{\pi\pi}$ (GeV/c^2)	$\sigma(\gamma\gamma \to \pi^+\pi^-)$ (nanobarns)
0.355	232.0 ± 9.3 ± 31.1	1.125	139.3 ± 9.8 ± 4.7
0.365	225.0 ± 8.2 ± 23.2	1.135	167.6 ± 11.3 ± 5.7
0.375	210.0 ± 9.4 ± 21.8	1.145	165.1 ± 11.1 ± 5.7
0.385	235.0 ± 19.0 ± 33.6	1.155	170.8 ± 11.5 ± 5.9
0.395	135.0 ± 25.4 ± 35.8	1.165	192.9 ± 12.0 ± 6.8
0.555	99.2 ± 4.2 ± 12.9	1.175	189.7 ± 11.9 ± 6.7
0.585	97.7 ± 3.6 ± 11.8	1.185	241.4 ± 13.7 ± 8.6
0.615	107.5 ± 3.7 ± 10.2	1.195	212.0 ± 12.8 ± 7.7
0.645	94.5 ± 3.4 ± 9.9	1.205	213.9 ± 13.1 ± 7.8
0.675	84.5 ± 3.3 ± 9.3	1.215	226.2 ± 13.4 ± 8.4
0.705	92.2 ± 3.6 ± 9.1	1.225	244.0 ± 13.8 ± 9.1
0.735	83.7 ± 3.5 ± 9.0	1.235	245.4 ± 14.2 ± 9.2
0.755	82.6 ± 6.1 ± 8.0	1.245	243.3 ± 14.5 ± 9.2
0.765	98.1 ± 6.5 ± 8.1	1.255	214.0 ± 13.3 ± 8.3
0.775	85.3 ± 6.2 ± 8.1	1.265	247.3 ± 15.2 ± 9.4
0.785	77.5 ± 6.0 ± 7.8	1.275	232.1 ± 14.5 ± 9.0
0.795	81.4 ± 6.2 ± 7.3	1.285	194.5 ± 13.6 ± 7.6
0.805	77.7 ± 6.1 ± 8.0	1.295	207.5 ± 13.7 ± 8.2
0.815	80.0 ± 6.1 ± 5.7	1.305	162.5 ± 12.1 ± 6.4
0.825	75.6 ± 5.8 ± 5.3	1.315	161.5 ± 12.4 ± 6.4
0.835	76.4 ± 6.0 ± 4.8	1.325	151.6 ± 12.2 ± 6.1
0.845	80.5 ± 6.1 ± 4.5	1.335	113.1 ± 10.8 ± 4.5
0.855	89.4 ± 6.3 ± 3.9	1.345	90.4 ± 9.6 ± 3.7
0.865	77.2 ± 6.3 ± 4.4	1.355	97.8 ± 9.9 ± 4.0
0.875	86.0 ± 6.4 ± 3.5	1.365	68.7 ± 8.1 ± 2.9
0.885	76.6 ± 5.9 ± 2.9	1.375	64.2 ± 7.9 ± 2.7
0.895	83.8 ± 6.2 ± 3.0	1.385	71.2 ± 8.5 ± 3.0
0.905	85.3 ± 6.3 ± 2.8	1.395	63.6 ± 8.2 ± 2.7
0.915	78.8 ± 6.2 ± 7	1.405	37.6 ± 6.5 ± 1.7
0.925	92.3 ± 6.8 ± 2.7	1.415	45.2 ± 6.9 ± 2.0
0.935	88.7 ± 6.5 ± 2.8	1.425	44.6 ± 6.7 ± 2.0
0.945	85.7 ± 6.6 ± 2.9	1.435	36.1 ± 6.6 ± 1.6
0.955	94.7 ± 7.1 ± 2.8	1.445	29.6 ± 6.1 ± 1.3
0.965	93.0 ± 7.0 ± 2.9	1.455	26.1 ± 5.5 ± 1.2
0.975	95.4 ± 7.2 ± 3.0	1.465	31.9 ± 6.4 ± 1.4
0.985	106.9 ± 7.5 ± 3.2	1.475	16.1 ± 4.2 ± 0.8
0.995	102.6 ± 7.7 ± 3.4	1.485	28.6 ± 6.2 ± 1.3
1.005	119.8 ± 8.3 ± 3.6	1.495	27.3 ± 5.6 ± 1.3
1.015	114.4 ± 8.2 ± 3.6	1.505	9.2 ± 3.3 ± 0.5
1.025	116.8 ± 8.2 ± 3.7	1.515	14.3 ± 4.3 ± 0.7
1.035	123.9 ± 8.7 ± 3.9	1.525	12.5 ± 4.6 ± 0.6
1.045	98.7 ± 7.8 ± 3.3	1.535	14.3 ± 4.3 ± 0.7
1.055	114.9 ± 8.6 ± 3.7	1.545	4.9 ± 2.6 ± 0.3
1.065	126.6 ± 9.1 ± 4.1	1.555	10.7 ± 3.7 ± 0.6
1.075	122.0 ± 9.0 ± 4.0	1.565	13.4 ± 4.2 ± 0.7
1.085	100.6 ± 8.1 ± 3.3	1.575	8.1 ± 3.8 ± 0.4
1.095	135.7 ± 9.5 ± 4.5	1.585	12.1 ± 4.0 ± 0.6
1.105	126.3 ± 9.3 ± 4.3	1.595	7.9 ± 3.3 ± 0.5
1.115	146.9 ± 10.0 ± 4.9		

REFERENCES

1. Ch. Berger *et al.*, PLUTO Collaboration, Phys. Lett. **137B**, 267 (1984)
2. Results on the first 35 pb^{-1} of this experiment have been published in J.R. Smith *et al.*, Phys. Rev. **D30**, 851 (1984)
3. H. Aihara *et al.*, TPC/2γ Collaboration, Phys. Rev. Lett. **57**, 404 (1986).
4. A. Courau *et al.*, DELCO Collaboration, Phys. Lett. **147B**, 227 (1984)
5. R. Johnson, DELCO Collaboration, Ph.D. thesis, SLAC294, unpublished.
6. J. E. Olson, JADE Collaboration, contributed paper to the 24th International Conference on High Energy Physics, Munich 1988.
7. R. Brandelik *et al.*, TASSO Collaboration, Z. Phys. **C10**, 117 (1981).
8. H.J. Behrend *et al.*, CELLO Collaboration, Z. Phys. **C23**, 223 (1984).
9. H.J. Behrend *et al.*, CELLO Collaboration, contributed paper to the 24th International Conference on High Energy Physics, Munich 1988.
10. C. Edwards *et al.*, Crystal Ball Collaboration, Phys. Lett. **110B**, 82 (1982).
11. A. Roussarie *et al.*, MARK II Collaboration, SPEAR, Phys. Lett. **B105**, 304 (1981).
12. H. Marsiski *et al.*, Crystal Ball Collaboration, Proc. XXIII Int. Conf. on High Energy Physics, Berkeley, 1986 (Ed. S.C. Loken; pub. World Scientific, 1987) p. 1223. Also H. Marsiski Ph. D. thesis (Hamburg U.) DESY-F31-88-02 (1988)
13. Ch. Berger *et al.*, PLUTO Collaboration, Z. Phys. **C26**, 199 (1984)
14. A. Courau *et al.*, DM1 Collaboration, Nucl. Phys. **B271**, 1 (1986)
15. Z. Ajaltouni *et al.*, DM2 Collaboration, Phys. Lett. **B194**, 573 (1987)
16. S.J. Brodsky and G.P. Lepage, Phys. Rev. **D24**, 1808 (1981)
17. D. Morgan and M.R. Pennington, Phys. Lett. **192B**, 207 (1987)
18. G. Mennessier, Z. Phys. **C16**, 241 (1983)
19. D.H. Lyth, J. Phys. G **10**, 39 (1984)
20. C.F. v. Weizsäcker, Z. Phys. **88**, 612 (1934)
21. E.J.Williams, Phys. Rev. **45**, 729 (1934)

21. E.J.Williams, Phys. Rev. **45**, 729 (1934)
22. F.E. Low, Phys. Rev. **120**, 582 (1960)
23. S.J. Brodsky, T. Kinoshita, and H. Terazawa, Pys. Rev. Lett. **25**, 972 (1970), and Phys. Rev. **D4**, 1532 (1971)
24. G. Bonneau, M. Gourdin and F. Martin, Nucl. Phys. **B54**, 573 (1973)
25. J.H. Field, Nucl. Phys **B168**, 477 (1980); addendum in Nucl. Phys. **B176**, 545 (1980)
26. R.H.Schindler *et al.*, Phys. Rev. D**24**, 78 (1981).
27. Mark Nelson, Ph.D. Thesis
28. Particle Properties Data Booklet, pp. 155-156, (1986)
29. John Dillon, Trilling-Goldhaber Technical Note # 232 (1982)
30. H. Aihara *et al.*, TPC/2γ Collaboration, Phys. Rev. Lett. **54**, 2564 (1985), and Phys. Rev. **D37**, 28 (1988)
31. Particle Properties Data Booklet, p. 72, (1986)
32. D. Karlen, Mark II memo, 13 October 1987
33. Peter C. Rowson, SLAC MEMO, TG note 379, 21 Feb. 1984
34. GGDEPA is based on Ref. 23
35. F.M.Renard, *Electron Positron Collisions*, (pub. Editions Frontières, Gif sur Yvette, France, 1981), 206
36. F.A. Berends, P.H. Daverveldt and R. Kleiss, Monte Carlo simulation of two-photon processes, Leiden preprint. See also Phys. Lett. **148B**, 489 (1984)
37. F. Butler, Ph. D. thesis, 100-103 (1988)
38. J. Boyer *et al.*, Phys. Rev. Lett. **56**, 207 (1986)
39. J.R. Smith, Ph. D. thesis, University of California at Davis, 1983 (unpublished).
40. M. Althoff *et al.*, Phys. Lett. **13B**, 449 (1983). The measured limit is $\sigma(\gamma\gamma\rightarrow\overline{p}p)$ <0.5 nb for $\sqrt{s}$ above 3 GeV.
41. H.D.I. Arbanel and M.I. Goldberger, Phys. Rev. **165**, 1594 (1968)
42. V.M. Budnev *et al.*, Physics Reports **15C**, 241 (1975)

43. K.M. Watson, Phys. Rev. **88**, 1163 (1952)

44. J.M. Blatt and V.F. Weiskopf, *Theoretical Nuclear Physics*, pub. Wiley, New York, pp. 359–365 and 386–389 (1952)

45. G. Grayer *et al.*, Nucl. Phys. **B75**, 189 (1974).

46. Particle Properties Data Booklet (1988)

47. G. Gidal *et al.*, MARK II Collaboration, SPEAR, Phys. Lett. **107B**, 153 (1981)

48. M.S. Chanowitz, *Proceedings of the VIIIth International Workshop on Photon-Photon Collisions, Shoresh, Israel*, ed. Uri Karshon; pub. World Scientific, Singapore (1988)